THERMAL TEMPERING OF LAYERED CERAMIC STRUCTURES

BY

BAHRAM HOJJATIE

A DISSERTATION PRESENTED TO THE GRADUATE SCHOOL
OF THE UNIVERSITY OF FLORIDA IN PARTIAL FULFILLMENT
OF THE REQUIREMENTS FOR THE DEGREE OF
DOCTOR OF PHILOSOPHY

UNIVERSITY OF FLORIDA

1990

Dedication

To my family
and
my friends

ACKNOWLEDGMENTS

I would like to thank Dr. Ulrich H. Kurzweg, the chairman, and Dr. Kenneth J. Anusavice, the cochairman of my doctoral committee, for providing continuous support, direction, and encouragement. During my graduate study, Dr. Kurzweg was readily accessible for guidance and direction. He encouraged the development of critical thinking skills and installed confidence and maintained support throughout this dissertation.

Dr. Anusavice, who is my supervisor in the Department of Dental Biomaterials, has established an atmosphere of trust and respect at that department, and his care and understanding has made it possible for me to pursue graduate study during my full-time employment at the University of Florida. He not only introduced this research to me, but also provided me with financial and unlimited technical support. This dissertation would have been impossible without the support and understanding of Dr. Kurzweg and Dr. Anusavice. The support and encouragement of Dr. Paul H. DeHoff from the University of North Carolina at Charlotte are greatly appreciated. Dr. DeHoff provided the thermal stress analysis programs which he developed based on viscoelastic theory. Also, as a consultant to the Dental Biomaterials Department, he has enhanced my understanding of the mechanics of solids.

The author acknowledges the technical advice of Dr. Calvin C. Oliver regarding the experimental and theoretical thermal analysis. Special gratitude also goes to Dr. Martin A. Eisenberg, for assisting me in establishing a foundation in finite element analysis and to Dr. Charles E. Taylor for his continuous support and encouragement in the area of experimental mechanics. I would like to express my appreciation to other faculty members and graduate students at the University of Florida, specifically Dr. Chung K. Hsieh and Mr. Francisco Soeiro who provided support for academic studies. Appreciation is also extended to the personnel at the Department of Dental

Biomaterials, specifically to Mr. Robert B. Lee for his expert assistance in the experimental analysis and to Mrs. Anna Grey for preparing some of the ceramic specimens.

Finally, I wish to express my sincere appreciation to my family, for their love and sacrifice, and to my friends for their moral support and encouragement, without which this research would have never been started. This study was made possible by the financial support of the National Institutes of Health, National Institute of Dental Research, through Grant No. DE06672.

TABLE OF CONTENTS

	Page
ACKNOWLEDGEMENTS	iii
LIST OF TABLES	viii
LIST OF FIGURES	ix
NOMENCLATURE	xxii
ABSTRACT	xxv
CHAPTER I INTRODUCTION	1
Strengthening of Glass	1
Influence of Flaws on Strength	1
Chemical Tempering	3
Physical Tempering	4
Comparison Between Chemical and Physical Tempering	6
Major Findings from Thermal Tempering of Glass	7
Strengthening of Ceramics	12
Major Findings from Thermal Tempering of Ceramics	13
Strengthening of Dental Ceramics	16
Background	16
Influence of Crown Design on Stress Distribution	19
Tempering of Dental Ceramics	25
Stress Analysis by Viscoelasticity and Structural Relaxation	26
Stress Analysis by Finite Element Method	27
Objectives of the Present Study	28
CHAPTER II EXPERIMENTAL METHOD AND ANALYSES	29
Determination of Thermal Data	29
Measurements of Thermal Contraction Coefficients	29
Preparation of Bilayered Disk Specimens	31
Temperature Distribution within the Dental Furnace	33

Page

Measurement of Cooling Profiles 34
Tempering by Gaseous Cooling Media 36
Tempering by Liquids 39
Influence of Initial Tempering Temperature 40
Measurement of Heat Transfer Coefficients 40
Analysis of Induced Cracks by Microhardness Indentation Test 42
Biaxial Flexure Test 46
Background 46
Flexural Testing of Porcelain Disks 47

CHAPTER III ANALYTICAL AND NUMERICAL METHODS 50
Calculation of Heat Transfer Coefficients 50
Free Convective Cooling 50
Characteristic Length 52
Tempering by Vertical Flow 53
Tempering by Horizontal Flow 54
Radiative Heat Transfer Coefficient 54
Closed-Form Solutions 55
Two-Dimensional Model (2-D) 55
Simplified One-Dimensional Model (1-D) 62
Finite Element Models 65
A. Axisymmetric Model of Ceramic Disks for Thermal Stress Analysis 65
B. Three-Dimensional Model of Dental Ceramic Crowns for Static Analysis 70
C. Axisymmetric Model of Dental Ceramic Crowns for Thermal Stress Analysis 73

CHAPTER IV RESULTS 77
Thermal Analyses 77
Thermal Contraction Curves 77
Temperature Distribution within the Dental Furnace 77
Experimental Cooling Profiles 78
Heat Transfer in Gaseous and Liquid Cooling Media 86
Determination of the Average Heat Transfer Coefficients 94

Page

Stress Analyses using Viscoelasticity and Structural Relaxation 103
A. Gaseous Cooling Media 103
B. Liquid Cooling Media 127
Stress Analyses using Finite Element Method 135
A. Transient Stress Analysis of Bilayered Ceramic Disks 135
B. Static Analysis of Dental Ceramic Crowns 183
C. Transient Stress Analysis of Dental Ceramic Crowns 192
Analyses of Crack Size Induced by a Microhardness Indenter 227
A. Statistical Analysis 227
B. Calculation of Surface Compressive Stresses 232
Evaluation of the Biaxial Flexure Test Data 232

CHAPTER V DISCUSSIONS AND CONCLUSIONS 237
Cooling Profiles 237
Viscoelastic Analysis 240
Finite Element Analyses 242
A. Transient Stress Analysis of Bilayered Ceramic Disks 242
B. Static Analysis of Dental Ceramic Crowns 243
C. Transient Stress Analysis of Dental Ceramic Crowns 243
Quenching in Silicone Oil 244
Microhardness Indentation Analysis..... 245
Biaxial Flexure Strength..... 247
Comparison of Predicted and Experimentally Determined Stresses 249
Recommendations for Future Studies 250

APPENDIX A VISCOELASTICITY AND STRUCTURAL RELAXATION 252

APPENDIX B FINITE ELEMENT METHOD 256

LIST OF REFERENCES 261

BIOGRAPHICAL SKETCH 268

LIST OF TABLES

Table	Description	Page
1.1	Flexural strength of 96% alumina quenched into various media.	14
1.2	Physical properties of glass and dental ceramics.	18
3.1	Thermal and mechanical properties of materials used in the finite element analysis.	70
4.1	Mean crack size (μm) for bilayered disks tempered in silicone oil from an initial temperature of 850°C.	228
4.2	Mean crack size (μm) for bilayered disks tempered in silicone oil from an initial temperature of 750°C.	228
4.3	Mean crack size (μm) for bilayered disks tempered in silicone oil at kinematic viscosity of 50 centistokes.	229
4.4	Mean crack size (μm) and 95% confidence intervals for bilayered disks tempered in silicone oil and in air.	229
4.5	Mean crack size (μm) for bilayered disks cooled in air from an initial temperature of 982°C.	231
4.6	Surface stresses in body porcelain disks cooled by free convection (FC) and tempering (T) in air, and quenched in silicone oil (OQ).	231
4.7	Mean flexural strength (MPa) of body porcelain disks cooled in air and quenched in silicone oil from various initial temperatures.	233
4.8	Mean flexural strength (MPa) and 95% confidence intervals of body porcelain disks cooled in air by various cooling methods.	233
4.9	Comparison of the tempering stresses in body porcelain disks calculated from viscoelastic model and biaxial flexure test.	235

LIST OF FIGURES

Figure	Description	Page
1.1	Residual stress distribution in glass resulting from physical (thermal) and chemical tempering.	8
1.2	Transient stress distribution in glass plate during tempering from initial temperatures of 616, 648 and 738°C.	9
1.3	Degree of temper (nm/cm) in a glass plate as a function of initial temperature and heat transfer coefficient.	11
1.4	Stress distribution at rupture for alumina bars quenched in silicone oil from an initial temperature of 1600°C.	15
1.5	Flexural strength of tempered alumina as a function of initial tempering temperature.	17
1.6	Two-dimensional finite element model of a prepared central incisor restored with each of three ceramic crown designs.	20
1.7	Maximum tensile stress (MPa) for crowns with ceramic thickness of 1.0 mm and 4.0 mm produced by an external load.	21
1.8	Maximum compressive stress (MPa) for crowns with ceramic thickness of 1.0 mm and 4.0 mm.	22
1.9	Peak values of principal stresses (σ_{max}) in ceramic and cement as a function of load orientation.	24
2.1	Schematic diagram of a single push-rod dilatometer.	30
2.2	Thermal contraction versus temperature profiles of opaque and body porcelains using a reference temperature of 25°C.	32
2.3	Steady-state temperature distribution in the test furnace at a control temperature of 982°C.	35
2.4	Schematic illustration of vertical air flow conditions for the small disk specimen.	37
2.5	Schematic illustration of horizontal air flow conditions and modes of heat loss.	38

Figure	Description	Page
2.6	Locations and directions of specimen and indentations applied at the surface of the body porcelain.	45
2.7	Biaxial flexure test apparatus.	48
3.1	Simplification of the heat transfer analysis from a two-dimensional model to a one-dimensional analytical model.	57
3.2	Bessel function of the first kind of order zero and order one.	60
3.3	Axisymmetric thermal model and boundary conditions for the finite element analyses.	66
3.4	Node and material property numbers used in the finite element model of a bilayered ceramic disk.	68
3.5	Element numbers and boundary conditions used in the finite element model of a bilayered ceramic disk.	69
3.6	Mesial view of a mandibular second molar showing three design cases.	71
3.7	Three-dimensional finite element model of the molar crown.	72
3.8	Locations of the applied loads in the finite element model.	74
3.9	Cross section of a ceramic molar crown used for finite element thermal stress analysis.	75
3.10	Axisymmetric finite element model of the bilayered ceramic molar crown consisted of opaque and body porcelain layers.	76
4.1	Temperature versus distance from the door of the test furnace at a control temperature of 982°C.	79
4.2	Temperature versus time profiles of a 2-mm-thick disk for free convective cooling, tempering by horizontal and vertical flows.	80
4.3	Temperature versus time profiles of a 6-mm-thick disk for three air cooling conditions.	82
4.4	Temperature versus time profiles in a 2-mm-thick disk using. slow cooling, free convective cooling and tempering in air.	83
4.5	Temperature versus time profile of a 2-mm and a 6-mm-thick disk cooled by free convection in air and helium.	84

Figure	Description	Page
4.6	Cooling profiles of a 2-mm-thick disk subjected to free convection and tempering in helium and air.	85
4.7	Cooling profiles of 2-mm (t = 2) and 6-mm (t = 6) thick disks tempered by vertical and horizontal flow of nitrogen.	87
4.8	Approximate values of the convective heat transfer coefficient in air and water.	88
4.9	Equivalent heat transfer coefficients versus surface temperature for a 2-mm thick disk subjected to various modes of cooling.	89
4.10	Radiation and convection heat losses from a 2-mm-thick disk.	90
4.11	Cooling profile of a thin copper disk for various values of heat transfer coefficient.	92
4.12	Cooling profiles of a thin copper disk cooled in various cooling media from an initial temperature of 982°C.	93
4.13	Calculated and measured cooling profiles for free convective cooling of a 2-mm-thick porcelain disk in air using a heat transfer coefficient of 57 $W/m^2 \cdot K$.	95
4.14	Experimental and the calculated cooling profiles for a thin copper disk subjected to free convection using heat transfer coefficients of 60 and 80 $W/m^2 \cdot K$.	97
4.15	Experimental and calculated (1-D) cooling profile for a 2-mm-thick porcelain disk subjected to free convection using a heat transfer coefficient of 70 $W/m^2 \cdot K$.	98
4.16	Graphical solution of the transcendental relation (equation 39) for a heat transfer coefficient of 70 $W/m^2 \cdot K$.	99
4.17	Calculated and measured cooling profiles for the free convective cooling of a 2-mm-thick disk in air using a heat transfer coefficient of 70 $W/m^2 \cdot K$ in the thermal models.	100
4.18	Cooling profiles calculated from the 1-D and 2-D models for a 2-mm-thick disk tempered in air using a heat transfer coefficient of 560 $W/m^2 \cdot K$.	102

Figure	Description	Page
4.19	Actual and fictive temperature versus time profiles at the surface and the insulated face of a 2-mm-thick body porcelain disk cooled by free convection from an initial temperature of 982°C.	105
4.20	Transient stresses versus time at the surface and the insulated face of a 2-mm-thick body porcelain disk cooled by free convection from an initial temperature of 982°C.	106
4.21	Residual stress distribution in a 2-mm-thick body porcelain disk subjected to free convective cooling from an initial temperature of 982°C.	107
4.22	Actual and fictive temperature versus time profiles at the surface and the insulated face of a 6-mm-thick body porcelain disk cooled by free convection from an initial temperature of 982°C.	109
4.23	Transient stresses versus time at the surface and the insulated face of a 6-mm-thick body porcelain disk cooled by free convection from an initial temperature of 982°C.	110
4.24	Residual stress distribution in a 6-mm-thick body porcelain disk subjected to free convective cooling from an initial temperature of 982°C.	111
4.25	Actual and fictive temperature versus time profiles at the surface and the insulated face of a 2-mm-thick body porcelain disk tempered from an initial temperature of 982°C.	113
4.26	Transient stresses versus time at the surface and the insulated face of a 2-mm-thick body porcelain disk tempered from an initial temperature of 982°C.	114
4.27	Residual stress distribution in a 2-mm-thick body porcelain disk tempered from an initial temperature of 982°C.	115
4.28	Actual and fictive temperature versus time profiles at the surface and the insulated face of a 2-mm-thick body porcelain disk tempered from an initial temperature of 850°C.	116
4.29	Transient stresses versus time at the surface and the insulated face of a 2-mm-thick body porcelain disk tempered from an initial temperature of 850°C.	117
4.30	Residual stress distribution in a 2-mm-thick body porcelain disk tempered from an initial temperature of 850°C.	118

Figure	Description	Page
4.31	Actual and fictive temperature versus time profiles at the surface and the insulated face of a 2-mm-thick body porcelain disk tempered from an initial temperature of 750°C.	119
4.32	Transient stresses versus time at the surface and the insulated face of a 2-mm-thick body porcelain disk tempered from an initial temperature of 750°C.	120
4.33	Residual stress distribution in a 2-mm-thick body porcelain disk tempered from an initial temperature of 750°C.	121
4.34	Actual and fictive temperature versus time profiles at the surface and the insulated face of a 2-mm-thick body porcelain disk tempered from an initial temperature of 650°C.	122
4.35	Transient stresses versus time at the surface and the insulated face of a 2-mm-thick body porcelain disk tempered from an initial temperature of 650°C.	123
4.36	Residual stress distribution in a 2-mm-thick body porcelain disk tempered from an initial temperature of 650°C.	124
4.37	Residual compressive and tensile stresses at the surface of a 2-mm-thick body porcelain disk as a function of initial tempering temperature.	125
4.38	Actual and fictive temperature versus time profiles at the surface and midplane of a 2-mm-thick body porcelain disk quenched in silicone oil from an initial temperature of 850°C.	128
4.39	Transient stresses versus time at the surface and midplane of a 2-mm-thick body porcelain disk quenched in silicone oil from an initial temperature of 850°C.	129
4.40	Residual stress distribution in a 2-mm-thick body porcelain disk quenched in silicone oil from an initial temperature of 850°C.	130
4.41	Actual and fictive temperature versus time profiles at the surface and midplane of a 2-mm-thick body porcelain disk quenched in water from an initial temperature of 850°C.	132
4.42	Transient stresses versus time at the surface and midplane of a 2-mm-thick body porcelain disk quenched in water from an initial temperature of 850°C.	133

Figure	Description	Page
4.43	Residual stress distribution in a 2-mm-thick body porcelain disk quenched in water from an initial temperature of 850°C.	134
4.44	Experimental and calculated cooling profiles for a 2-mm-thick disk subjected to free convective cooling in helium.	136
4.45	Temperature distribution near glass transition temperature within a 2-mm-thick disk subjected to free convective cooling in helium.	137
4.46	Vector plot of thermal fluxes for free convective cooling of a 2-mm-thick disk in helium.	138
4.47	Transient principal stress ($\sigma 1$ in MPa) produced within a 2-mm-thick disk ($\Delta\alpha$ = +3.2 ppm/°C) subjected to free convective cooling in helium (T_i = 982°C).	140
4.48	Transient principal stress ($\sigma 2$ in MPa) produced within a 2-mm-thick disk ($\Delta\alpha$ = +3.2 ppm/°C) subjected to free convective cooling in helium (T_i = 982°C).	141
4.49	Temperature distribution near T_g (600°C) for free convective cooling of a 2-mm-thick disk in air (T_i = 850°C).	142
4.50	Transient principal stress ($\sigma 1$ in MPa) produced within a 2-mm-thick disk ($\Delta\alpha$ = +3.2 ppm/°C) subjected to free convective cooling in air (T_i = 850°C).	143
4.51	Transient principal stress ($\sigma 2$ in MPa) produced within a 2-mm-thick disk ($\Delta\alpha$ = +3.2 ppm/°C) subjected to free convective cooling in air (T_i = 850°C).	144
4.52	Transient principal stress ($\sigma 1$ in MPa) produced within a 2-mm-thick disk ($\Delta\alpha$ = –1.5 ppm/°C) subjected to free convective cooling in air (T_i = 850°C).	145
4.53	Transient principal stress ($\sigma 2$ in MPa) produced within a 2-mm-thick disk ($\Delta\alpha$ = –1.5 ppm/°C) subjected to free convective cooling in air (T_i = 850°C).	146
4.54	Superimposed plots of the deformed and undeformed disk ($\Delta\alpha$ = +3.2 ppm/°C) under the influence of transient thermal and incompatibility stresses.	148

Figure	Description	Page
4.55	Displacements along the vertical direction (mm) for a 2-mm -thick disk ($\Delta\alpha = 0$) subjected to free convection.	149
4.56	Transient principal stress ($\sigma 1$ in MPa) produced within a 2-mm-thick disk ($\Delta\alpha = 0$) subjected to free convective cooling in air (T_i = 850°C).	150
4.57	Transient principal stress ($\sigma 2$ in MPa) produced within a 2-mm-thick disk ($\Delta\alpha = 0$) subjected to free convective cooling in air (T_i = 850°C).	151
4.58	Transient principal stress ($\sigma 1$ in MPa) produced at the surface of a 2-mm-thick disk ($\Delta\alpha = 0$) subjected to free convective cooling in air as a function of radius (T_i = 850°C).	152
4.59	Transient principal stress ($\sigma 2$ in MPa) produced at the surface of a 2-mm-thick disk ($\Delta\alpha = 0$) subjected to free convective cooling in air as a function of radius (T_i = 850°C).	153
4.60	Transient principal stress ($\sigma 1$ in MPa) produced at the edge of a 2-mm-thick disk ($\Delta\alpha = 0$) subjected to free convective cooling in air as a function of thickness (T_i = 850°C).	154
4.61	Transient principal stress ($\sigma 2$ in MPa) produced at the edge of a 2-mm-thick disk ($\Delta\alpha = 0$) subjected to free convective cooling in air as a function of thickness (T_i = 850°C).	156
4.62	Temperature distribution near T_g (600°C) for free convective cooling of a 6-mm-thick disk in air (T_i = 982°C).	157
4.63	Transient principal stress ($\sigma 1$ in MPa) produced within a 6-mm-thick disk ($\Delta\alpha$ = 3.2 ppm/°C) subjected to free convective cooling in air (T_i = 982°C).	158
4.64	Transient principal stress ($\sigma 2$ in MPa) produced within a 6-mm-thick disk ($\Delta\alpha$ = 3.2 ppm/°C) subjected to free convective cooling in air (T_i = 982°C).	159
4.65	Temperature versus time profiles for three selected nodes on the symmetrical axis in a 2-mm-thick disk subjected to tempering in air (T_i = 850°C).	160

Figure	Description	Page
4.66	Temperature distribution near T_g (600°C) in a 2-mm-thick disk subjected to tempering in air (T_i = 850°C).	162
4.67	Transient principal stress ($\sigma 1$ in MPa) produced within a 2-mm-thick disk ($\Delta\alpha$ = 3.2 ppm/°C) subjected to tempering in air (T_i = 850°C).	163
4.68	Transient principal stress ($\sigma 2$ in MPa) produced within a 2-mm-thick disk ($\Delta\alpha$ = 3.2 ppm/°C) subjected to tempering in air (T_i = 850°C).	164
4.69	Transient stress intensity (SI in MPa) produced within a 2-mm-thick disk ($\Delta\alpha$ = 3.2 ppm/°C) subjected to tempering in air (T_i = 850°C).	165
4.70	Transient principal stress ($\sigma 1$ in MPa) produced within a 2-mm-thick disk ($\Delta\alpha$ = –1.5 ppm/°C) subjected to tempering in air (T_i = 850°C).	166
4.71	Transient principal stress ($\sigma 2$ in MPa) produced within a 2-mm-thick disk ($\Delta\alpha$ = –1.5 ppm/°C) subjected to tempering in air (T_i = 850°C).	167
4.72	Transient stress intensity (SI in MPa) produced within a 2-mm-thick disk ($\Delta\alpha$ = –1.5 ppm/°C) subjected to tempering in air (T_i = 850°C).	168
4.73	Transient principal stress ($\sigma 1$ in MPa) produced within a 2-mm-thick disk ($\Delta\alpha$ = 0) subjected to tempering in air (T_i = 850°C).	169
4.74	Transient principal stress ($\sigma 2$ in MPa) produced within a 2-mm-thick disk ($\Delta\alpha$ = 0) subjected to tempering in air (T_i = 850°C).	170
4.75	Transient principal stress ($\sigma 3$ in MPa) produced within a 2-mm-thick disk ($\Delta\alpha$ = 0) subjected to tempering in air (T_i = 850°C).	171
4.76	Transient stress intensity (SI in MPa) produced within a 2-mm-thick disk ($\Delta\alpha$ = 0) subjected to tempering in air (T_i = 850°C).	172
4.77	Transient principal stress ($\sigma 1$ in MPa) at the surface of a 2-mm-thick disk ($\Delta\alpha$ = 0) subjected to tempering in air (T_i = 850°C) as a function of radius.	174

Figure	Description	Page
4.78	Transient principal stress ($\sigma 2$ in MPa) at the surface of a 2-mm-thick disk ($\Delta\alpha = 0$) subjected to tempering in air ($T_i = 850°C$) as a function of radius.	175
4.79	Transient principal stress ($\sigma 1$ in MPa) at the edge of a 2-mm-thick disk ($\Delta\alpha = 0$) subjected to tempering in air ($T_i = 850°C$) as a function of thickness.	176
4.80	Transient principal stress ($\sigma 2$ in MPa) at the edge of a 2-mm-thick disk ($\Delta\alpha = 0$) subjected to tempering in air ($T_i = 850°C$) as a function of thickness.	177
4.81	Temperature distribution near T_g (600°C) for a 2-mm-thick body porcelain disk ($\Delta\alpha = 0$) quenched from an initial temperature of 850°C in silicone oil at a temperature of 100°C.	178
4.82	Vector plot of thermal fluxes for a 2-mm-thick body porcelain disk ($\Delta\alpha = 0$) quenched from an initial temperature of 850°C in silicone oil at a temperature of 100°C.	179
4.83	Transient principal stress ($\sigma 1$ in MPa) within a 2-mm-thick disk ($\Delta\alpha = 0$) quenched from an initial temperature of 850°C in silicone oil at a temperature of 100°C.	180
4.84	Transient principal stress ($\sigma 2$ in MPa) within a 2-mm-thick disk ($\Delta\alpha = 0$) quenched from an initial temperature of 850°C in silicone oil at a temperature of 100°C.	181
4.85	Transient stress intensity (SI in MPa) within a 2-mm-thick disk ($\Delta\alpha = 0$) quenched from an initial temperature of 850°C in silicone oil at a temperature of 100°C.	182
4.86	Transient principal stress ($\sigma 1$ in MPa) at the surface a 2-mm-thick disk ($\Delta\alpha = 0$) quenched in silicone oil as a function of radius.	184
4.87	Transient principal stress ($\sigma 2$ in MPa) at the surface a 2-mm-thick disk ($\Delta\alpha = 0$) quenched in silicone oil as a function of radius.	185
4.88	Transient stress intensity (SI in MPa) at the surface a 2-mm-thick disk ($\Delta\alpha = 0$) quenched in silicone oil as a function of radius.	186

Figure	Description	Page
4.89	Transient principal stress ($\sigma 1$ in MPa) at the edge of a 2-mm-thick disk ($\Delta\alpha = 0$) quenched in silicone oil as a function of thickness.	187
4.90	Transient principal stress ($\sigma 2$ in MPa) at the edge of a 2-mm-thick disk ($\Delta\alpha = 0$) quenched in silicone oil as a function of thickness.	188
4.91	Transient stress intensity (SI in MPa) at the edge of a 2-mm-thick disk ($\Delta\alpha = 0$) quenched in silicone oil as a function of thickness.	189
4.92	Principal stress contours ($\sigma 1$ in MPa) in a ceramic dental crown due to vertically applied loads.	190
4.93	Principal stress contours ($\sigma 1$ in MPa) in a ceramic dental crown due to horizontally oriented loads.	191
4.94	Principal stress contours ($\sigma 2$ in MPa) in a ceramic dental crown due to horizontally oriented loads.	193
4.95	Maximum shear stress contours (τmax in MPa) in a ceramic dental crown due to horizontally oriented loads.	194
4.96	Vector plot of thermal fluxes for a bilayered dental ceramic crown subjected to free convective cooling.	195
4.97	Temperature versus time profiles at the inner and outer surfaces of the bilayered ceramic molar crown ($\Delta\alpha = +3.2$ ppm/°C) subjected to free cooling from an initial temperature of 850°C.	196
4.98	Temperature contours (°C) near the glass transition temperature of 600°C in a bilayered ceramic molar crown ($\Delta\alpha = +3.2$ ppm/°C) subjected to free convective cooling.	197
4.99	Transient stress contours ($\sigma 1$ in MPa) in a bilayered ceramic molar crown ($\Delta\alpha = +3.2$ ppm/°C) subjected to free convective cooling from an initial temperature of 850°C.	198
4.100	Transient stress contours ($\sigma 2$ in MPa) in a bilayered ceramic molar crown ($\Delta\alpha = +3.2$ ppm/°C) subjected to free convective cooling from an initial temperature of 850°C.	199
4.101	Displacement contours (mm) along horizontal direction in a bilayered ceramic molar crown ($\Delta\alpha = +3.2$ ppm/°C) subjected to free convective cooling from an initial temperature of 850°C.	201

Figure	Description	Page
4.102	Temperature versus time profiles for the inner and outer surfaces of the bilayered ceramic molar crown ($\Delta\alpha = +3.2$ ppm/°C) subjected to tempering from an initial temperature of 850°C.	202
4.103	Temperature contours (°C) near the glass transition temperature of 600°C for a bilayered ceramic crown tempered from an initial temperature of 850°C.	203
4.104	Transient stress contours (σ_1 in MPa) in a bilayered ceramic molar crown ($\Delta\alpha = +3.2$ ppm/°C) tempered from an initial temperature of 850°C.	204
4.105	Transient stress contours (σ_2 in MPa) in a bilayered ceramic molar crown ($\Delta\alpha = +3.2$ ppm/°C) tempered from an initial temperature of 850°C.	205
4.106	Transient stress contours (σ_3 in MPa) in a bilayered ceramic molar crown ($\Delta\alpha = +3.2$ ppm/°C) tempered from an initial temperature of 850°C.	206
4.107	Displacement contours (mm) along horizontal direction for a bilayered ceramic crown ($\Delta\alpha = +3.2$ ppm/°C) tempered from an initial temperature of 850°C.	207
4.108	Temperature contours (°C) near the glass transition temperature of 600°C for a ceramic crown tempered from an initial temperature of 750°C.	208
4.109	Transient stress contours (σ_1 in MPa) in a bilayered ceramic molar crown ($\Delta\alpha = +3.2$ ppm/°C) tempered from an initial temperature of 750°C.	210
4.110	Transient stress contours (σ_2 in MPa) in a bilayered ceramic molar crown ($\Delta\alpha = +3.2$ ppm/°C) tempered from an initial temperature of 750°C.	211
4.111	Transient stress contours (σ_3 in MPa) in a bilayered ceramic molar crown ($\Delta\alpha = +3.2$ ppm/°C) tempered from an initial temperature of 750°C.	212

Figure	Description	Page
4.112	Displacement contours (mm) along horizontal direction in a bilayered ceramic crown molar crown ($\Delta\alpha$ = + 3.2 ppm/°C) tempered from an initial temperature of 750°C.	213
4.113	Temperature contours (°C) near the glass transition temperature of 400°C for a ceramic molar crown tempered from an initial temperature of 850°C.	214
4.114	Transient stress contours (σ1 in MPa) in a bilayered ceramic molar crown ($\Delta\alpha$ = + 3.2 ppm/°C) tempered from an initial temperature of 850°C assuming a glass transition temperature of 400°C.	216
4.115	Transient stress contours (σ2 in MPa) in a bilayered ceramic molar crown ($\Delta\alpha$ = + 3.2 ppm/°C) tempered from an initial temperature of 850°C assuming a glass transition temperature of 400°C.	217
4.116	Transient stress contours (σ3 in MPa) in a bilayered ceramic molar crown ($\Delta\alpha$ = + 3.2 ppm/°C) tempered from an initial temperature of 850°C assuming a glass transition temperature of 400°C.	218
4.117	Transient stress contours (σ1 in MPa) for a tempered ceramic crown ($\Delta\alpha$ = 0) from an initial temperature of 850°C using a glass transition temperature of 600°C.	219
4.118	Transient stress contours (σ2 in MPa) for a tempered ceramic crown ($\Delta\alpha$ = 0) from an initial temperature of 850°C, using a glass transition temperature of 600°C.	220
4.119	Transient stress contours (σ3 in MPa) for a tempered ceramic crown ($\Delta\alpha$ = 0) from an initial temperature of 850°C using a glass transition temperature of 600°C.	221
4.120	Transient stress intensity (SI in MPa) for a tempered ceramic crown ($\Delta\alpha$ = 0) from an initial temperature of 850°C using a glass transition temperature of 600°C.	222
4.121	Transient stress contours (σ1 in MPa) for a tempered ceramic crown ($\Delta\alpha$ = 0) from an initial temperature of 850°C using a glass transition temperature of 400°C.	223
4.122	Transient stress contours (σ2 in MPa) for a tempered ceramic crown ($\Delta\alpha$ = 0) from an initial temperature of 850°C using a glass transition temperature of 400°C.	224

Figure	Description	Page
4.123	Transient stress contours (σ_3 in MPa) for a tempered ceramic crown ($\Delta\alpha = 0$) from an initial temperature of 850°C using a glass transition temperature of 400°C.	225
4.124	Transient stress intensity (SI in MPa) for a tempered ceramic crown ($\Delta\alpha = 0$) from an initial temperature of 850°C using a glass transition temperature of 400°C.	226
4.125	Mean flexure strength for disk specimens cooled in air from various initial temperatures.	235
4.126	Mean biaxial flexure strength for tempered disks as a function of initial tempering temperature.	236

NOMENCLATURE

Symbol	Description
A	Convective surface area
a	Thickness of porcelain disk
a_h	Half thickness of a porcelain plate
a_p	Projected half-diagonal length of indentation
$Bi = \frac{L_c h_c}{K}, \frac{a\ h}{K}, \frac{R\ h}{K}$	Biot number
C	Crack size (half crack length)
C_{sc}	Crack size for slowly cooled disks
C_P	Constant pressure specific heat
D	Disk diameter
E	Elastic modulus
e	Emissivity
g	Acceleration due to gravity
$h, h_t = h_c + h_r$	Heat transfer coefficient
h_c	Convective heat transfer coefficient
h_r	Radiative heat transfer coefficient
$H = 0.47 \frac{P}{a_p^2}$	Hardness
$J_n(x)$	Bessel function of first kind of order n
K	Thermal conductivity of a solid body
K_m	Thermal conductivity of cooling medium
K_c	Fracture toughness
L_c	Characteristic length
$Nu = \frac{h\ L_c}{K_m}$	Nusselt number
P	Applied load
P_f	Applied load at failure
P_s	Perimeter
$Pr = \frac{\mu\ C_p}{K_m}$	Prandtl number
$\dot{Q}$	Heat flow rate
Q_C	Heat loss by convection
R	Radius of porcelain disk

Symbol	Description
$R(x,t)$	Axillary function
Ra	Rayleigh number
$Re = \frac{V R}{\nu}$	Reynolds number
R_o	Radius of piston used for biaxial flexure test
R_s	Radius of support base of biaxial flexure test device
T	Temperature (°C)
T_a	Ambient temperature
$T_{fm} = \frac{T_s+T_a}{2} + 273.2$	Film temperature (°K)
T_f	Fictive temperature
T_g	Glass transition temperature
T_i	Initial temperature
T_s	Surface temperature
T_u, T_t, T_r, T_{rr}, T_{xx} , T_z, T_{zz}	Partial derivatives of temperature with respect to the corresponding variables
t	Time
t_n	Time at step n
V	Volume
X	Distance along horizontal axis
Z	Distance along vertical axis
α	Thermal contraction coefficient
α_g	Thermal contraction coefficient at glassy state
α_l	Thermal contraction at liquid state
α_{th}	Free thermal contraction
β_n , γ_n , ξ_n	Roots of the corresponding transcendental equation
ε	Strain
$\varepsilon(t_{n-1})$	Strain at time step t_{n-1}
$\gamma = \frac{\mu}{\rho}$	Kinematic viscosity
$\eta = \frac{R}{r}$	Dimensionless distance for r direction
$\kappa = \frac{K}{\rho C_p}$	Thermal diffusivity
μ	Dynamic viscosity

Symbol	Description
ν	Poisson's ratio
$\theta = \frac{T-T_a}{T_i-T_a}$	Dimensionless temperature
ρ	Density
ρ_c	Radius of curvature at crack tip
σ_F	Flexural strength
σ	Stress
σ_{SB}	Stefan-Boltzmann constant
$\tau = \frac{t\,\alpha}{a\,R}$, $\frac{t\,\alpha}{a^2}$	Dimensionless time
χ	Dimensionless indentation constant
$\zeta = \frac{Z}{a}$	Dimensionless distance in z direction

Abstract of Dissertation Presented to the Graduate School
of the University of Florida in Partial Fulfillment of the Requirements
for the Degree of Doctor of Philosophy

THERMAL TEMPERING OF LAYERED CERAMIC STRUCTURES

By
Bahram Hojjatie

May, 1990

Chairman: Dr. Ulrich H. Kurzweg
Cochairman : Dr. Kenneth J. Anusavice
Major Department: Aerospace Engineering, Mechanics and Engineering Science

This study was designed to test the hypothesis that thermal tempering by compressed air is the most effective strengthening method for layered feldspathic porcelain structures and to determine the influence of cooling method, initial tempering temperature, thermal contraction mismatch, and specimen thickness on transient and residual stresses produced within dental ceramic structures.

Bilayered porcelain disks with a thermal contraction mismatch between –1.5 and +3.2 ppm/°C and a thickness of 2 or 6 mm were prepared and thermally tempered in air, helium, and silicone oil. The transient temperature distributions were calculated by analytical and finite element methods and were incorporated in finite element and viscoelastic thermal stress models to determine the transient and residual stresses produced in each disk. The finite element method was also employed to determine the influence of ceramic thickness, loading orientation, thermal contraction mismatch, initial tempering temperature and cooling rate on the stress distribution within a dental ceramic molar crown. Statistical analysis revealed that forced convective cooling of disk specimens in air resulted in a significantly smaller induced crack size and increased the mean flexural strength on specimens by a factor of two compared with the specimens which were conventionally-cooled by

free convection. However, the thermal stress models predicted transient tensile stresses far above the failure level of porcelain for the 6-mm thick bilayered disks subjected to free convective cooling and for the 2-mm thick bilayered disks subjected to quenching at high initial temperatures in silicone oil. These predictions were supported by experimental findings. The results of this study support the hypothesis that thermal tempering by compressed air is the most effective strengthening method for layered feldspathic porcelain structures. However, variables such as specimen dimensions, initial tempering temperature, heat transfer coefficient, and thermal contraction mismatch have a significant influence on the effectiveness of tempering. The most effective tempering treatment, which results in maximum flexure strength and minimum structural distortion by viscous flow and air blasting, was achieved by forced convective cooling in air using initial tempering temperatures between 750°C and 850°C.

CHAPTER I
INTRODUCTION

Strengthening of Glass

Influence of Flaws on Strength

Microcracks and critical flaws which act as stress concentrators, reduce the strength of brittle materials. The interaction of these flaws with applied forces on structures can cause either premature fracture or crack growth which endangers the integrity of these structures. The theoretical tensile strength of a flawless glass can be as high as 1400 MPa, but because of the surface stress raisers which usually are present, the strength may be reduced to 70 MPa [1]. Defects and cracks can be produced from grinding, machining, handling, impact forces, and thermal stresses. Studies of the failure mechanisms in glass have been conducted for several hundred years. In 1678, Hooke included glass in his experiments which led to the famous stress-strain law for solid bodies. A historical review of glass strength factors and failure mechanisms is given by Holloway [2].

Inglis in 1913 showed that for a flaw represented by a long and narrow elliptical hole in a glass plate, the stress at the flaw tip increases by a factor of $2\,(C/\rho_c)^{1/2}$, where C and ρ_c are the half crack length (semimajor axis of an ellipse) and radius of curvature at the crack tip, respectively [3]. However, because the radius (ρ_c) of a crack tip is generally of atomic dimensions and is difficult to measure, many workers have assumed that it is constant for cracks of different length [4-5]. Griffith [6] made a very important theoretical contribution

to the understanding of brittle fracture by demonstrating that, for a given value of applied force, a crack will propagate and cause fracture only if it has a length greater than a certain value called the critical crack length and this is determined by energy considerations. The strength of brittle materials is significantly influenced by the number and severity of the flaws and cracks, specifically those that are located at the surface regions [5-12]. Sapphire crystals after normal handling have a flexural strength in the range of 350-700 MPa, but when the critical surface flaws are reduced by flame polishing, the strength increases to 10,000 MPa [13]. However, this technique is impractical in many cases because the material will be subjected to surface damage in use.

Although it is difficult to maintain the surface of brittle materials completely free of flaws and microcracks, it is possible to significantly reduce the effect of these surface stress raisers by producing compressive stresses in a thin layer near and parallel to the surface. These stresses which are present in the unloaded state should act over a distance from the surface which is greater than the depth of the deepest surface flaw. If a compressive stress of 70 MPa is produced at the surface of a glass plate which has a tensile strength of 70 MPa, its strength can be increased by up to a factor of two, because any tensile forces applied at the surface of this plate must first overcome the existing compressive stresses before causing any tension at the surface. Compressive stresses can be produced at the surface by the use of a thermal tempering treatment, which is a well-established technique in the glass industry.

In general, strengthening by surface compression (tempering) can be classified into two main categories: 1) chemical tempering, and 2) physical tempering [1].

Chemical Tempering

In chemical tempering techniques such as the Schott overlay process, surface crystallization and ion-exchange, surface compression is produced by modifying the chemical composition of the surface [14,15]. In the Schott process, glass with a relatively larger thermal expansion coefficient is sealed within a smaller thermal expansion glass. When the composite glass structure cools from an elevated temperature, the interior, which contracts more than the exterior, causes the development of compressive stresses at the surface. This process is currently being used to produce glass-ceramic dinnerware. Krohn and Copper [16] used this technique to produce cladded fibers by placing a solid rod of high thermal expansion glass inside a tube of low expansion glass. The mean strength of fibers drawn from this composite increased to 290 MPa compared with 138 MPa for the untreated fibers.

Surface crystallization forms a layer with a lower thermal expansion coefficient compared with the interior and develops compressive stresses in the surface as glass is cooled. In most glasses, this technique may weaken the sample because it introduces tensile stresses or cracks. Also it may result in surface opacity and poor optical properties. However, certain lithium-aluminosilicate systems can be treated in this manner to achieve a strength of about 690 MPa [15]. For strengthening of a 0.5-cm diameter lithium-aluminosilicate rod the optimum thickness of the compressive surface layer was found to be 0.07 mm. When the crystallization process was continued too long, it produced large tensile stresses which resulted in failure of the specimen [5].

Toughening of glass by ion-exchange is accomplished when a large ion is exchanged for a smaller one at temperatures below the glass transition

temperature. As a result of this ion transport, compressive stresses build up in the exchanged region. In this technique, glass is immersed in a molten salt bath containing potassium ions. Sodium ions diffusing from surface into the fused salt are replaced by an equal number of larger potassium ions. The surface compressive stresses develop because of the difference in size between the alkali ions which increase the local density of surface-near regions. The larger potassium ions try to expand the surface but this is resisted by the chemically unchanged interior region which puts the surface in compression [17]. It is possible to combine ion-exchange and surface crystallization for some glasses to enhance the effectiveness of chemical tempering. Above the glass transition temperature, surface crystallization which occurs as a results of ion-exchange can reduce the thermal expansion coefficient of the surface layer. This develops larger compressive stresses at the surface [5].

Physical Tempering

In physical tempering (thermal tempering), rapid cooling of glass at an initial temperature above the glass transition causes the glass surface to cool before the interior region. During the initial stage of the tempering process, the surface becomes rigid and contracts, while the interior is still soft and can adjust its dimensions to the surface contraction. Cooling is most often accomplished by jets of air or sometimes by an oil bath [18]. At the later stages of tempering, the interior temperature drops below the glass transition temperature and it will contract. However, the surface is rigid and cannot adjust itself to the interior contraction. Since the volume elements at the surface are constrained from any expansion or contraction, compressive stresses are produced at the surface, simultaneously balancing tensile stresses of smaller magnitude which are

developed in the interior regions. This effect can be enhanced by coating a glass with another one of lower thermal expansion coefficient [5]. Precompression of the glass surface is based on the unique behavior of glass in the transformation temperature range during cooling where its properties change from that of a viscous liquid to that of an elastic body [19-34].

The initial idea of tempering glass goes back to the 17th century when experiments were conducted to produce the so-called "Prince Rupert's Drops" [20]. To produce these drops, molten glass is subjected to a water quench which produces a tear-shaped glass drop with a long tail. Since the exterior surface of this molten drop cools before the interior, large compressive stresses are induced on the surface, while the interior is under tension. As a result, the body of "Prince Rupert's Drop" becomes so strong that it cannot be broken by relatively large compressive forces applied by a hammer. However, the drop will burst in a quite rapid and violent manner when tensile stresses are applied by twisting its tail. This is similar to the less explosive fracture which occurs when a tempered car windshield breaks into a large number of fragments a few millimeters in size [17].

One of the earliest tempering experiments for glass plates was performed by Siemens [35], who introduced the method of quenching by contact with solid surfaces. However, most of the studies on controlling thermal stresses in glass prior to 1920 were related to annealing in which the residual stresses in glass products were removed by slow cooling in an annealing oven. In 1920 the method of quenching flat glass with impinging air jets was invented in France, and in early 1930 thermally tempered safety glass began to be widely used in European automobiles. When a toughened windshield glass breaks in the presence of tensile stresses at the interior, it breaks into small pieces which are

relatively harmless. In tempered automotive glass, one usually seeks high strength and, upon fracture, small fragments to minimize physical injury from glass shards. However, in the tempered glass used in some architectural applications and in ovenware, increased strength and, upon fracture, large fragments are desirable. The enhancement in the strength of tempered glass is determined by the magnitude of compressive stresses in its surface while the propensity to break into many small fragments is believed to be governed by the magnitude of the interior tension. Perhaps the most extensive analytical and experimental studies on tempering of glass in the United States have been conducted by Robert Gardon. In a recent study [24], Gardon has shown that the strength and fracture characteristics of tempered glass can be controlled independently by programming the heat transfer coefficient of air flow during the tempering process. In this technique, which is called "modulated quenching," the ratio of surface compression to interior tension is controlled.

Comparison Between Chemical and Physical Tempering

Doremus [5] has reported that glass can be strengthened by a factor of 17 for surface crystallization, 10 for ion-exchange, 22 for combined ion-exchange and surface crystallization, and 6 for thermal tempering. However, the effectiveness of a tempering technique depends on factors such as its ability to maintain the strength over a long period of time under a variety of loading conditions, the time and the cost required for strengthening, the convenience of the process, and the simplicity of the method.

Compared with thermal tempering, chemical tempering provides a greater degree of flexibility in overcoming physical design problems such as size and

shape restrictions. Since the chemical exchange process is carried out at lower temperatures, there is no danger of distortion resulting from viscous flow of glass. However, compared with the thermal tempering, chemically strengthened glass is more susceptible to abrasion, is less flexible in terms of chemical composition, is more expensive and the processing is longer.

Shown in Fig 1.1 is the difference between the residual stress profiles produced by ion-exchange and thermal tempering [1]. Although the chemical tempering produces greater compressive stresses at the surface and smaller tensile stresses at the interior, the compressive stresses are developed only in a thin layer near the surface and the tensile stresses at the interior regions are extended dangerously close to the surface layer [1].

Major Findings from Thermal Tempering of Glass

Gardon has employed cinematography to record the transient photoelastic fringe patterns corresponding to the transient stress distributions in a 6.1 mm thick glass plate during the tempering process. The stress profiles for the first 20 seconds of quenching are shown schematically in Fig. 1.2. For a constant heat transfer coefficient of 222 $W/m^2 \cdot K$, stresses are influenced by the initial tempering temperature. At the final stage of tempering, the stress distribution is parabolic with the surface in compression and the interior in tension. However, it is important to notice that the surface stresses at the initial stage of tempering may be tensile or compressive depending on the initial tempering temperature (T_i). At low T_i values of 616°C and 648°C (cases A and B), the surface initially sustains tensile stress which subsequently changes to a state of compression, while at a higher initial temperature of 738°C (case C), it passes directly from an initially stress-free

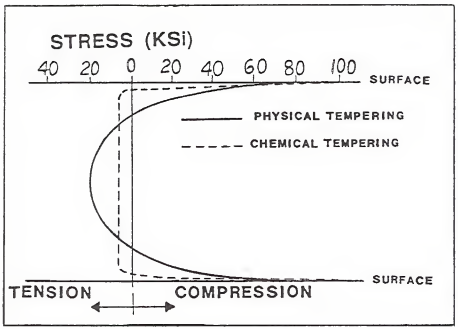

Fig. 1.1 Residual stress distribution in glass resulting from physical (thermal) and chemical tempering [1].

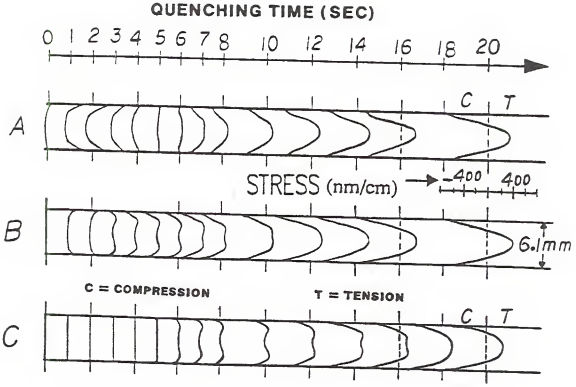

Fig. 1.2 Transient stress distribution in glass plate during tempering from initial temperatures of 616°C (A), 648°C (B) and 738°C (C) [20].

condition into compression. The effect of heat transfer coefficient and specimen thickness on midplane tension in a flat glass has also been reported by Gardon [20] using the birefringence technique. At a constant initial temperature of 650°C, when the heat transfer coefficient in air was increased from 12.5 $W/m^2 \cdot K$ (free convection) to 552 $W/m^2 \cdot K$ (forced convection), the midplane tension was increased by a factor of 6.9. For the same initial temperature, an increase in specimen thickness from 2.1 mm to 26.5 mm resulted in an increase in the midplane tension by a factor of 8.5. Although the surface compression which enhances the strength of tempered specimens had been taken previously as 2.0 to 2.2 times greater than the midplane tension, the actual ratio of surface compression to midplane tension may be considerably different for different materials and cooling conditions.

Gardon [20] has also shown that for a constant glass thickness and heat transfer coefficient, a limiting value for the initial cooling temperature exists such that an increase in that temperature before quenching will not result in any further increase in the magnitude of induced surface compression (Fig. 1.3). However, as previously stated, the development of transient tensile stresses at the initial stage of tempering depends on the initial temperature. For moderate quenching conditions with a heat transfer coefficient of 222 $W/m^2 \cdot K$, which is representative of industrial practice for tempering of 6-mm-thick glass, an initial temperature of 648°C produced tensile stresses at the surface during the initial stage of tempering (Fig. 1.2), while tempering from an initial temperature of 738°C did not produce any surface tensile stresses. Fig. 1.3 also indicates that for a fixed value of initial temperature and specimen thickness, an increase in the heat transfer coefficient will result in a greater degree of tempering. These results show that the beneficial effect

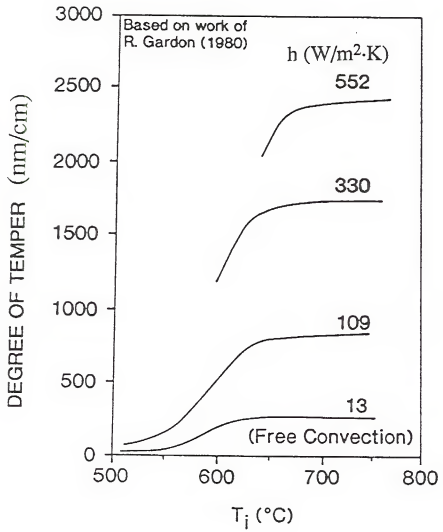

Fig. 1.3 Degree of temper (nm/cm) in a glass plate as a function of initial temperature and heat transfer coefficient [20].

of quenching is strongly related to the heat transfer coefficient and the initial temperature employed in the tempering treatment.

Strengthening of Ceramics

By comparison of the color and texture of many of the prehistoric tools and weapons made from Ocala chert, anthropologists have empirically determined that prehistoric Indians performed heat treatment on this ceramic to obtain smoother fracture surfaces and sharper edges [36,37]. Ceramic materials in general have desirable properties for structural design such as thermodynamic stability, resistance to corrosion, low density, high melting point and reliable performance at high temperatures. However, they exhibit a high degree of brittleness, low impact resistance, and high sensitivity to surface damage which may result in their failure without prior warning.

Based on the success with the thermal tempering of glass which produces beneficial compressive stresses at the surface, substantial progress has also been made in strengthening ceramics. Mechanical strength, resistance to thermal shock failure and impact of some polycrystalline ceramics such as alumina have been improved by thermal tempering [38]. Thermal tempering can assist in the more widespread use of ceramics in engineering applications such as in energy conversion and within the aerospace industry. High temperature strength and the smaller density of ceramics compared with metal can result in a significant improvement in performance, thermodynamics and overall efficiencies in heat engines.

Several authors have discussed factors which influence the design procedures required for the successful applications of ceramics in thermal and

structural equipment such as gas turbines, heat exchangers, automobile engines and refractory metals [39-43]. Although a wide range of strengthening mechanisms or processes such as annealing and minimizing grain size have been identified for ceramics, in most cases the improvements have been unimpressive except for the results obtained by using compressive surface stresses such as glazing and thermal tempering. Most pottery and chinaware are glazed with a layer that has a lower thermal expansion coefficient. During cooling, the interior tends to contract more than the glaze, which put the glaze layer in compression and the interior into tension.

Major Finding from Thermal Tempering of Ceramics

Studies have shown that tempering improves the strength of various ceramic materials [44-46]. Kirchner et al. [47], conducted experiments by quenching both glazed and unglazed alumina rods (96% alumina), using gaseous cooling media such as air, helium, and CO_2 (forced convective cooling), and liquid cooling media such as silicone oil with various kinematic viscosity, kerosene and water (free convective cooling). The mean value of the flexural strength using a four-point bending test for the untreated (control) specimens was 322.7 MPa. The corresponding values for specimens quenched in low viscosity silicone oil from an initial temperature of 1600°C and by forced helium from an initial temperature of 1500°C were 728.3 MPa and 522.4 MPa, respectively. However, quenching the specimens in water caused thermal shock failure. Shown in Table 1.1 is a summary of the results obtained when quenching alumina in various media.

Table 1.1 Flexural strength of 96% alumina quenched in various media [47].

QUENCHING MEDIUM	QUENCHING TEMPERATURE (°C)	NO. OF SPECIMENS	STRENGTH (MPa)
As-received (control)	-------	19	322.7
Silicone oil (γ = 5.0 cs)	1600	5	728.3
Silicone oil (γ = 12,500 cs)	1550	5	593.8
Water (Thermal Shock)	1600	3	35.9
10% oil + 90% H_2O	1550	3	640.7
Forced air	1500	5	533.8
Forced helium	1500	5	522.4

Significant improvements were also obtained in tensile strength, thermal shock resistance and impact resistance of tempered compared with slowly cooled specimens. Thermal shock tests were performed by quenching the specimens in water at room temperature and measuring the remaining flexural strength after one thermal shock cycle. Impact resistance was measured by dropping a weight from progressively greater heights onto a specimen until a height was reached at which the specimen failed. The residual and flexural stress profiles for 96% alumina quenched in silicone oil from an initial temperature of 1600° C are shown in Fig. 1.4a. Compressive surface stresses produced by tempering have reduced the flexural tensile stress from 724 MPa to 330 MPa (Fig. 1.4b).

In a more recent study by Travitzky et al. [48], tiles of structural alumina at various initial temperatures were subjected to tempering in forced air. After

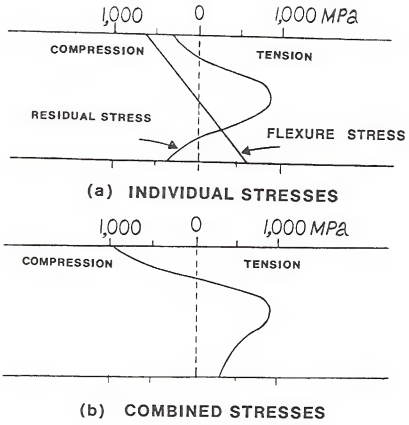

Fig. 1.4 Stress distribution at rupture for alumina bars quenched in silicone oil from an initial temperature of 1600°C [47].

tempering, a diamond saw was used to cut the tiles to produce rectangular bars for mechanical testing. The mean value of flexural strength (three-point bending) of tempered specimens at an initial temperature of 1400°C increased to 430 MPa compared with the 225 MPa reported value for the untempered samples. This study also showed that the flexural strength increased significantly with initial tempering temperature. However, at initial quenching temperatures above 1400°C, the strength no longer increased (Fig. 1.5).

Strengthening of Dental Ceramics

Background

Dental porcelain frits consist of fine powders that are formed into a paste by mixing them with water. The desired shape is then fired at maturing temperatures as high as 1300°C to produce a ceramic restoration with color and shade similar to human teeth. Due to loss of water and a sintering process (fusion of the porcelain powder to form a continuous mass), the porcelain may shrink during firing as much as 40 percent by volume. The firing technique has a pronounced effect on the strength and quality of the resultant dental restorations. The major mineral constituent of a high temperature maturing porcelain is feldspar ($Na_2O{\cdot}Al_2O_3{\cdot}6SiO_2 + K_2O{\cdot}Al_2O_3{\cdot}6SiO_2$), which may contain as much as 36% alumina (Al_2O_3) by volume [49]. Similar to other types of ceramic materials, dental porcelain exhibits brittle fracture and because of surface irregularities, it has low tensile strength.

Shown in Table 1.2 are comparative physical properties of glass and two types of dental ceramics [5, 18, 50, 51].

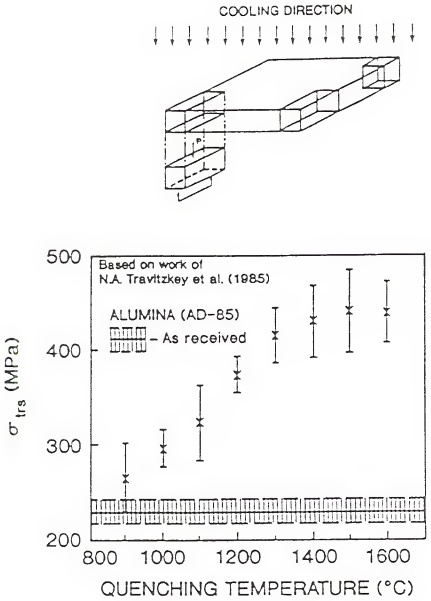

Fig. 1.5 Flexural strength of tempered alumina as a function of initial tempering temperature [48].

Table 1.2- Physical properties of glass and dental ceramics.

Material	Specific Gravity (g/cm^3)	Thermal Diffusivity (mm^2/sec)	Modulus of Elasticity (GPa)	Compressive Strength (MPa)	Tensile Strength (MPa)
Glass	2.4	0.57	72.0	383	30-100
Castable Ceramic	2.7	0.80	70.3	828	34-69
Porcelain	2.4	0.64	70.3	172	34-69

To overcome the limitations associated with the mechanical properties of porcelain and to improve the structural integrity of dental crowns and bridges, Weinstein et al. [52,53] in 1962 developed an alloy that chemically bonds to porcelain. Since then, construction of the majority of dental restorations has been based on porcelain-fused-to-metal systems. However, structural failure of these prostheses as well as all-ceramic restorations still occur despite the introduction of more compatible systems and improvements in laboratory techniques. For a glass-ceramic molar crown, Moffa [54] has reported a failure rate of 35.3% during the first three years which indicates that there is a need for the development of new dental materials with improved mechanical and thermal properties. However, at the present time it seems more practical to focus on the development of better laboratory techniques to improve the design of dental restorations using the existing materials rather than altering their chemical composition to produce new materials. This focus on existing materials is justified because all conditions required for biological compatibility, mechanical and handling properties, esthetics and economics should be satisfied before any new material can be used clinically.

Influence of Crown Design on Stress Distribution

Several studies have analyzed the stress distribution in dental restorations due to mechanical loading in order to improve the design and enhance the structural integrity of these prostheses [51,55–63]. In our previous studies [51,58,59], we have shown that the stress distributions in metal-ceramic crown or in all-ceramic crowns are not significantly influenced by small changes in metal or ceramic thicknesses at some locations. Since the introduction of castable ceramics in 1982, several studies have focused on optimizing the design of all-ceramic crowns based on finite element stress analysis. These ceramics are sometimes preferred to metal-ceramic crowns for restorations of anterior teeth because of their improved aesthetic potential.

We have analyzed [51] the stress distribution induced by applied loads in three different maxillary ceramic crown designs with variable thickness of ceramic in the incisal region (Fig. 1.6). The incisal edges of ceramic for these designs were located at distances of 1.0 mm (case I), 1.9 mm (case II) and 4.0 mm (case III) from the incisal edges of the prepared teeth. Figs. 1.7 and 1.8 show the influence of ceramic thickness and loading orientation on peak tensile stress in the ceramic and the cement layer. The locations in which these stresses were obtained are also shown in these figures. Comparison of the maximum principal stresses induced in ceramic and dentin for cases I and III indicates that the increase of ceramic thickness from 1.0 to 4.0 mm in the incisal region has a negligible effect on stress distributions. However, the influence of loading orientation on the induced stresses is significant. A 200-newton load was distributed at the lingual region along vertical and horizontal directions, and also

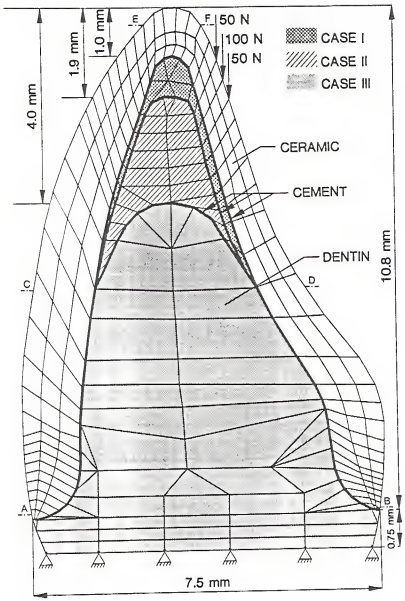

Fig. 1.6 Two-dimensional finite element model of a prepared central incisor restored with each of three ceramic crown designs [51].

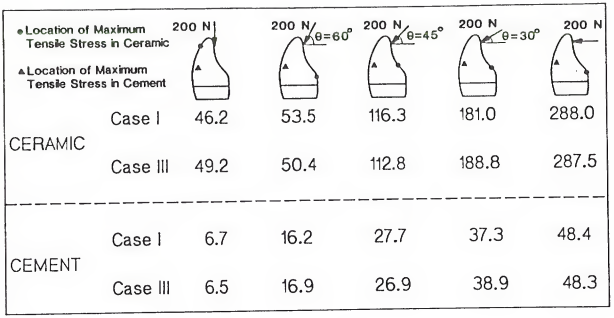

CERAMIC	Case I	46.2	53.5	116.3	181.0	288.0
	Case III	49.2	50.4	112.8	188.8	287.5
CEMENT	Case I	6.7	16.2	27.7	37.3	48.4
	Case III	6.5	16.9	26.9	38.9	48.3

Fig. 1.7 Maximum tensile stress (MPa) for crowns with ceramic thickness of 1.0 mm and 4.0 mm produced by an external load [51].

▪ Locations of Maximum Compressive Stress in Ceramic and Cement		200 N	200 N, θ=60°	200 N, θ=45°	200 N, θ=30°	200 N
CERAMIC	Case I	44.7	218.0	284.5	331.9	356.6
	Case III	45.2	227.4	287.0	346.3	356.0
CEMENT	Case I	112.0	224.0	289.5	335.3	356.3
	Case III	112.2	233.0	290.0	348.7	355.2

Fig. 1.8 Maximum compressive stress (MPa) for crowns with ceramic thickness of 1.0 mm and 4.0 mm [51].

at angles of 30°, 45°, and 60° to the horizontal axis. Maximum tensile stresses in ceramic and cement at various locations in the crown were plotted (Fig. 1.9) as a function of the angle of the load to the horizontal axis. When the load was applied along a horizontal direction, the maximum tensile stresses in ceramic and cement were 288 MPa and 47.4 MPa, respectively. These values were much greater than the published tensile strength values [59] for porcelain and cement. The maximum principal stresses in ceramic and cement increased as the load orientation changed from a vertical to a horizontal orientation. For Dicor, a tetrasilic fluormica glass-ceramic ($KMg_{2.5}Si_4O_{10}F_2$), Moffa [54] reported a failure rate of anterior crowns of 3.5% during the first three years. This is a relatively small rate of failure which indicates that such a horizontal loading condition analyzed by finite element methods occurs only under extraordinary conditions.

The major assumption that was required in this plane stress model was that all vertical planes which cross through the crown (sections parallel to the section shown in Fig. 1.6) have identical stress distributions due to a given force. In general, a plane-stress distribution corresponds to a thin plate which is loaded by forces applied at the plate boundary, parallel to the plane of the plate, and distributed uniformly over the plate thickness. Such an ideal case does not exist in a ceramic crown under the influence of intraoral forces. A three-dimensional model would yield more accurate stress values compared with a two-dimensional model. However, the two-dimensional model employed in this study [51] can be used for a relative comparison of various design geometries.

Hojjatie and Anusavice [64] have developed a three-dimensional finite element model to determine the strength of posterior ceramic crowns with various designs and to analyze the influence of loading orientation and occlusal thickness on the level of tensile stresses under simulated applied loads. The results of the

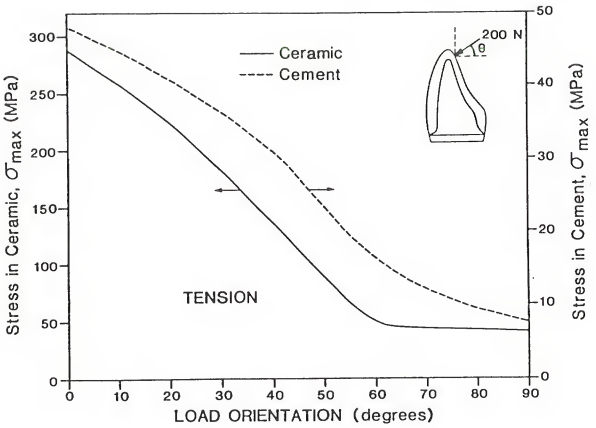

Fig. 1.9 Peak values of principal stresses (σ_{max}) in ceramic and cement as a function of load orientation [51].

finite element stress analyses of ceramic crowns indicated that under the influence of horizontally applied loads, relatively large tensile stresses were developed in ceramic despite the changes in the crown designs. Therefore, to increase the longevity of dental restorations under intraoral conditions, a combination of strengthening techniques such as tempering and design modifications should also be pursued.

Tempering of Dental Ceramics

The potential benefit of thermal tempering of dental ceramic structures was identified several years ago [49]. The first extensive experimental and theoretical investigations on this research topic have only recently been reported [65–69]. These studies have focused on analysis of the effectiveness of this technique when it is used for strengthening of dental porcelain. In one of these studies [65], it was reported that air blasting of feldspathic porcelain can significantly improve the resistance to crack development within the tempered surface. However, the effect of transient tensile stresses which are developed at the surface of porcelain during the initial stage of tempering was not investigated. If transient tensile stress results in crack initiation and/or propagation, it could negate the beneficial effect of the tempering treatment.

This same study [65] has shown that the mean crack size induced by a microhardness indenter in tempered specimens was significantly smaller than those for the conventionally cooled specimens. This suggests that the surface compressive stress produced by tempering decreases the growth rate of surface cracks; therefore, this procedure can improve the overall strength of layered ceramics. However, several variables such as the cooling medium, specimen geometry, initial tempering temperature, heat transfer coefficient, and other

thermal properties of ceramic materials can influence the effectiveness of the tempering treatment.

The development of transient tensile stresses in ceramic surfaces during the initial stage of tempering for some cooling conditions may result in crack initiation and growth. Also, the effect of residual tensile stresses which are produced within the interior of tempered ceramics on the overall strength of restorations must be determined. Studies on tempering of glass plates indicate that the ratio of surface compressive stress to mid-plane tensile stress increases with the initial tempering temperature and the heat transfer coefficient [20]. In addition, the initial temperature should be kept low enough to prevent anatomical distortion of the dental prostheses due to viscous flow, and the surface heat transfer coefficient should be kept small enough to avoid fracture due to thermal shock. The transient and residual stresses can be calculated based on viscoelastic analysis or elastic analysis using analytical approaches and finite element methods.

Stress Analysis by Viscoelasticity and Structural Relaxation

DeHoff and Anusavice [66] have developed an analytical model to calculate transient and residual stress distribution in dental porcelain plates subjected to cooling rates used in commercial laboratories. By incorporating linear viscoelasticity, structural relaxation characteristic of porcelain, and an assumed glass transition temperature (T_g) of 400°C in the analytical model, they have shown that for symmetrical cooling of a 2-mm-thick porcelain plate, an increase in initial cooling temperature from 700°C to 800°C does not change the stress distribution significantly. In general, relatively low compressive stresses were calculated at the surfaces of porcelain. At an initial temperature of 800°C and heat

transfer coefficients of 56.8, 113.6 and 170.3 $W/m^2.K$, the stresses were 26.4, 17.6 and 8.5 MPa, respectively. The viscoelastic method requires identification of a glassy and a liquid state for porcelain from the thermal expansion/contraction data. For the assumed T_g value of 400°C, the following linear relations were determined from the experimental dilatometry data:

Glassy State : $\alpha_g(t) = a_0 + a_1 T$ at $T_a \leq T \leq T_g$ (1)

Liquid State : $\alpha_l(t) = a_2 + a_3 T$ at $T_g \leq T \leq T_i$ (2)

where T_a and T_i are the ambient and initial cooling temperatures of porcelain, respectively. DeHoff and Anusavice applied the procedures reported by Lee et al. [33], which was modified by Narayanaswamy [28], to determine the transient stresses in a biaxial viscoelastic slab by numerical techniques. A summary of the procedures used in the study by DeHoff and Anusavice [66] is given in Appendix A. For the complete description of the mathematical formulations and the numerical technique, one should refer to the published paper.

Stress Analysis by Finite Element Method

Transient and residual tensile stresses produced within a thermally tempered ceramic can also be calculated by the use of finite element analysis. Some general purpose finite element programs can incorporate the theory of viscoelasticity to determine residual stresses in ceramic structures with complex geometric shapes. However, the finite element analyses performed in this study are based on elasticity theory and are used only for calculation of transient stresses. Although the elastic analysis by finite element method assumes that the viscoelastic stresses

are relaxed during cooling through the glass transition region, the advantage of this method over the viscoelastic analysis by analytical method is that it can be used for a single layered structure as well as multilayered structures with any geometric shape. To determine the transient thermal stresses by the finite element method, first the unsteady–state temperature distributions are calculated based on an energy balance within the model. Then the calculated temperatures are incorporated in the stress-strain relations corresponding to static analysis. A summary of the finite element technique for temperature and stress analyses is given in Appendix B.

Objectives of the Present Study

The present study was designed to optimize the tempering process for layered porcelain structures as a function of the thermal characteristics of the ceramics and cooling media without causing transient failure or inducing high internal residual tensile stresses. The specific objectives of the study were as follows:

1. To test the hypothesis that the strength of feldspathic porcelain structures can be enhanced by thermal tempering.
2. To characterize the transient temperature and stress distribution within bilayered porcelain disks subjected to various cooling treatments.
3. To test the hypothesis that thermal tempering of dental porcelain in gaseous cooling media is more effective than tempering in liquids.
4. To analyze the influence of variables such as cooling method, initial tempering temperature, thermal contraction mismatch, and specimen dimensions on the transient and residual stresses produced within ceramics during various cooling treatments.

CHAPTER II

EXPERIMENTAL METHOD AND ANALYSES

Determination of Thermal Data

Measurement of Thermal Expansion Coefficients

Five specimens in each group of two opaque feldspathic porcelains and two body feldspathic porcelains were prepared as rectangular bars (5x5x50.8 mm) according to the manufacturer's recommendations (J.F. Jelenko and Co., Armonk, NY) and were used to measure the thermal contraction coefficient (α) in the temperature range of 25-500°C. The measurements were conducted according to the ASTM standard designation E228–71 using an Orton single push-rod dilatometer (Orton Ceramic Foundation, Columbus, OH). The percent contraction versus temperature curves for each specimen were obtained by interfacing the dilatometer to a recorder. The displacement of the specimen because of temperature change was transferred through a fused silica pushrod to a linear variable differential transducer (LVDT). The LVDT produced a voltage that was directly proportional to the displacement of the specimen under isothermal conditions. A thermocouple, which was in contact with the surface of the sample, also produced a voltage proportional to the specimen temperature. The voltages produced by the thermocouple and the LVDT were amplified and were transferred to the x and y axes of the chart recorder, respectively (Fig. 2.1). The α values in the temperature range between 25-500°C were determined from the contraction curves of the specimens at a cooling rate of 3°C/min. Shown in

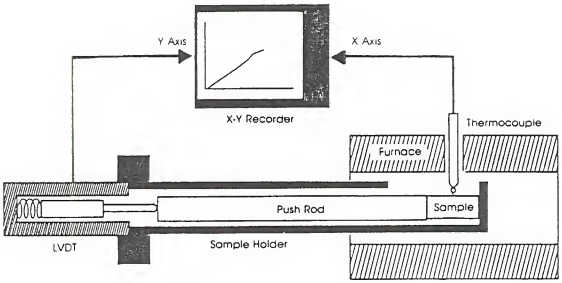

Fig. 2.1 Schematic diagram of a single push-rod dilatometer.

Fig. 2.2 is the percent contraction versus temperature for two opaque porcelains (O1 and O2) and two body porcelain (B1 and B) using a reference temperature of 25°C. The mean values of the linear thermal contraction coefficients corresponding to five specimens in each group for the opaque porcelains were α_{O1} = 12.0 ppm/°C and α_{O1} = 14.2 ppm/°C. The corresponding values for the body porcelain were α_{B1} = 11.0 ppm/°C and α_{B1} = 13.5 ppm/°C. These porcelains were employed to prepare bilayered circular disk specimens with thermal contraction mismatches, $\Delta\alpha$ (α_O–α_B), of +3.2 and –1.5 ppm/°C. Disk specimens consisting of body porcelain only (α_{B2} = 13.5 ppm/°C) were used as a thermally compatible system ($\Delta\alpha$ = 0.0) in the control group to determine the influence of thermal contraction incompatibility on transient and residual stresses produced by various cooling methods. These porcelain combinations correspond to the largest values of positive and negative mismatch types studied by Anusavice et al. [65].

Preparation of Bilayered Disk Specimens

One set of bilayered porcelain disks were 16 mm in diameter and 2 mm in thickness. Each disk consisted of a 0.5 mm-thick layer of opaque and a 1.5 mm-thick layer of body porcelain. The second set of disks were 32 mm in diameter and 6 mm in thickness. Each disk consisted of 1.5 mm thick–layer of opaque porcelain and 4.5 mm–thick layer of body porcelain. In both disk sizes the thickness ratios of body to opaque porcelain were 3 to 1 which is a typical value for clinical restorations. The opaque and body porcelains were condensed into slightly oversized cylindrical brass molds to compensate for sintering shrinkage. After condensing the specimen with a Vibra II handpiece (J.F. Jelenko and Co., Armonk, NY) and removing the excess moisture with a blotting paper, the

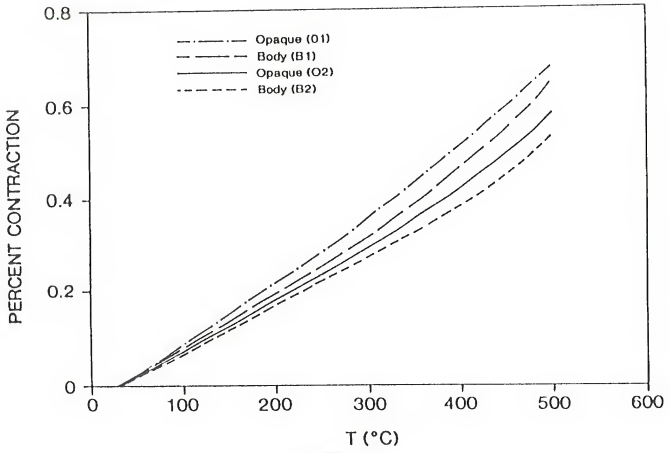

Fig. 2.2 Thermal contraction versus temperature profiles of opaque and body porcelains using a reference temperature of 25°C.

specimens were placed near the open door of a preheated Ney Mark IV digital furnace (J. M. Ney Company, Bloomfield, CT) for 10 minutes, then moved further inside the furnace at an initial temperature of 649°C (1200°F) with the furnace door closed. The furnace temperature was then raised to 982°C (1800°F), which is the maturing temperature of the porcelain, at a heating rate of 20 to 55°C/min. The lower heating rate was applied to minimize the temperature gradient within the 6–mm–thick disks to uniformly fuse the porcelain specimens and to prevent thermal shock failure. Firing was accomplished in a vacuum of 27 in Hg to minimize surface roughness and porosity within the specimen. After the disks were heated at the maximum temperature of 982°C for 15 sec, they were taken out of the furnace and cooled under natural (free) convection to room temperature (30°C). Using a Buehler polishing wheel (Buehler Ltd., Lake Bluff, IL), each porcelain layer was ground to the proper dimensions and finished with 0.05 μm alumina abrasive.

Temperature Distribution within the Dental Furnace

To determine the steady–state temperature distribution inside the furnace, four chromel-alumel thermocouples (K type) were calibrated with a L & N reference standard thermocouple (Leeds & Northrup Company, North Wales, PA) which were installed at various locations inside the furnace. The thermocouples were interfaced to an IBM PC-AT microcomputer (IBM Corporation, Boca Raton, FL) through a μMEGA-4000 analog-to-digital converter (Omega Engineering, Inc., Stamford, CT) which was plugged into the RS–232 serial port of the microcomputer. The furnace temperature was set at constant temperatures between 100 to 982°C and the steady–state temperature distribution within the dental furnace for each set-point temperature was

measured to identify the regions with uniform temperature. Shown in Fig. 2.3 are the locations of thermocouples and the steady–state temperature distribution inside the heating chamber of the test furnace at a control temperature of 982°C. The temperatures at the right side of the heating chamber correspond to the mean values of the four thermocouple readings at each position. The shaded area which is identified as "hot zone", corresponds to the region inside the furnace with minimum thermal gradients. The disk specimens were placed in this region for firing.

Measurement of Cooling Profiles

A computer program in BASIC language was developed to record the temperature values of up to four thermocouples versus any arbitrary time interval which was controlled by using the IBM PC-AT internal clock. This program used the commands recognized by the data acquisition unit to receive temperature data from the thermocouples and the corresponding time values from the computer clock. These data were stored on the microcomputer hard disk for plotting and further analysis of the cooling profiles.

To determine the temperature versus time profiles for each cooling technique, a calibrated thermocouple was installed at the center of each disk on the body porcelain surface with a high temperature resistance cement (Omega Engineering, Inc., Stamford, CT) and the thermocouple was interfaced to the microcomputer. The distance between the center of the thermocouple tip and the disk surface was 0.5 mm. Each disk was supported by a layer of refractory insulating cloth (Thermoz, American Dental Supply, Easton, PA) on a ceramic saggar tray and was placed inside the furnace at the "hot zone" region.

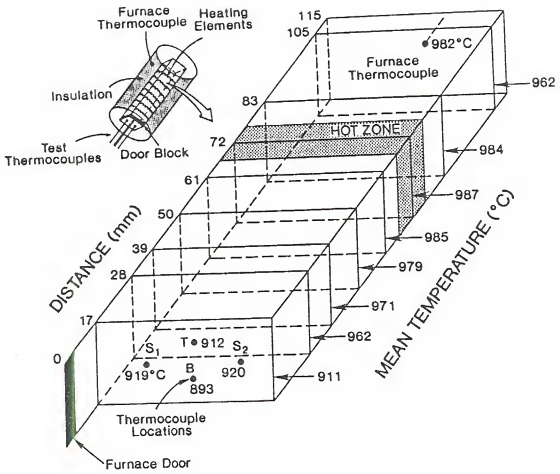

Fig. 2.3 Steady-state temperature distribution in the test furnace at a control temperature of 982°C.

Tempering by Gaseous Cooling Media

To determine the effectiveness of gaseous cooling media and cooling methods, air, nitrogen, and helium were employed and the specimens were cooled by free convection (FC), tempering by vertical flow (TV) and tempering by horizontal flow (TH) from an initial temperature of 982°C. Free convection in air was accomplished by bench cooling of specimens inside the test laboratory. The ambient temperature near the furnace was 30°C. Free convective cooling in other gases was performed inside a relatively large environmental chamber which was completely sealed from the outside air. The temperature inside the environmental chamber during each test was monitored by two digital thermocouples. Shown in Fig. 2.4 is a schematic diagram of the tempering procedure with relative positions of the multiple–orifice nozzle and the thermocouple for air blasting in a vertical direction. In each tempering treatment the gas pressure was set to a constant value of 0.34 MPa (50 psi). The mean value of air velocity near the specimen during tempering was 77 m/sec as measured by a hot wire–anemometer (Solomat Corp., Stamford, CT).

Shown in Fig. 2.5 is a schematic illustration of the modes of heat loss from the surface during the tempering procedure using horizontal air flow. The main sources of heat transfer during cooling treatment with gas are radiation (Q_R) and convection (Q_C). However, heat is also conducted away from the thermocouple junction through the lead wires. This heat loss can cause deviation of the thermocouple output from the actual temperature at the point of interest [70]. To minimize this error, the lead wires near the thermocouple junction were formed into a coil (Fig. 2.5). This configuration minimized the temperature gradient between the thermocouple sensor and the lead wire and, thus, the conduction loss

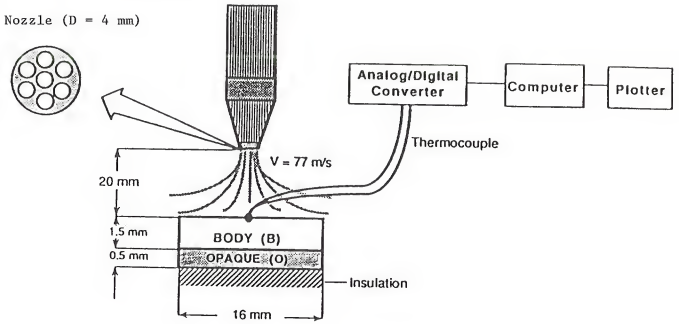

Fig. 2.4 Schematic illustration of vertical air flow conditions for the small disk specimen.

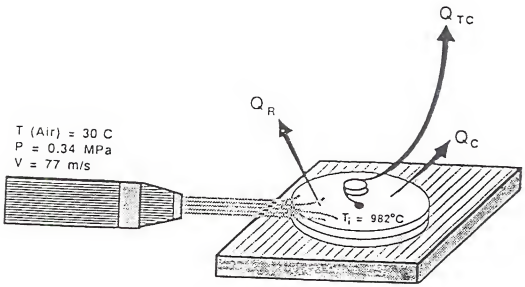

Fig. 2.5 Schematic illustration of horizontal air flow conditions and modes of heat loss.

from the wire to the surroundings. For cooling treatment, by gaseous media, the bottom surface of each disk was placed on a layer of insulating material. Although there was a small heat loss by conduction from the bottom surface to the insulation, for the determination of temperature and stress distribution by analytical methods, the bottom surface was assumed to be perfectly insulated.

Tempering by Liquids

To analyze the effectiveness of tempering in liquid media, the disks were quenched in silicone oils (General Electric Company, Waterford, NY) having kinematic viscosities of 50, 1000, and 5000 centistokes. These oils had the same specific heat (1,506 J/kg·K), conductivity (0.158 W/m·K), and density (957 kg/m^3), at the temperature range between 27°C and 93°C. The silicone oils with variable viscosities were chosen based on the findings of Kirchner [38,47] who quenched alumina in silicone oils at room temperature with fluid viscosities varying from 5 to 12,500 centistokes. He reported that the oils with lower viscosities were more effective than those of higher viscosities because of their higher heat transfer coefficient which produced greater compressive stresses at the surface. However, quenching media with very large heat transfer coefficients, such as water will often promote thermal shock failure. Since quenching the bilayered porcelain disks from the maturing temperature of 982°C in room temperature silicone oils caused thermal shock failure, the initial temperature of the oil was increased to 100°C and the quenching experiments were conducted from specimens at initial temperatures of 850°C or lower.

Influence of Initial Tempering Temperature

Travitzkey et al. [48] showed that initial tempering temperature had a significant influence on the flexural strength of alumina (Fig. 1.4) when tempered by an air jet. In the present study, the porcelain disks were slow-cooled (SC), fast-cooled (FC) and tempered (T) in air or in silicone oil from initial temperatures of 650, 750, 850 and 982°C. The initial temperature of air was 30°C and the corresponding value for silicone oil was 100°C. The effect of initial temperature on specimen strength using silicone oil quenching was analyzed via measurements of surface cracks induced by a microhardness indenter and measurements of the strength by means of a biaxial flexure test. Comparison of the data was performed statistically by means of an analysis of variance (ANOVA) and the Tukey's multiple range test (HSD).

Measurement of Heat Transfer Coefficients

The heat loss by convection from the disk to the surrounding for each cooling treatment is calculated from:

$$Q_C = A\, h_C (T_S - T_a) \qquad (3)$$

where

Q_C = Convective heat loss (W)
A = Convective surface area (m^2)
h_C = Convective heat transfer coefficient ($W/m^2.K$)
T_S = Surface temperature (°C)
T_a = Ambient temperature (°C)

Equation (3) has been simplified by incorporating all of the complex convection characteristics in the coefficient h_C, which is generally a function of

fluid flow, thermal properties of the fluid medium, and geometry of the system [71]. A common method to determine h_C is to combine dimensional analysis with experimental data. It is important to emphasize that the heat transfer coefficient is influenced by the shape and the dimensions of the body under convection and not by its material properties. According to the principle of similarity (model law), the behavior of two systems will be similar if the ratios of their linear dimensions are the same. Therefore, for the experimental determination of the heat transfer coefficient, this principle was applied and a copper disk with the same diameter as the porcelain disk was used. This simplified both the experiments and the calculations, because the same copper disk was used to measure experimentally the cooling profiles for various cooling conditions. Also, because of the large thermal conductivity of copper and the small thickness of the disk, the temperature gradient within the copper was assumed to be negligible and the heat transfer coefficient was determined by a lumped analysis according to the following method:

Rate of energy loss by copper disk = $\dot{Q} = \rho\, V\, C_P \frac{d\, T_S}{dt}$ (4)

where ρ , V and C_P are the density, volume and specific heat of the copper disk, respectively. At any instant of time, the rate of energy loss by the copper disk is the same as the convection loss from the disk to the surrounding fluid:

$$\rho\, V\, C_P \frac{d\, T_S}{dt} = A\, h_C\, (T_S - T_a) \tag{5}$$

Using the initial condition $T(0) = T_i$, one obtains :

$$h_C = \frac{-\rho\, C_P\, L_C}{t}\, \ln\, \left(\frac{T_S - T_a}{T_i - T_a} \right) \tag{6}$$

where $L_C = V/A$ = characteristic length of the disk, t = time and A =convective surface area. To eliminate T_i , two locations (T_1 , t_1) and (T_2 , t_2) on the experimentally determined cooling curve were used [72]. Then from (6) one obtains :

$$h_C = \frac{-\rho C_P L_C}{t_1} \ln \left(\frac{T_1 - T_a}{T_i - T_a} \right) = \frac{-\rho C_P L_C}{t_2} \ln \left(\frac{T_2 - T_a}{T_i - T_a} \right) \quad (7)$$

By eliminating T_i, it can be reduced to :

$$h_C = \frac{-\rho C_P L_C}{t_2 - t_1} \ln \left(\frac{T_1 - T_a}{T_2 - T_a} \right) \quad (8)$$

The condition for a valid lumped analysis [73] is that $B_i = \frac{L_C h_C}{K} < 0.1$

where K is the thermal conductivity of the copper disk and B_i is the Biot number . For an unsteady problem, first B_i is evaluated.

Equations (6) and (8) are commonly used transient methods for determining the heat transfer coefficient by experimentally measuring the slope of the cooling profile. However, this method is associated with an error due to differentiation of the cooling profile [72]. In this study, the heat transfer coefficient was also calculated from other analytical and numerical approaches and the values were checked by comparing the calculated and experimentally measured cooling profiles.

Analysis of Induced Cracks by Microhardness Indentation Test

The microhardness indentation method which is a simple technique for rapid evaluation of fracture toughness was used first by Evans and Charles in 1976

[74]. They concluded that the Vickers indentation technique should enable the calculation of fracture toughness data within an accuracy of approximately 10 percent if the Young's modulus of the material is known. The fracture toughness value provides a measure of resistance to crack initiation and extension in brittle materials. The fracture toughness, K_C, was calculated from the following relations [75-77]:

$$K_C = \chi P / (C_{SC})^{3/2} \quad (9)$$

$$\chi = 1.6 \times 10^{-8} (E/H)^{1/2} \quad (10)$$

Where:

K_C = fracture toughness ($MPa \cdot m^{1/2}$)
χ = dimensionless indenter constant
P = indentation load = 4.9 N
C_{SC} = crack size for slowly cooled disks (m)
E = elastic modulus of porcelain = 70.3 GPa
H = hardness of porcelain (GPa) = $0.47\ P/a_p^2$
a_p = Projected length of the indenter half-diagonal indentation
($a_p = 21 \times 10^{-6}$ m for a load of 4.9 N)

For determination of K_C, the surface of the porcelain disk should contain no significant residual stresses prior to indentation. Therefore, in equation (9), the crack size measured for the slowly cooled specimens was used. In this equation, the ratio $P/(C_{SC})^{3/2}$ was approximately independent of the applied load. Although porosity is known to reduce the elastic modulus of porcelain, no correction was made because data on the variation of E with porosity are not available [78].

Traditionally, residual stresses produced at the surface of a thermally treated glass have been determined by the use of the photoelastic birefringence technique. However, this optical method cannot be used in ceramics because of their opacity. One of the most convenient methods of stress determination is the

measurement of the surface cracks induced by a microhardness indenter [79-82]. Comparative evaluation of crack size on surfaces of tempered and untempered disks will provide information on the residual compressive stresses which are produced because of the tempering treatment.

The specimen surfaces were cleaned, polished, and then positioned under the diamond pyramid indenter on an adjustable mechanical stage corresponding to a Vickers microhardness indenter (Tukon Wilson, Binghampton, NY). An indentation load of 4.9 N (500 grams) was applied through the mechanical control of a dash pot, which eliminates shock and impact and vibration. The dash pot causes a delay on the movement of the indenter and load assembly to allow absorption of machine disturbances before the indenter meets the specimen surface. After a short contact between the indenter and the specimen, the dash pot automatically raises the indenter above the specimen. By using the mechanical stage, the specimens were placed under the microscope to measure the size of the induced indentation crack by a micrometer. The crack sizes were measured within 60 seconds after indentation to minimize error due to crack growth in the presence of environmental moisture. Twenty indentations were applied on the surface of body porcelain in each disk along two perpendicular diametral lines. Each line contained 10 indentations at the surface of body porcelain (Fig. 2.6). The crack sizes which were measured for each of the three silicone fluids, three mismatch levels, and three initial cooling temperatures were compared with the corresponding crack measurements for the slow-cooled (SC), fast-cooled (FC) and tempered (T) specimens in air from an initial temperature of 982°C [Anusavice et al., 65]. Analysis of variance (ANOVA) was performed to determine if the crack sizes were significantly influenced by cooling media, contraction mismatch and initial temperature. If the influence of each variable or

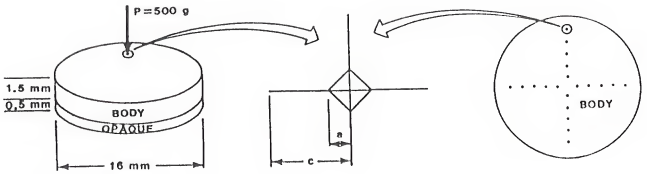

Fig. 2.6 Locations and directions of specimen and indentations applied at the surface of the body porcelain.

their combined effects was significant, a Tukey's multiple contrast analysis (HSD) was employed at a significant level of 5% to determine if the mean values were significantly different. The mean values of crack sizes for tempered (T), fast-cooled (FC) and oil quenched (OQ) specimen were used to calculate the residual surface stresses from the following equation which was developed by Marshall and Lawn [81]:

$$\sigma = \frac{K_C}{2} \left(\frac{\pi}{C}\right)^{1/2} \left[1-\left(\frac{C_{SC}}{C}\right)^{3/2}\right] \qquad (11)$$

,where C_{SC} is the crack size for slowly cooled, C is the crack size for the fast-cooled or tempered specimens, and K_C is the fracture toughness calculated from equation (9).

Biaxial Flexure Test

Background

The biaxial flexure test was developed by Wachtman et al. in 1972 [83] for determining the strength of thin, circular disks of brittle materials. In this method the specimen is supported on three equally spaced balls and a load is applied to the center of the specimen by a flat piston. Unlike the three-point or four-point bending (uniaxial tests), the strength value calculated by this method is unaffected by the edge condition of the specimen. In the biaxial test, the three points of the supports are located near the periphery and equidistant from the center of the disk. Therefore, the area of the maximum tensile stress falls at the center of the lower face of the disk and the strength should be independent of the edge conditions. The breaking load, the dimensions and elastic constants of the specimen, and the radii of the support and the load are used to compute the

maximum tensile stress. Wachtman et al. [83] employed this method to determine the strength of eight types of alumina substrate and they concluded that if the mean biaxial flexure value of five specimens is used as a measure of strength, a coefficient of variation of about 7 percent can be expected for similar materials. This is acceptable for most design considerations.

Flexural Testing of Porcelain Disks

Based on the results from the indentation test for the five mismatch group reported by Anusavice et al. [65], disk specimens with thermal contraction differences of +3.2, 0.0 and –1.5 ppm/°C were selected. Six disks, 16 mm in diameter and 2 mm in thickness were prepared for each mismatch group and each cooling condition. Also, to determine the influence of initial temperature on flexural strength, the compatible disks ($\Delta\alpha = 0.0$) were treated by slow cooling (SC), fast cooling (FC) and tempering (T) methods, each from initial temperatures of 650, 750, and 850°C. Six specimens were prepared for each group and each disk was subjected to biaxial flexure testing under water at 37°C. Shown in Fig. 2.7 is the schematic drawing of the biaxial test apparatus. Each disk was placed upon three equidistant stainless steel balls (1.6 mm in diameter) which lie upon the perimeter of a circle 10 mm in diameter. The disks were loaded in water at 37°C at the untempered surface by means of a steel piston (with a 3.2-mm diameter flat ground along the contacting surface) at a loading rate of 0.5 mm/min until fracture occurred. Since it is expected that this loading condition causes tensile failure at the surface opposite to the applied load, the tempered surface of each disk was placed at the bottom and a compressive force was applied to the center of the top surface. This mode of flexure caused tensile failure to initiate at the center of the lower surface.

Fig. 2.7 Biaxial flexure test apparatus.

The failure stress, σ_F, at the center of the tempered surface was calculated using the following equations developed by Marshall [84] for the piston-on-three-ball flexure test described by Wachtman et al. [83]:

$$\sigma_F = X P_f / a^2 \quad (12)$$

$$X = (3/4\pi) [2(1+\nu) \text{Ln} (R_s / R_o^*) + (1-\nu) (2R_s^2 - R_o^{*2}) / 2R^2 + (1+\nu) \quad (13)$$

$$R_o^* = (1.6 R_o^2 + a^2)^{1/2} - 0.675 a \quad (14)$$

where

σ_F = flexural strength
P_f = applied load at failure
ν = Poisson's ratio (0.28 for dental ceramics)
R_s = radius of the support circle
R_o = radius of the piston at the contacting surface
R = radius of disk
a = thickness of the disk

The failure stress data were analyzed by a two-factor ANOVA and Tukey's multiple range test (HSD) to determine the significance of cooling condition and contraction difference on biaxial flexure strength.

CHAPTER III

ANALYTICAL AND NUMERICAL METHODS

Calculation of Heat Transfer Coefficients

Free Convective Cooling

The convective heat transfer coefficient (h_C) as a function of specimen surface temperature for each cooling method was calculated from the appropriate empirical correlations available for each cooling medium and each flow direction. The results were used in a finite element thermal analysis to determine the temperature distribution within each specimen. Preliminary finite element analyses were performed using h_C as a function of temperature. However, for more simplification, subsequent analyses were performed by assuming an average heat transfer coefficient for each condition. The h_C value for each cooling method was calculated from the following relation :

$$h_C = \frac{Nu\ K_m}{L_c} \tag{15}$$

,where Nu = Nusselt number = ratio of conductive thermal resistance to the convective thermal resistance of the cooling medium

K_m = thermal conductivity of the cooling medium ($W/m^2 \cdot K$)
L_c = characteristic length of the specimen (m) .

For the free convection (FC) case the value of Nu was obtained from the following equations [85]:

$$Nu = 0.54\ Ra^{1/4} \tag{16}$$

$$Ra = \frac{2g\,(T_s - T_a)\,L_c^3}{\gamma\,\kappa\,(T_s + T_a)} \qquad (17)$$

where Ra = Rayleigh number
g = acceleration due to gravity = 9.8 m/s^2
T_s = specimen surface temperature at the center of body porcelain (°C)
T_a = ambient temperature = 30°C
L_c = characteristic length (m)
γ = kinematic viscosity of the cooling medium (m^2/s)
κ = thermal diffusivity of the cooling medium (m^2/s)

Although equation (16) has been developed based on the experimental data for a relatively large plate subjected to convective cooling, several studies have obtained satisfactory results using this equation or a similar equation for disks or plates with relatively small dimensions [86–88]. In the present study, the calculated heat transfer coefficient from equation (16) was used as an initial value in the thermal models to determine the temperature distribution numerically. Then this calculated value was modified to produce calculated cooling profiles comparable with the experimental data. Based on the gradient of the experimentally determined temperature versus time profile, various surface temperatures (T_s) in the range of 30-982°C were used in equation (17). For each constant value of T_s, the thermal properties of the cooling media were evaluated at the following temperature [85]:

$$T_{fm} = \frac{T_s + T_a}{2} + 273.2 \qquad (18)$$

where T_{fm} = film temperature (°K). For each constant value of the specimen surface temperature (T_s), a value of Ra and Nu was calculated from equations (17) and (16), respectively. Using the appropriate values of Nu and L_c in equation (15), the convective heat transfer coefficient as a function of specimen

surface temperature was determined for each specimen dimension and cooling medium.

Characteristic Length

Many discrepancies exist regarding the definition of characteristic length for bodies subjected to natural convection. King [89] has reported the following relation for the characteristic length of a body whose horizontal dimension is L_h and vertical dimension is L_v :

$$\frac{1}{L_c} = \frac{1}{L_h} + \frac{1}{L_v} \tag{19}$$

He indicated that the results of this equation were very satisfactory for bodies such as small short cylinders, planes and spheres. This relation for a porcelain disk, 16 mm in diameter (L_h) and 2 mm in thickness (L_v) gives a characteristic length of 1.78 mm. Equation (19) was quoted for many years in heat transfer textbooks. However, in 1983, Sparrow and Ansari [90] conducted experimental studies on free convective heat transfer for multidimensional bodies. They concluded that King's relation (eq. 19) was inaccurate and its citation in the modern literature [91–94] has been propagated from older textbooks without challenge. Lienhard [95] recommended that the travel length of a fluid in the boundary layer be used as a characteristic dimension. For the porcelain disk cooled by free convection from the top and sides, and insulated from the bottom surface, using L_h =16 mm and L_v = 4 mm, this equation gives a L_c value of 20 mm. Goldstein et al. [96], reported the following commonly used relation :

$$L_c = A/P_s \tag{20}$$

,where A is the surface area and P_s is the perimeter. Equation (20), which was confirmed by Lloyd and Moran [97], is expected to enable horizontal plates as well as nonsymmetrical surfaces to exhibit a common correlation. Using this relation the value of L_c for the disk is 4 mm. However, Kreith [71] has applied a value of 0.9 D (D = disk diameter), for the characteristic length of a horizontal disk which gives an L_c value of 14.4 mm for the porcelain disk. Several authors have used the L_c value to be the same as the disk diameter [86,87,90,96] which was 16 mm for the bilayered disk. In view of these discrepancies, it is unlikely that the selection of a single equation would be sufficient to determine the characteristic length of a multidimensional body. Most of the correlation formulas available for free convection are based on the experimental studies of relatively large bodies. However, the characteristic length of D gave sufficiently accurate results for small disks with variable dimensions in the range of 1 to 20 mm [87]. For the analysis of the convective cooling conditions in the present study. the heat transfer coefficients were calculated using the characteristic length D and the results were in agreement with the published values [73].

Tempering by Vertical Flow

For tempering by vertical flow (TV), the Nusselt number was calculated from [98]:

$$Nu = 0.93\ Re^{0.5}\ Pr^{0.4} \qquad (21)$$

where Re = Reynolds number based on radius = $V R/\nu$
R = Radius of the porcelain disk (m)
Pr = Prandtl number = $\mu C_p/K$
μ = Dynamic viscosity of the cooling media (Pa·s)
C_p = Constant pressure specific heat of the cooling media (kJ/kg·K)
K = Thermal conductivity of the porcelain disk (W/m·K).

As in the FC case, for constant values of surface temperature, the thermal properties of cooling media were evaluated at the film temperature (18) and the corresponding values of Nu calculated from equation (21) were employed in (15) using the specimen's radius as the characteristic length.

Tempering by Horizontal Flow

The convective heat transfer coefficient for tempering by a horizontal flow (TH) was approximated by the equation corresponding to laminar flow over a flat plate [73]:

$$Nu = 0.665\ Re^{1/2}\ Pr^{1/3} \qquad (22)$$

where Re = Reynolds number based on the disk diameter = $V\ D/\nu$

The values of Nu calculated for the constant surface temperature were applied in equation (15), using D as the characteristic length, and the corresponding h_c values were incorporated in equation (3) to determine the transient heat loss due to convection.

Radiative Heat Transfer Coefficient

If the cooling medium is an infrared opaque liquid, all of the heat dissipated from the porcelain disk occurs essentially by convection, but if it is a gas, the exchange of radiant heat between the disk and the surrounding surfaces must be taken into account in computing the total heat loss. It is convenient to include both radiation and convection in expressing the total heat loss from the disk surfaces. This is accomplished by introducing a radiative heat transfer coefficient. For a constant surface temperature corresponding to an instantaneous

time of cooling in free convection (FC) and Tempering (T) cases, a radiative heat transfer coefficient is defined according to the following equation [99]:

$$h_r = \frac{e\,\sigma_{SB}\,(T_s^4 - T_a^4)}{(T_s - T_a)} \qquad (23)$$

where e = emissivity of porcelain = 0.99
σ_{SB} = Stefan-Boltzmann constant = 5.669 x 10^{-8} $W/m^2.K^4$.

The total value of the heat transfer coefficient (h_t) due to combined effects of convection and radiation losses for each cooling condition was obtained from :

$$h_t = h_c + h_r \qquad (24)$$

Closed-Form Solutions

Two-Dimensional Model (2-D)

For the calculation of transient and residual stresses within a disk during each cooling treatment, one needs to determine initially the corresponding transient temperature distributions. Since the disk is subjected to approximately uniform cooling, an axisymmetric thermal model can be used in which the heat is transferred from the disk to the cooling media by convection and radiation. For a further simplification of the analysis, the radiation was taken into account via a modified convective heat transfer coefficient. For gaseous cooling media, the bottom surface of the disk was assumed to be perfectly insulated (Fig. 2.4). But for quenching in liquids, the heat is also transferred from the bottom surface. Under this condition the temperature distribution is symmetric with respect to the midplane of the disk which can be treated as an insulating boundary. Therefore,

The calculated temperature versus time values obtained from the one-dimensional model were incorporated in the viscoelastic model developed by DeHoff and Anusavice [66] to determine the tempering (residual) stresses within each disk. However, for calculation of the transient stresses, an axisymmetric finite element model was developed. Although the viscoelastic model considers the stress relaxation behavior of porcelain, it can be applied only for the single layered disks. Also this model is based on the assumption that temperature gradients along directions parallel to the surface are negligible, while in the axisymmetric finite element model these temperature gradients were taken into account.

The equation governing an axisymmetric temperature distribution T (r,z,t) in the disk shown in Fig. 2.5 is :

$$T_t = \kappa \left(T_{rr} + \frac{1}{r} T_r + T_{zz} \right) \tag{25}$$

which is subjected to the following initial and boundary conditions:

$$T(r,z,0) = T_i \tag{26}$$

$$T_r(0,z,t) = 0$$

$$-K\, T_z(r,a,t) = h\,[T(r,a,t) - T_a]$$

$$-K\, T_r(R,z,t) = h\,[T(R,z,t) - T_a]$$

and

$$T_z(r,0,t) = 0$$

the same solution was applied for gaseous and liquid media, except that in the liquids, only half of the disk thickness was introduced into the equations. Since this is an axisymmetric problem with well defined initial and boundary conditions, a closed-form solution exists.

In this study, first the exact solution of the axisymmetric model was obtained. Then the problem was simplified by the use of a one-dimensional model (Fig. 3.1). The results from these two models were compared with the experimental data for some cooling conditions.

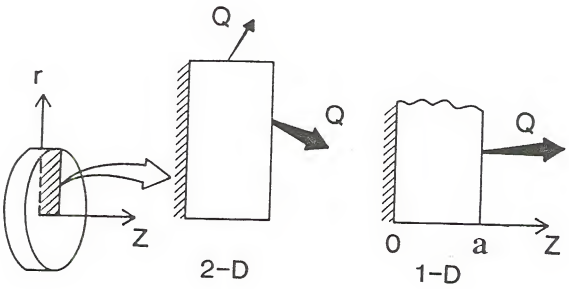

Fig. 3.1 Simplification of the heat transfer analysis from a two-dimensional model to a one-dimensional analytical model.

where κ is thermal diffusivity and K is thermal conductivity of porcelain. An average heat transfer coefficient (h) is assumed for the top and side surfaces. To obtain the non-dimensional form of this equation let:

$$\eta = \frac{r}{R} \quad , \quad \zeta = \frac{z}{a} \quad , \quad \tau = \frac{t\,\kappa}{a\,R} \quad \text{and} \quad \theta = \frac{T - T_a}{T_i - T_a} \tag{27}$$

One then finds:

$$\left(\frac{R}{a}\right)\theta_\tau = \theta_{\eta\eta} + \frac{1}{\eta}\,\theta_\eta + \left(\frac{R}{a}\right)^2 \theta_{\zeta\zeta} \tag{28}$$

with

$$\begin{aligned} &\theta\,(\eta,\zeta,0) = 1 \\ &\theta_\eta\,(0,\zeta,\tau) = 0 \\ &\theta_\eta\,(1,\zeta,\tau) + B_{i1}\,\theta\,(1,\zeta,\tau) = 0 \\ &\theta_\zeta\,(\eta,1,\tau) + B_{i2}\,\theta\,(\eta,1,\tau) = 0 \end{aligned} \tag{29}$$

and

$$\theta_\eta\,(\eta,0,\tau) = 0$$

where

$$Bi_1 = \frac{R\,h}{K} \quad \text{and} \quad Bi_2 = \frac{a\,h}{K} \tag{30}$$

are the Biot numbers based on disk radius and disk thickness, respectively. Using the the method of separation of variables to solve the PDE (28), one obtains:

$$\theta\,(\eta,\zeta,\tau) = \Delta(\eta) \cdot \Psi(\zeta) \cdot \Omega(\tau) \tag{31}$$

Substituting (31) into (28) and applying the symmetric (r = 0) and the insulation (z = 0) boundary conditions yields:

$$\theta(\eta,\zeta,\tau) = \sum_{m=1}^{M}\sum_{n=1}^{N} \{ A_{m,n} \exp[-\frac{a}{R}(\gamma_m^2+\xi_n^2)\tau][J_o(\xi_n\eta)]\cos(\frac{a\gamma_m}{R}\zeta)\} \tag{32}$$

where γ_m and ξ_n are characteristics of the transcendental equations corresponding to the top and right side boundary conditions, respectively. J_o and J_1 are the Bessel functions of the first kind of order zero and order one, respectively (Fig. 3.2). The initial condition and the following equations [100] were used to find a relation for $A_{m,n}$:

$$\int_0^1 [\eta J_o(\xi_n\eta)]\, d\eta = \frac{1}{\xi_n} J_1(\xi_n) \tag{33}$$

$$\int_0^1 [\eta J_o^2(\xi_n\eta)]\, d\eta = \frac{1}{2}[J_o^2(\xi_n) + J_1^2(\xi_n)] \tag{34}$$

Finally one obtains :

$$\theta(\eta,\zeta,\tau) = 4\sum_{m=1}^{M}\sum_{n=1}^{N} \{ \exp[-\frac{a}{R}(\gamma_m^2+\xi_n^2)\tau]\}(C_n)(C_m) \tag{35}$$

with $$C_n = \frac{J_o(\xi_n\eta)}{\xi_n[J_o^2(\xi_n)+J_1^2(\xi_n)]} \tag{36}$$

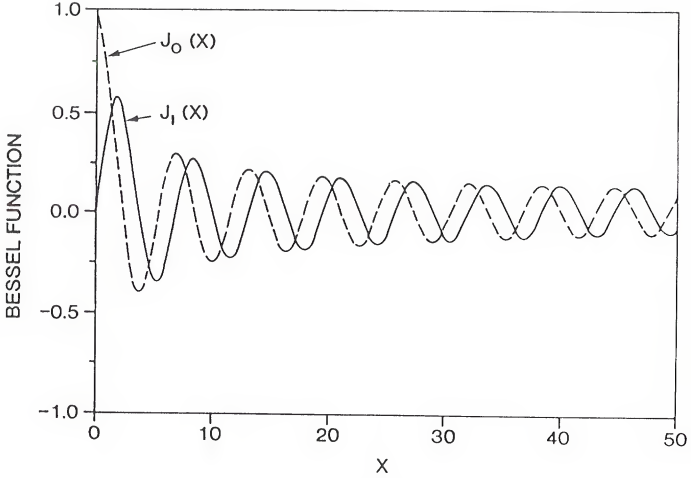

Fig. 3.2 Bessel function of the first kind of order zero and order one.

and $$C_m = \frac{\sin(\frac{a}{R}\gamma_m)(\cos(\frac{a}{R}\gamma_m \zeta))}{[\frac{a}{R}\gamma_m + \sin(\frac{a}{R}\gamma_m)(\cos(\frac{a}{R}\gamma_m))]} \quad (37)$$

where γ_n and ξ_n are characteristics of the following transcendental equations:

$$\cot(\frac{a}{R}\gamma_n) = \frac{a\gamma_n}{R\ Bi_2} \quad (38)$$

$$Bi_1\ J_0(\xi_n) = \xi_n\ J_1(\xi_n)\ . \quad (39)$$

The characteristics of (38) can be easily determined by a numerical or graphical technique. The solution of (39) is obtained by the Newton-Raphson method as follows:

Let:

$$F(\xi_n) = Bi_1\ J_0(\xi_n) - \xi_n\ J_1(\xi_n) \quad (40)$$

then by using the relation :

$$\frac{d}{dx}[J_1(x))] = J_0(x) - \frac{1}{x}J_1(x) \quad (41)$$

one obtains:

$$\frac{d}{d\xi}[F(\xi_n)] = F'(\xi_n) = -[\xi_n\ J_0(\xi_n) + Bi_1\ J_1(\xi_n)] \quad (42)$$

where via Newton–Raphson one obtains:

$$\xi_n(I+1) = \xi_n(I) - \frac{F(\xi_n)}{F'(\xi_n)} \quad (43)$$

For a known value of Bi_1 and an initial guess for ξ_n, initial values for $F(\xi_n)$ and $F'(\xi_n)$ are found by using the Integrated Mathematical and Statistical Libraries (IMSL), subroutine programs. The solution by the Newton – Raphson method (43) is strongly influenced by the initial value ξ_n (I). Therefore, to determine the value of ξ_n, some approximate characteristic values for (39) are first obtained by a graphical methods. Then each approximate value is used as an initial value in (43). Once the solutions of (38) and (39) are obtained, they are used in (36), (37) and (35) to determine the transient temperature distributions at the locations of interest.

A more simplified one-dimensional thermal model can be developed by assuming that the heat transfer from the side of the disk is negligible. It is predicted that for large values of heat transfer coefficient (tempering), the difference between the results from the 1-D and the 2-D models is negligibly small because, under this condition, the heat transfer from the top surface becomes dominant.

Simplified One-dimensional Model (1-D)

In the following solution it is assumed that the transient temperature distribution within the porcelain disk is similar to that of a semi-infinite plate (Fig. 3.1) subjected to convective cooling. Here the governing equation is :

$$T_t = \kappa T_{zz} \tag{44}$$

and is subjected to the initial condition : $T(z,0) = T_i$ (45)

and boundary conditions at left $(z = 0)$: $T_z(0,t) = 0$

at right $(z = a)$: $T_z(a,t) + \frac{h}{K}[T(a,t) - T_a] = 0$

where again h is an average heat transfer coefficient, K is thermal conductivity and κ is thermal diffusivity of porcelain. To convert equation (44) in nondimensional form, let:

$$\eta = \frac{z}{a} \quad , \qquad \tau = \frac{t\kappa}{a^2} \qquad \text{and} \qquad \theta = \frac{T - T_a}{T_i - T_a} \tag{46}$$

to yield :

$$\theta_\tau = \theta_{\eta\eta} \tag{47}$$

with initial condition (I.C.) : $\theta(\eta,0) = 1$ (48)
and boundary conditions (left) : $\theta_\eta\,(0,\tau) = 0$
(right) : $\theta_\eta\,(1,\tau) + \text{Bi}\;\theta(1,\tau) = 0$,

where again, Bi = Biot number = $\frac{a\,h}{K}$

Many heat transfer books have used the method of separation of variables to solve (47) as follows:

$$\text{Let} \qquad \theta\,(\eta,\tau) = \Delta(\eta) \cdot \Omega(\tau) \tag{49}$$

After substituting in (47) and applying the initial and boundary conditions (48) one finds :

$$\theta\,(\eta,\tau) = 2 \sum_{n=1}^{N} \{\exp\,(-\beta_n{}^2\,\tau) \quad \frac{\sin(\beta_n\tau)\,\cos(\beta_n\,\eta)}{\beta_n + [\sin(\beta_n\tau)\,\cos(\beta_n\,\eta)]}\} \tag{50}$$

where β_n are characteristics of the transcendental equation :

$$\tan\,(\beta_n) = \frac{\text{Bi}}{\beta_n} \tag{51}$$

To find the nondimensional temperature, θ, first one must solve (51), using an iteration technique such as the Newton-Raphson method to get the characteristic values of β_n. Then at each point in space (η) and time (τ) , the temperature (θ) is determined from (50). Because of the negative power of the exponential function, this equation usually has a rapid rate of convergence. Therefore, the closed form solution by the separation of variable approach requires the solution of equation (50) and a numerical solution of equation (51).

An alternative approach used in this study is the Laplace transformation method.

The Laplace transformation is defined by:

$$L\ [f(\tau)] = \int_0^\infty [f(\tau)\, e^{-s\tau}]\, d\tau = F(s) \qquad (52)$$

where $$f(\tau) = L^{-1}\,[F(s)] \qquad (53)$$

Taking L of both sides of (47) and applying the initial condition will yield an ordinary differential equation (ODE) :

$$\Theta_{\eta\eta} - s\,\Theta = -1\ , \qquad \text{where } \Theta = L(\theta) \qquad (54)$$

Solving this ODE one has:

$$\Theta\ (\eta, s) = A \sinh(\sqrt{s}\ \eta) + B \cosh(\sqrt{s}\ \eta) + 1/s \qquad (55)$$

subjected to the boundary conditions (left) : $\Theta\ (0, s) = 0$ (56)

(right) : $\Theta_{\eta} + Bi\,\Theta = 0$ at $\eta = 1$

Applying the boundary condition and taking the inverse Laplace transform (L^{-1})

of both sides will yield :

$$\theta(\eta,\tau) = 1 - \text{Bi}\ L^{-1}\left\{\frac{\cosh(\sqrt{s}\,\eta)}{s[\sqrt{s}\sinh(\sqrt{s}) + \text{Bi}\cos(\sqrt{s})]}\right\} \qquad (57)$$

For given values of Bi and η , the L^{-1} term is easily found by using available computer programs such as IMSL subroutines. In equation (57), s is a parameter corresponding to the nondimensional time, τ . The advantage of this method over the previous separation approach is that the temperature (θ) can be obtained by solving only one equation. The higher efficiency of this method becomes more apparent when the temperatures are calculated for various values of the heat transfer coefficient. Also the computer programming of this method is less difficult than for the separation of variable approach.

Finite Element Models

A. Axisymmetric Model of Ceramic Disks for Thermal Stress Analysis

As stated earlier, an axisymmetric finite element model was developed to determine the transient temperature and stress distributions within the bilayered porcelain disks by considering the heat loss from the side of the disk. In this model, it was assumed that the bottom surface (side DC in Fig. 3.3) was completely insulated and the disk specimen was initially at a uniform temperature. The shaded cross section of the disk was divided into 153 nodes and 128 quadrilateral elements and the boundary conditions shown in the figure were applied in the thermal analysis. The node which is labeled 103 and is located near point A on the y axis corresponds to the thermocouple location for each

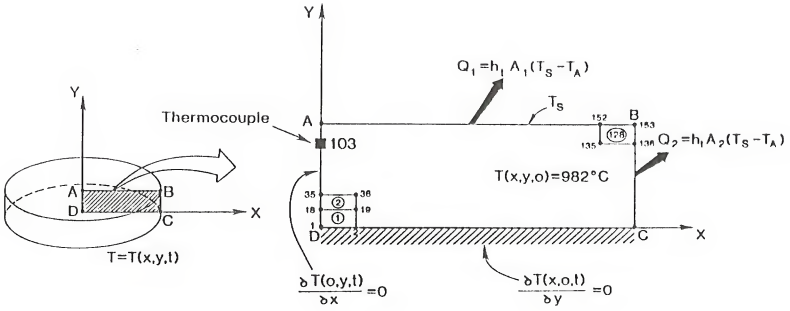

Fig. 3.3 Axisymmetric thermal model and boundary conditions for the finite element analyses.

disk. The total heat transfer coefficient , h_t , calculated from equation (24) was used to impose the boundary conditions along the sides AB and BC.

Shown in Fig. 3.4 are the node and material type numbers and the boundary conditions used in the finite element stress analyses. The nodes located on the symmetric axis correspond to zero displacement along the horizontal axis. A zero displacement along the vertical direction was also imposed on the node 1. For the bilayered disk the thickness ratio of body (1) to opaque porcelain (2) was assumed to be 3 (Fig. 3.4) which represents the clinical conditions. Shown in Fig. 3.5 are the element numbers used in the finite element model. The transient temperature and stress distribution within disks subjected to various cooling conditions were calculated by the use of the finite element program, ANSYS (Swanson Analysis System, Inc., Houston, PA). To improve the accuracy of the nodal temperatures and to minimize the computer time required for the unsteady–state thermal analysis, the automatic time step optimization option of ANSYS was employed. Therefore, at the initial stage of cooling the time step (Δt) had the smallest value of 0.5 sec which increased gradually as the slope of the cooling curve reduced at the later stages. The calculated nodal temperatures as a function of time were stored in a computer file to be recalled as input data for the axisymmetric thermal stress analysis. A glass transition (T_g) value of 600°C was assumed for each porcelain type and the calculated temperatures near this T_g value were used to determine the transient stress distribution. Shown in Table 3.1 are the thermal and mechanical properties of porcelains used in the finite element models.

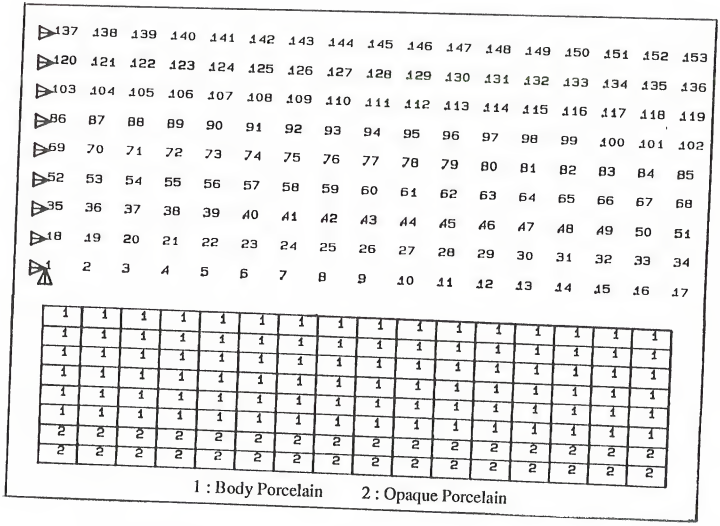

Fig. 3.4 Node and material property numbers used in the finite element model of a bilayered ceramic disk.

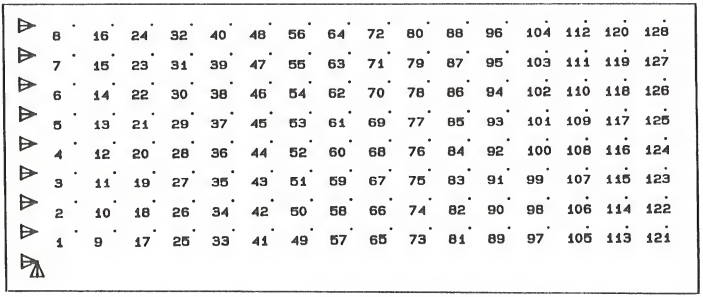

Fig. 3.5 Element numbers and boundary conditions used in the finite element model of a bilayered ceramic disk.

Table 3.1 Thermal and Mechanical Properties of Porcelain used in Finite Element Analysis.

PROPERTY	UNIT	VALUE
Thermal Conductivity	W/m·K	1.68
Density	kg/m^3	2.29×10^3
Specific Heat	J/kg·K	1.68×10^3
Glass Transition	°C	600
Modulus of Elasticity	GPa	70.3
Poisson's Ratio	---	0.28
Thermal Contraction Mismatch	ppm/°C	-1.5, 0.0, +3.2

B. Three-Dimensional Model of Dental Ceramic Crowns for Static Analysis

Stress analyses were performed for ceramic thicknesses of 0.5 mm (case I), 1.5 mm (case II), and 3.0 mm (case III) at the occlusal region (Fig. 3.6). The elastic modulus values used for ceramic, dentin and pulp were 7.03×10^4, 1.86×10^4 and 2.0 MPa, respectively, and the corresponding Poisson's ratios were 0.28, 0.31 and 0.45, respectively. The analyses were performed on an IBM PC-AT microcomputer using the SAP86 (Number Cruncher Microsystems, Inc., San Francisco, CA) finite element program. All the components of normal, shear and principal stresses and displacements along the three directions of the global coordinate system were examined by use of stress contour maps.

Shown in Fig. 3.7 is the three-dimensional finite element model of the molar crown which consisted of 586 nodes and 456 solid elements. All the nodes in the x-y plane which correspond to the root portion of dentin, were assumed to be fixed. A distributed load of 600 Newtons which is an average

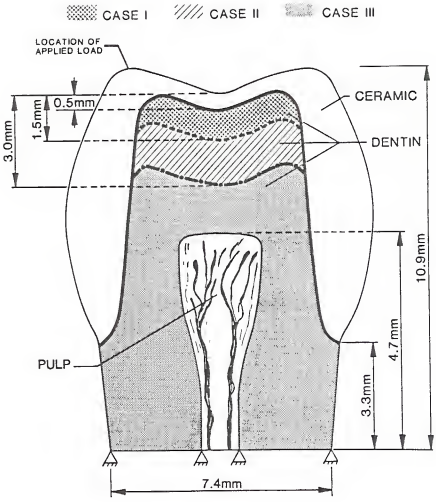

Fig. 3.6 Mesial view of a mandibular second molar showing three design cases.

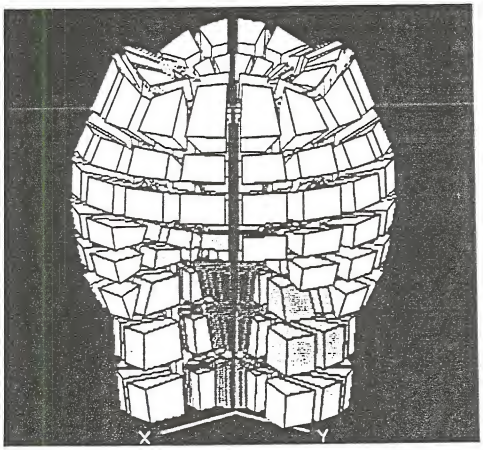

Fig. 3.7 Three-dimensional finite element model of the molar crown.

biting force on a molar tooth, was applied at the occulusal region along vertical (Fig. 3.8) and horizontal directions.

C. Axisymmetric Model of Dental Ceramic Crowns for Thermal Stress Analysis

Shown in Fig. 3.9 is the finite element model of the molar crown used in the stress analysis. Because the crown is axisymmetric with respect to a vertical axis passing through AB, only half of the model (Fig. 3.10) consisting of 164 nodes and 136 elements was used in the analysis. The bilayered ceramic crown consisted of an approximately 1.5 mm thick layer of opaque (α = 14.2 ppm/°C) and a 4.5–mm–thick layer of body porcelain (α = 11.0 ppm/°C). In the thermal analysis, the inside surface was assumed to be completely insulated and the outside surface was subjected to uniform convective cooling. The transient temperature distributions were determined for free convective cooling (h =70 W/m^2.K) and tempering by forced air (h =560 W/m^2.K). The temperatures were calculated for an initial time step (Δt) of 0.5 sec and the time step optimization option of the ANSYS program was used to increase the Δt value. The calculated temperatures were incorporated in the stress analysis program to determine transient stresses for assumed glass transition temperatures, (T_g), of 600°C and also 400°C. The transient stresses were calculated relative to these T_g values for the crowns cooled from the initial temperatures of 850°C and 750°C. The node A located on the symmetric axis (Fig. 3.10) was assumed to be fixed along the x and y directions. Points C and D (Figs 3.9 and 3.10) identify the cuspal region of the crown which has the maximum ceramic thickness. The temperature versus time corresponding to each cooling treatment was plotted at these points using the postprocessing options of the ANSYS finite element program.

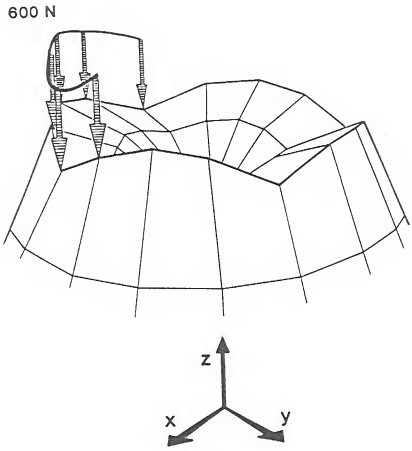

Fig. 3.8 Locations of the applied loads in the finite element model.

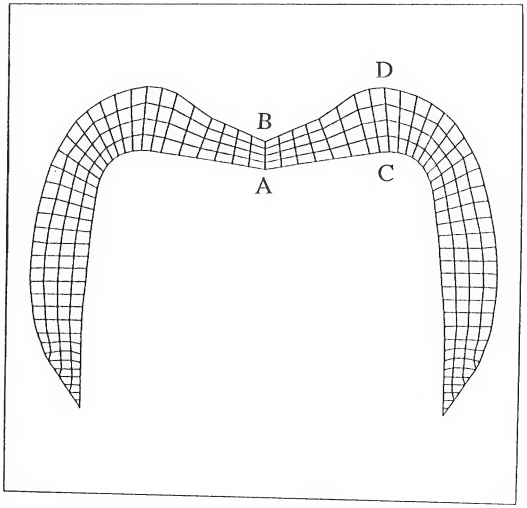

Fig. 3.9 Cross section of a ceramic molar crown used for finite element thermal stress analysis.

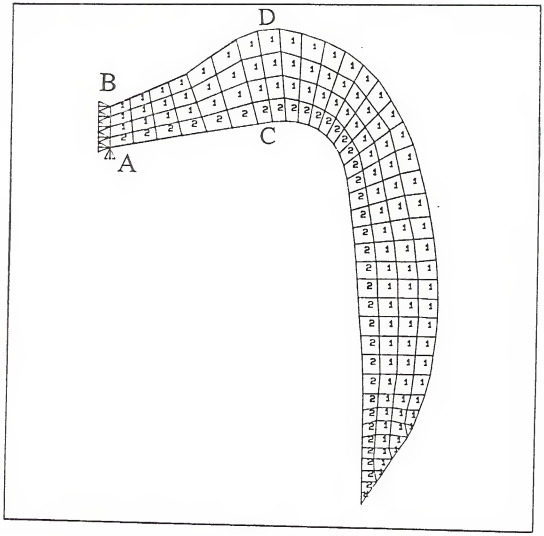

Fig. 3.10 Axisymmetric finite element model of the bilayered ceramic molar crown consisted of opaque and body porcelain layers.

CHAPTER IV

RESULTS

Thermal Analyses

Thermal Contraction Curves

The percent thermal contraction data as a function of temperature for the two opaque and two body porcelain types (Fig. 2.2) were obtained from the cooling curves. Each curve corresponds to the mean values obtained from five specimens in the temperature range between 25°C to 500°C, using a reference temperature of 25°C. The average coefficient of linear thermal contraction (α) for each porcelain group (five specimens in each group) which was calculated from the slope of these cooling curves, agreed well with the values supplied by the manufacturer (J.F. Jelenko and Co., Armonk, NY). Although the transition of dental ceramics from solid to liquid occurs in a temperature range (glass transition region) which depends on the type of porcelain and thermal parameters such as heating and cooling rates used, in this study a constant glass transition temperature (T_g) of 600°C was assumed for the finite element analysis.

Temperature Distribution within the Dental Furnace

A schematic illustration of the furnace heating chamber and the steady–state temperature distribution inside this chamber at 982°C was shown in Fig. 2.3. The mean temperature values of the sides (S_1 and S_2), top (T) and bottom (B) thermocouples at each distance from the furnace door indicate that there is a relatively larger temperature gradient from the center toward the furnace door compared to the back wall which is located at a distance of 115 mm from the door.

Although the furnace thermocouple is controlled at a temperature of 982°C, this thermal gradient exists because of the heat losses from the front and back walls of the chamber and the nonuniform arrangements of the electric heating elements. At each distance there was a larger difference between the top (T) and bottom (B) thermocouples compared to the difference between S_1 and S_2 (see Fig. 2.3). The average temperature values at the side (S) and the overall mean (M) corresponding to the four thermocouples as a function of distance are plotted in Fig. 4.1. The shaded region which is located between the distance of 65 mm and 75 mm is related to the maximum temperature value of each curve and is identified as the hot zone region of the heating chamber. To minimize the initial temperature gradient within the specimen, each disk was placed inside the furnace near this region and 15 sec after the desired set point temperature was reached, it was rapidly removed from the furnace for various cooling treatments.

Experimental Cooling Profiles

Shown in Fig. 4.2 are the measured temperature versus time profiles of a 2–mm–thick disk subjected to free convection (FC), tempering by horizontal flow (TH) and tempering by vertical flow (TV) from an initial temperature of 982°C, using air as a cooling medium. The largest slope of the cooling curve corresponds to the TV case in which the disk temperature at the thermocouple location (0.5 mm from the surface) reached the ambient temperature (30°C) after 50 sec. However, because the bottom surface was still at a higher temperature, the air blasting was continued for approximately 90 sec until the entire specimen reached ambient temperature. The time required for the specimen to reach the ambient temperature was 90 sec for TH and 8.5 minutes for FC conditions. The glass transition temperature (T_g) of 600°C for TV, TH and FC cases were reached after 4.5, 16

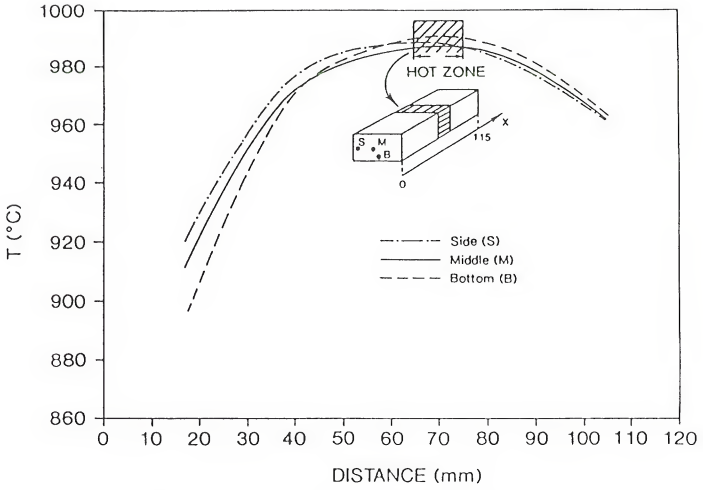

Fig. 4.1 Temperature versus distance from the door of the test furnace at a control temperature of 982°C.

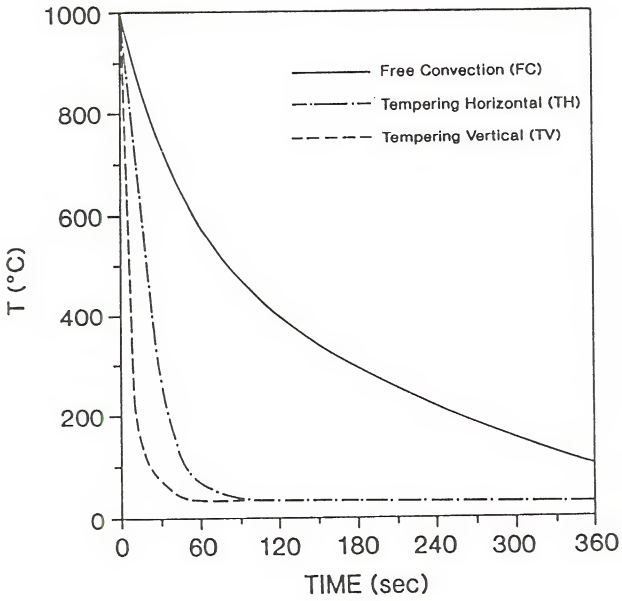

Fig. 4.2 Temperature versus time profiles of a 2-mm-thick disk for free convective cooling, tempering by horizontal and vertical flows.

and 56 sec, respectively. As the experimentally determined cooling curves for the 6 mm-thick disk (Fig. 4.3) also indicate, tempering by vertical air flow produced a more rapid cooling rate than the horizontal flow. For this specimen which has a diameter of 32 mm, the T_g value was reached after 4.5 sec (TV), 34 sec (TH) and 72 sec (FC). A comparison among the cooling profiles of a 2-mm thick disk subjected to slow cooling inside the furnace (SC), fast cooling (FC), and tempering by vertical flow of air (TV) are shown in Fig. 4.4. For the disks that were slow-cooled from an initial temperature of 982°C, the ambient temperature of 30°C was reached after approximately 4 hours.

Shown in Fig. 4.5 is the comparison between the capabilities of air and helium gases for cooling of a 2-mm-thick, 16-mm-diameter , and 6-mm thick, 32-mm-diameter specimens by free convection. In both specimens, the slope of the cooling curves for helium gas were larger than the values for air. As was expected, because of the difference between their heat capacities, the time required for the 6 mm-thick disk to reach ambient temperature was much greater than that for the 2 mm-thick disk. The experimentally measured temperature versus time profiles of a 2 mm-thick disk subjected to free convection (FC) and tempering (TV) in helium and air are shown in Fig. 4.6. For the TV case, there was a negligible difference between the cooling curves obtained from helium and air. Both of the cooling media led to an ambient disk temperature of 30°C after about 30 sec. In the free convection case (FC), the helium gas was more effective than air but the difference between the slopes of the curves near the glass transition temperature (T_g) was relatively small. Because of the similarity between the thermal characteristics of nitrogen and oxygen with air, additional cooling experiments were carried out only for nitrogen gas.

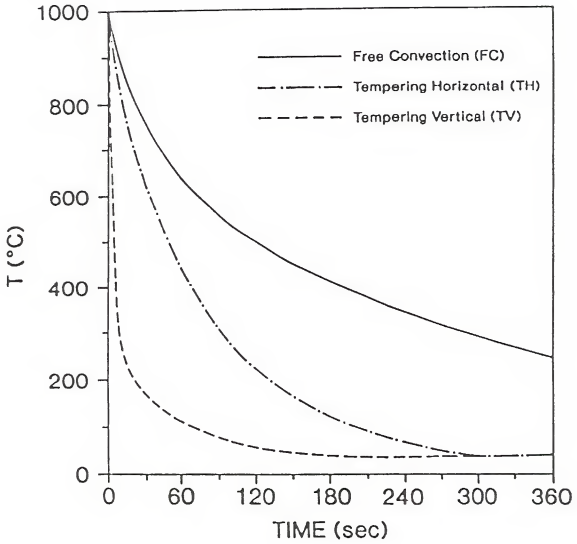

Fig. 4.3 Temperature versus time profiles of a 6-mm-thick disk for three air cooling conditions.

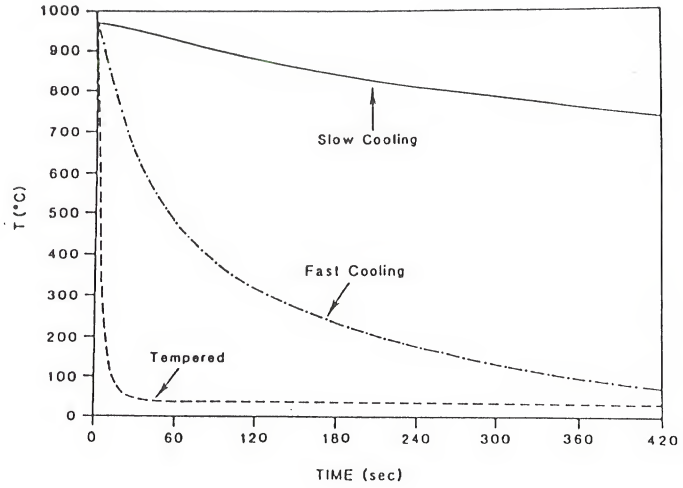

Fig. 4.4 Temperature versus time profiles in a 2-mm-thick disk using slow cooling, free convective cooling and tempering in air.

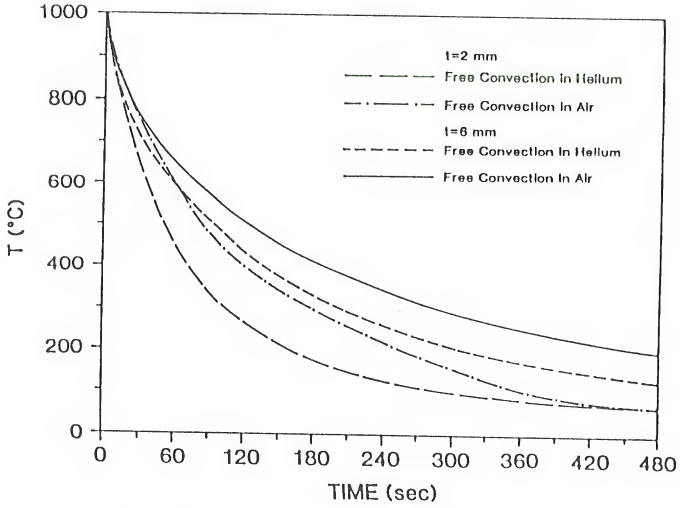

Fig. 4.5 Temperature versus time profile of a 2-mm (t = 2) and a 6-mm (t = 6) thick disk cooled by free convection in air and helium.

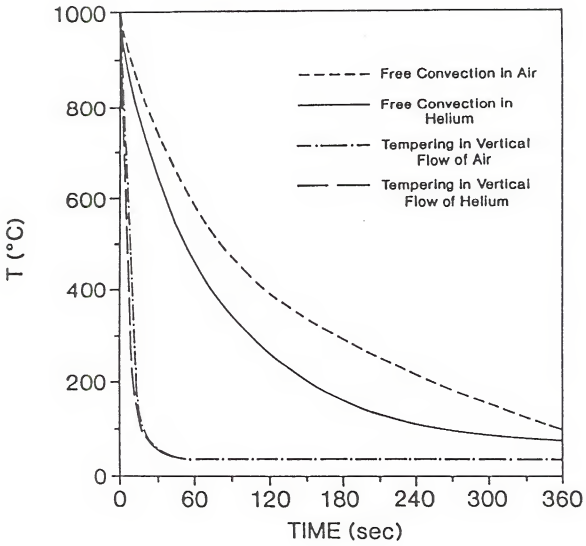

Fig. 4.6 Cooling profiles of a 2-mm-thick disk subjected to free convection and tempering in helium and air.

Shown in Fig. 4.7 are the cooling profiles for 2 mm-thick and 6 mm-thick specimens tempered by vertical (TV) and horizontal (TH) flow of nitrogen. This figure also shows that vertical tempering is more effective than horizontal tempering and the difference is more pronounced for the 6 mm-thick disk which has a larger diameter (32 mm). For the horizontal flow condition, the thickness of the thermal boundary layer increases with the distance from the nozzle, consequently, the heat transfer or the effectiveness of tempering is reduced along this direction.

Heat Transfer in Gaseous and Liquid Cooling Media

The heat transfer coefficient (h) is a function of the cooling medium and the method of cooling. For free convective cooling of a body in air, h is in the range between 5 to 50 $W/m^2 \cdot K$, while for forced convection the value can increase up to 500 $W/m^2 \cdot K$ (Fig. 4.8). When water is used as cooling medium, the value of h can be as high as 4,000 for free convection and 15,000 $W/m^2 \cdot K$ for forced convection. Shown in Fig. 4.9 is the comparison among the equivalent heat transfer coefficients (h) for a 2-mm thick porcelain porcelain disk cooled by free convection (FC), radiation and tempering by vertical air flow (TV). The h values for FC and TV conditions, which were determined from equations (16) and (21), are approximately independent of specimen surface temperature. However, the equivalent heat transfer coefficient for radiation (h_r) which is calculated from equation (23) and exists in both FC and TV cooling cases is significantly influenced by the surface temperature. Therefore, the total heat transfer coefficient (h_t in eq. 24) is a temperature dependent property, during the initial stage of cooling. As shown in Fig. 4.10, the major mode of heat loss at higher

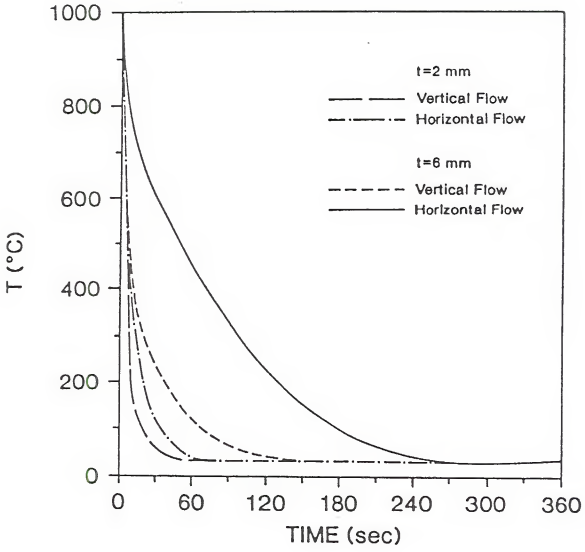

Fig. 4.7 Cooling profiles of 2-mm (t = 2) and 6-mm (t = 6) thick disks tempered by vertical and horizontal flow of nitrogen.

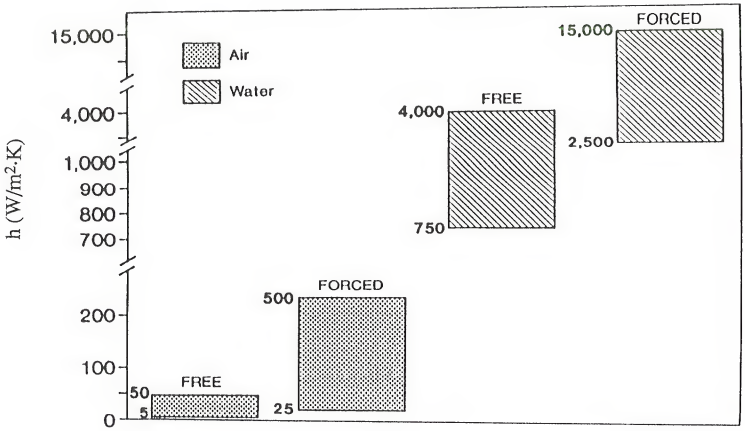

Fig. 4.8 Approximate values of the convective heat transfer coefficients in air and water.

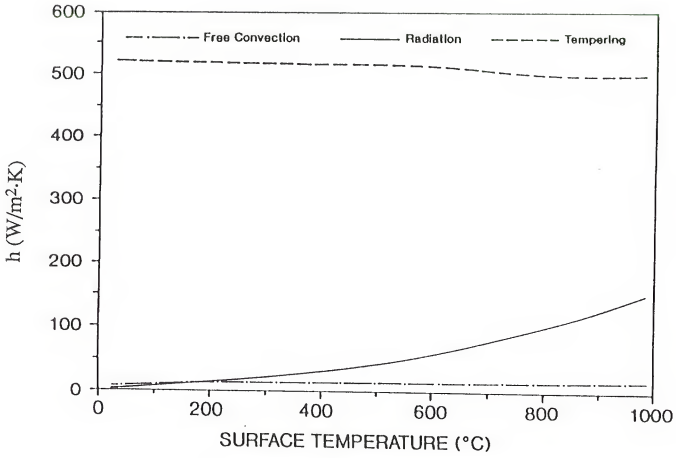

Fig. 4.9 Equivalent heat transfer coefficients versus surface temperature for a 2-mm thick disk subjected to various modes of cooling.

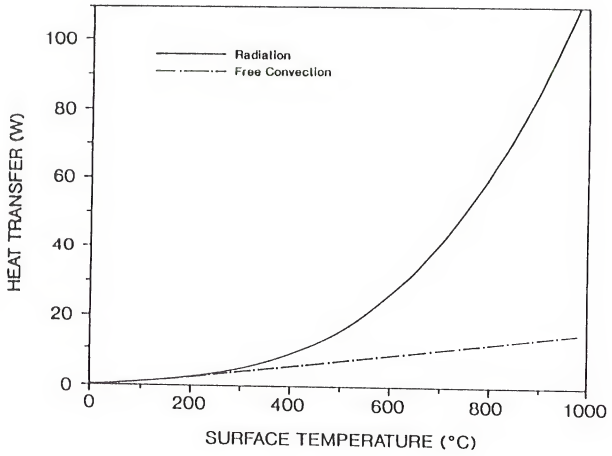

Fig. 4.10 Radiation and convection heat losses from a 2-mm-thick disk.

temperatures, which for the cooling condition in this study is called "free convection" or "fast cooling" (FC), is actually radiative heat transfer. At the initial stage of cooling, the heat loss by radiation is approximately 7 times greater than the convection heat loss. As the specimen temperature drops below 300°C, the amount of heat losses by convection and radiation become comparable. The h_t values in the temperature range between 30 and 982°C which were obtained by superposition of convective and radiative heat transfer coefficients were determined for each cooling condition and used in the thermal models to calculate the transient temperature distributions within each disk.

As stated in Chapter III, the heat transfer coefficient is independent of the material properties of the body. However, the thermal history of the body is controlled by the heat transfer coefficient. Shown in Fig. 4.11 is the calculated temperature versus time profile determined from equation 6 for a thin copper disk for some arbitrarily chosen values of the heat transfer coefficient.

To compare the cooling capabilities of various media and to determine an average h value associated with each cooling medium, a thin copper disk, 1 mm in thickness and 16 mm in diameter, was employed. Experimentally measured cooling profiles for free convection in air, silicone oils with kinematic viscosities of 50 and 1000 centistokes, and water are shown in Fig. 4.12. The largest temperature gradient was obtained in the water quenched specimens in which the ambient temperature was reached after 7 sec. The silicone oil with a kinematic viscosity of 50 centistokes resulted in a steeper cooling profile because it is associated with a larger heat transfer coefficient compared with that of oil at a larger viscosity.

To determine the influence of porcelain and silicone oil soaking temperatures in producing thermal shock failure, several quenching experiments were conducted

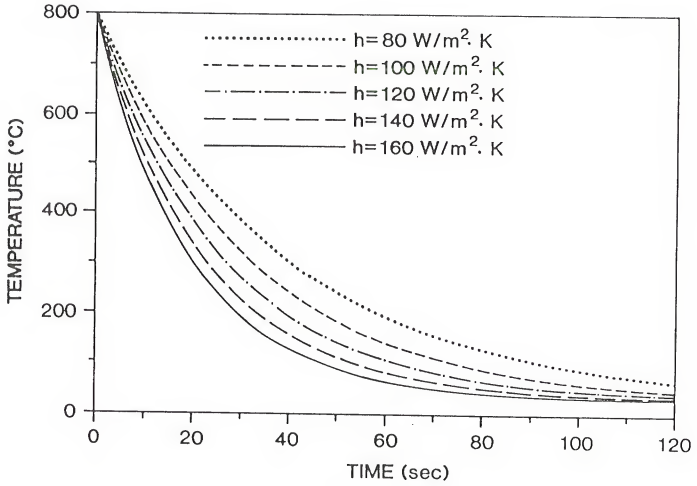

Fig. 4.11 Cooling profile of a thin copper disk for various values of heat transfer coefficient.

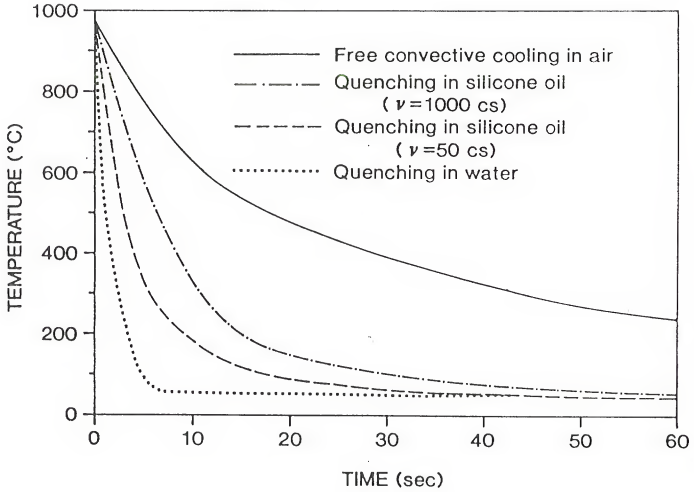

Fig. 4.12 Cooling profiles of a thin copper disk cooled in various cooling media from an initial temperature of 982°C.

by reducing the initial temperature of the disk and/or increasing the initial temperature of the silicone oil. When porcelain disk specimens were quenched from an initial temperature of 982°C in the silicone oils at room temperature, thermal shock failure occurred in almost all bilayered specimens. But when the initial temperature was 850°C and the oil was at 100°C, thermal shock occurred in approximately 5% of the bilayered ($\Delta\alpha$ =+3.2 or $\Delta\alpha$ = –1.5) porcelain disks. In general, the quenching experiments with the single layer disks ($\Delta\alpha$ = 0) were more successful (fewer thermal shock failures) than that of the bilayered ($\Delta\alpha$ = –1.5 or $\Delta\alpha$ = +3.2) disks, probably because the incompatibility tensile stresses were not produced in the first group.

Determination of the Average Heat Transfer Coefficients

DeHoff and Anusavice [66] assumed a constant heat transfer coefficient (h) of 57 W/m^2·K in the solution of a semi-infinite plate (eq. A-1), to determine the transient temperature distribution in a single–layer porcelain plate subjected to free convective cooling from an initial temperature of 800°C. Although the value of h was chosen based on thermocouple measurements reported in a study by Twiggs et al. [101], the calculated cooling profile was not compared with any experimental data. In the present study, the h value of 57 W/m^2·K was used in equations (35) and (57) to determine the temperature versus time profile in a porcelain disk subjected to free convective cooling (FC) from an initial temperature of 982°C. The results from 1-D (57) and 2-D (35) thermal models and the comparison with the experimental data are shown in Fig. 4.13. The heat transfer coefficient of 57 W/m^2·K applied in the 1-D model, overestimates the temperatures. However, when it was applied in the 2-D solution, better agreement between the model and

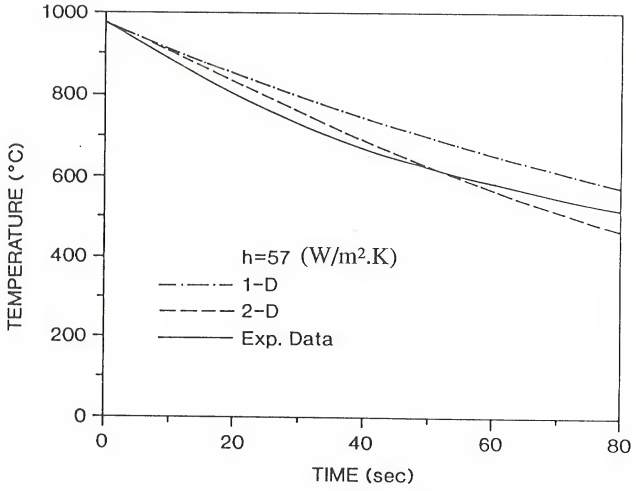

Fig. 4.13 Calculated and measured cooling profiles for free convective cooling of a 2-mm-thick porcelain disk in air using a heat transfer coefficient of 57 W/m^2.K.

the experiment was obtained near the glass transition region. This difference is because of the heat loss from the side of the disk specimen which is not taken into account in the 1-D analysis.

The experimental cooling profile for a copper disk was used to determine the mean value of the heat transfer coefficient for free convective cooling of a porcelain disk. The h values of 60 and 80 $W/m^2 \cdot K$ were used in the lumped analysis (eq. 6) to calculate the transient temperatures and the results were compared with the experimental data (Fig. 4.14). These results indicate that the cooling profile of a copper disk subjected to free convection can be predicted by using a heat transfer coefficient between 60 and 80 $W/m^2 \cdot K$. When an h value of 70 $W/m^2 \cdot K$ was applied in equation (57), the calculated temperature versus time profile agreed well with that of the experimental values. Shown in Fig. 4.15 is the comparison between the 1-D model and the experimental data for a porcelain disk using the non-dimensional forms of time and temperature (eq. 46). To determine the cooling profile from the 2-D analysis with the heat transfer coefficient of 70 $W/m^2 \cdot K$, the characteristic values of (38) and (39) were calculated by the Newton-Raphson method. The approximate values of characteristics corresponding to the transcendental equation (39) were found by graphical methods (see Fig. 4.16) and were applied in equation (43). For the conditions used in this analysis, the first 10 positive characteristics of equations (38) and (39) yielded acceptable accuracy in the temperatures obtained from equation (35).

Shown in Fig. 4.17 is a comparison between the results from the 1-D and 2-D analyses with the experimental data corresponding to a thermocouple which was embedded along the symmetric axis of the porcelain disk at a distance of 0.5 mm from the surface. This figure indicates that a heat transfer coefficient of 70 $W/m^2 \cdot K$ is suitable for predicting the thermal history based on the 1-D analysis.

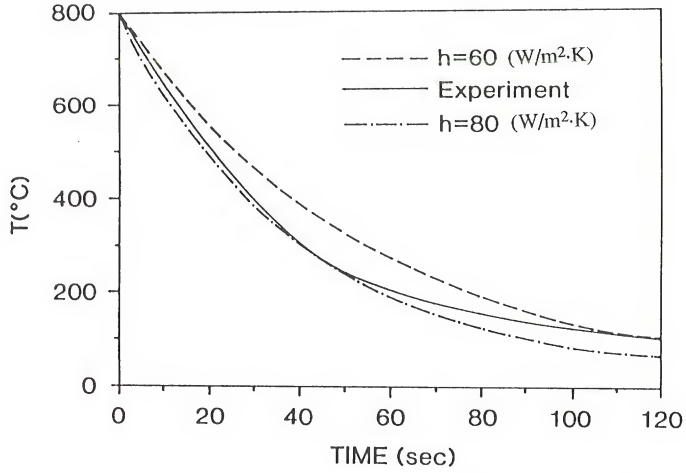

Fig. 4.14 Experimental and the calculated cooling profiles for a thin copper disk subjected to free convection using a heat transfer coefficients of 60 $W/m^2 \cdot K$ and 80 $W/m^2 \cdot K$.

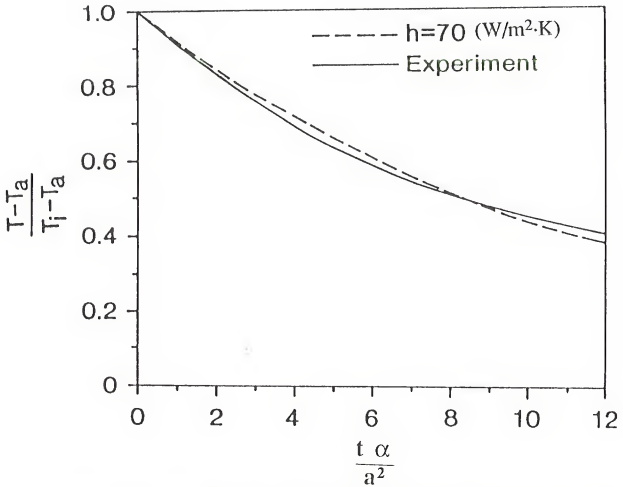

Fig. 4.15 Experimental and calculated (1-D) cooling profile for a 2-mm-thick porcelain disk subjected to free convection using a heat transfer coefficient of 70 W/m^2·K.

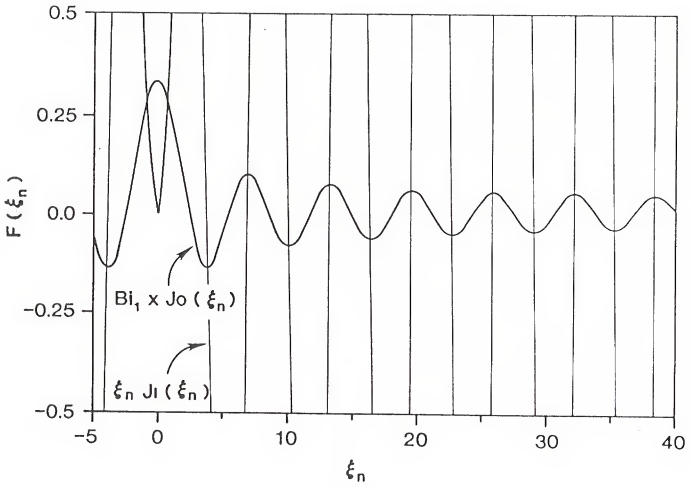

Fig. 4.16 Graphical solution of the transcendental relation (equation 39) for a heat transfer coefficient of 70 W/m^2·K.

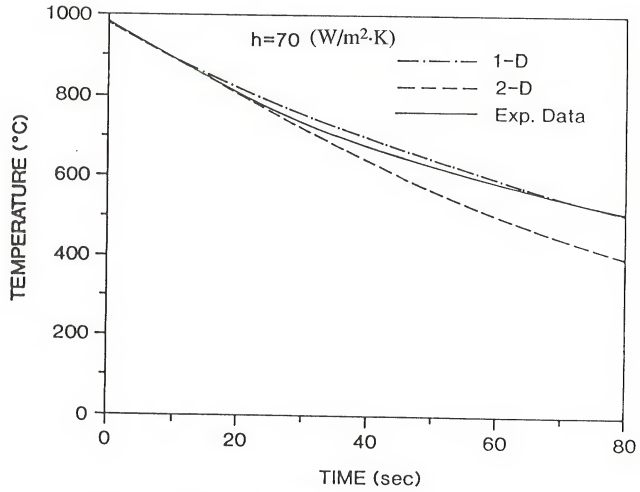

Fig. 4.17 Calculated and measured cooling profiles for the free convective cooling of a 2-mm-thick disk in air using a heat transfer coefficient of 70 W/m2·K in the thermal models.

However, the 2-D model here yields lower temperatures than the measured values. The results in Figs. 4.13 and 4.17 suggest that the cooling profiles of the porcelain disk can be predicted with variable accuracy depending on the type of model (1-D or 2-D) and the value of the heat transfer coefficient used. For free convective cooling the heat loss from the side cannot be neglected compared with the loss from the surface. Thus, the h value of 57 $W/m^2 \cdot K$ used by DeHoff and Anusavice [66] in a 1-D model of a porcelain plate will result in a more accurate cooling curve when it is applied in a 2-D model of a porcelain disk. However, to make the computations less difficult, further analyses were performed based on the results from the 1-D model for a higher heat transfer coefficient value of 70 $W/m^2 \cdot K$ (Fig. 4.17).

Shown in Fig. 4.18 is a comparison between the cooling profiles for a tempered disk by a vertical air flow from the 1-D and the 2-D models. Similar to the previous method, an average value of h was obtained using the slope of the cooling profile from a copper disk. The mean values of the total heat transfer coefficient used in the 1-D thermal model for specimens quenched in air, silicone oil and water were 560, 720 and 1590 $W/m^2 \cdot K$, respectively. As Fig. 4.18 indicates, for a large value of h (560 $W/m^2 \cdot K$ or higher), the results from the 1-D and 2-D models are similar above the glass transition region. This supports our hypothesis that, for such rapid cooling condition, the heat transfer from the top surface of the disk is much greater than that from the side so that side heat loss can be considered negligible. Therefore, the one-dimensional model is sufficient for calculation of the temperature and from that the stress distributions within the tempered disks in air and in silicone oil. The stresses for these conditions were calculated based on the results from equation (57).

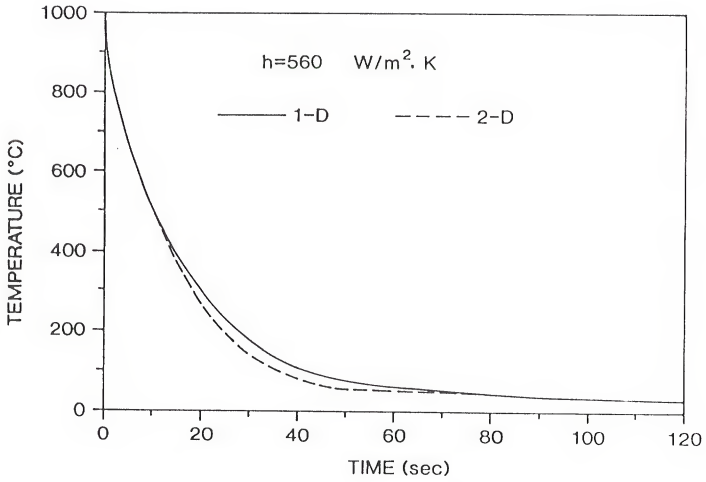

Fig. 4.18 Cooling profiles calculated from the 1-D and 2-D models for a 2-mm-thick disk tempered in air using a heat transfer coefficient of 560 W/m^2-K.

Stress Analyses using Viscoelasticity and Structural Relaxation

A. Gaseous Cooling Media

Computer programs in Basic language were developed by P. H. DeHoff (Mechanical Engineering and Engineering Science Department, University of North Carolina at Charlotte) on an IBM microcomputer to determine the transient and residual stresses induced within a porcelain plate during a cooling treatment. These programs which are referred to as "fictive temperature" and "stress" programs, incorporate linear viscoelasticity and structural relaxation behavior of porcelain and were used by DeHoff and Anusavice [66] to calculate the thermal stresses in a single layer porcelain plate symmetrically cooled on both sides from an initial temperature of 800°C. A summary of the procedures employed in this analysis is given in chapter I and in Appendix A. However, for a more complete description of the analytical and numerical techniques, one should refer to the original study [66]. In the following calculations of the thermal stresses, the edge effect of the porcelain disk is neglected and it is assumed that the stress distributions produced within a porcelain disk are similar to that within a porcelain plate.

The temperature versus time data which were calculated from the 1-D thermal model (eq. 57) for each cooling condition were incorporated in the "fictive temperature" program and the transient fictive temperature distribution for that cooling condition was calculated. The fictive temperature is the quenching temperature of glass corresponding to a particular structural state (see eq. A-3). Using procedures utilized by DeHoff and Anusavice [66], a glassy and a liquid state for the body porcelain were defined by a linear regression fit to the measured

thermal contraction data. To compare the results of this study with the results of analyses performed in the original paper [66], the contraction data at temperatures greater than 400°C were used for the liquid and at temperatures below 400°C for the glassy states (elastic solid state) of porcelain. The transient fictive temperatures calculated for each disk and the thermal contraction values for the liquid and glassy states were applied in the "stress" program to determine the induced transient and residual stresses. It should be emphasized that in this study, the thermal contraction coefficients were measured at a constant cooling rate of 3°/min. However, this property can be significantly influenced by the rate of cooling employed in the dilatometer.

Shown in Fig. 4.19 is the actual and fictive transient temperatures at the surface and the insulated face of a 2-mm-thick disk subjected to free convective (FC) cooling in air from an initial temperature of 982°C. The fictive temperatures reached an asymptotic value of approximately 600°C after 70 sec. Above this temperature, there is only small difference between the actual and the fictive temperatures. Also, at 70 sec after cooling, there is a negligible temperature gradient within the disk. In the "stress" program, the actual and fictive temperature distribution within the disk at any given time are fit by quadratic equations. The corresponding transient stresses at the top and bottom (insulated) surfaces as a function of time are shown in Fig. 4.20. At approximately 300 sec after cooling when the disk reached a constant temperature (Fig. 4.19), the stresses also approached a fixed value (Fig. 4.20). The magnitude of the compressive stresses within the top surface and tensile stresses at the bottom surface increased rapidly at about 70 sec after initial cooling. The residual stresses within the disk versus the distance from the surface are shown in Fig. 4.21. The maximum compressive and tensile stress values of 24.2 and 11.1 MPa which

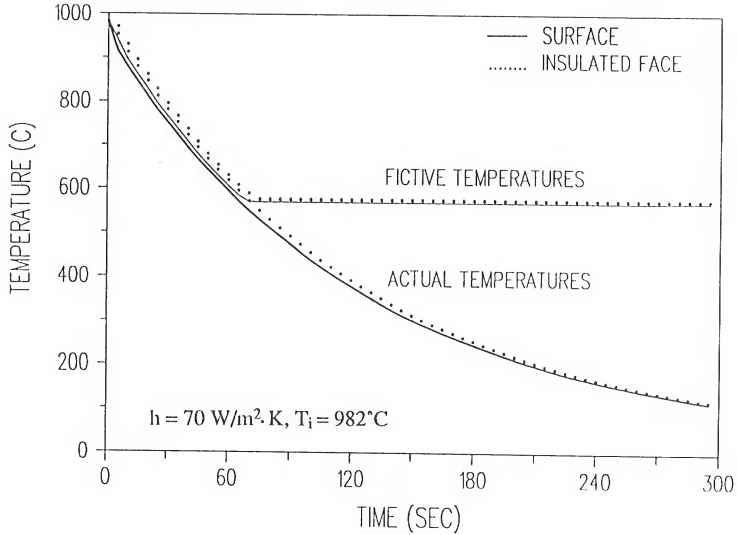

Fig. 4.19 Actual and fictive temperature versus time profiles at the surface and the insulated face of a 2-mm-thick body porcelain disk cooled by free convection from an initial temperature of 982°C.

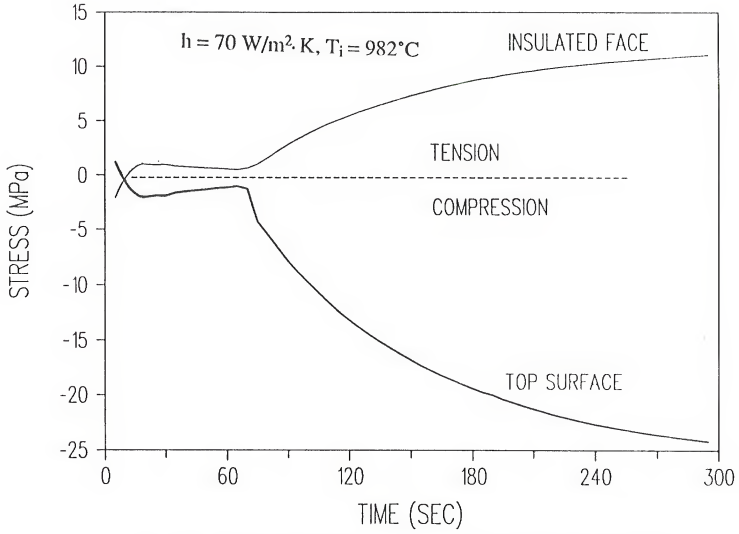

Fig. 4.20 Transient stresses versus time at the surface and the insulated face of a 2-mm-thick body porcelain disk cooled by free convection from an initial temperature of 982°C.

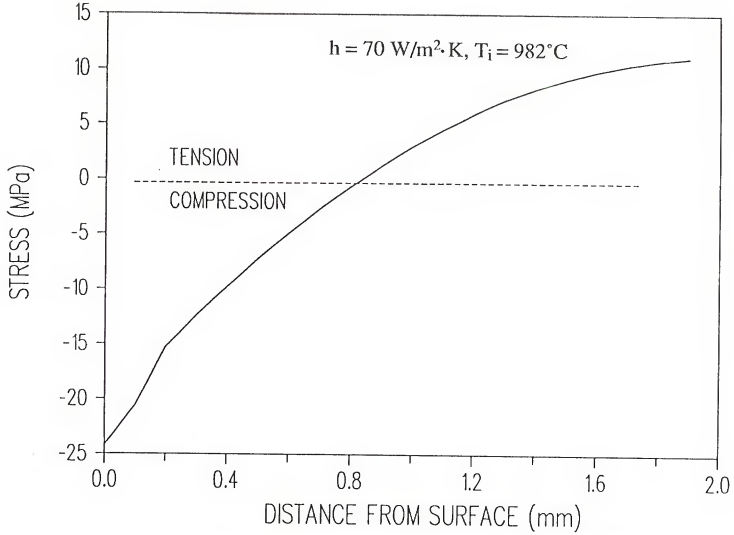

Fig. 4.21 Residual stress distribution in a 2-mm-thick body porcelain disk subjected to free convective cooling from an initial temperature of 982°C.

correspond to a ratio of 2.1, were produced at the top and bottom surfaces, respectively.

Figs. 4.22 to 4.24 correspond to the temperature and stress data for free convective cooling of a 6-mm-thick disk. Compared with the disk with a thickness of 2 mm, larger actual and fictive temperature gradients are produced within this disk at any given time (Fig. 4.22). A fictive temperature of 570°C was reached at the surface after 180 sec. During the initial stage of cooling, relatively large tensile stresses were induced at the surface (Fig. 4.23). At about 30 sec after initial cooling, these stresses rapidly decreased in magnitude and became compressive in nature. However, as stated in Chapter I, these tensile stresses are highly undesirable. Experimental cooling of several 6-mm thick disks resulted in thermal shock failure, specifically for the bilayered ($\Delta\alpha$ =+3.2 or –1.5) specimens. The failure occurred during various stages of free convective cooling in which pieces of porcelain were violently separated from the disk. The cause of the thermal shock failure was the development of relatively large tensile stresses at the top surface during the initial stage and at the interior during a later stage of cooling. These stresses were developed because of the combined effect of the thermal contraction incompatibility and temperature gradient within the 6–mm–thick disks. The residual stress distribution as a function of distance from the top surface is shown in Fig. 4.24. This figure shows that if a disk does not break because of initial tensile stresses at the surface, it will have a compressive stress layer approximately 2.42 mm in depth. Since the preparation and cooling treatments of a 6-mm-thick disks were associated with several failures, additional experiments were performed only for the 2-mm thick specimens.

To determine the influence of the initial temperature on the effectiveness of tempering, the single layer body porcelain disks, ($\Delta\alpha$ = 0.0), having a 2 mm

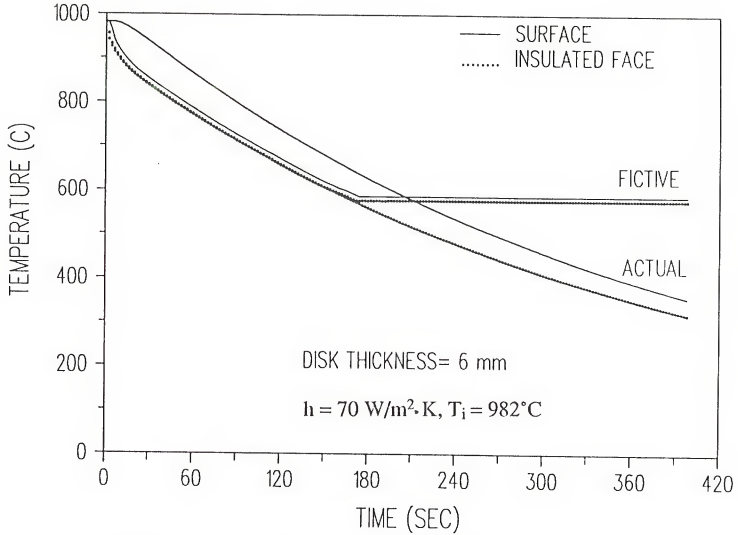

Fig. 4.22 Actual and fictive temperature versus time profiles at the surface and the insulated face of a 6-mm-thick body porcelain disk cooled by free convection from an initial temperature of 982°C.

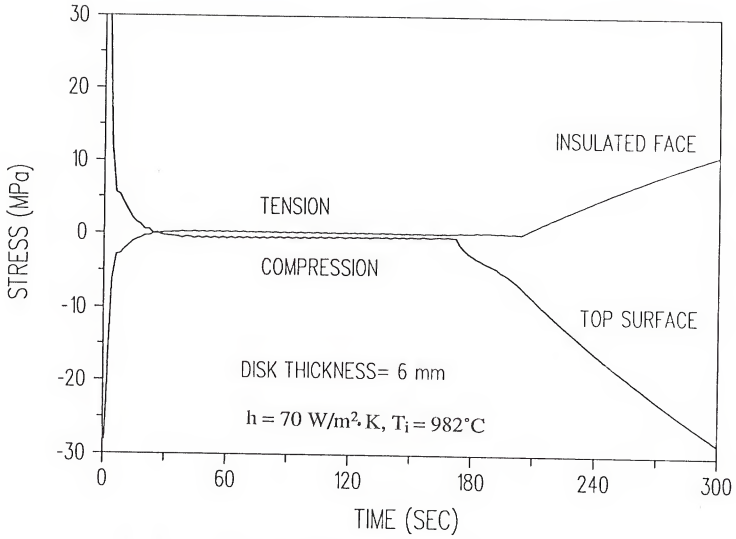

Fig. 4.23 Transient stresses versus time at the surface and the insulated face of a 6-mm-thick body porcelain disk cooled by free convection from an initial temperature of 982°C.

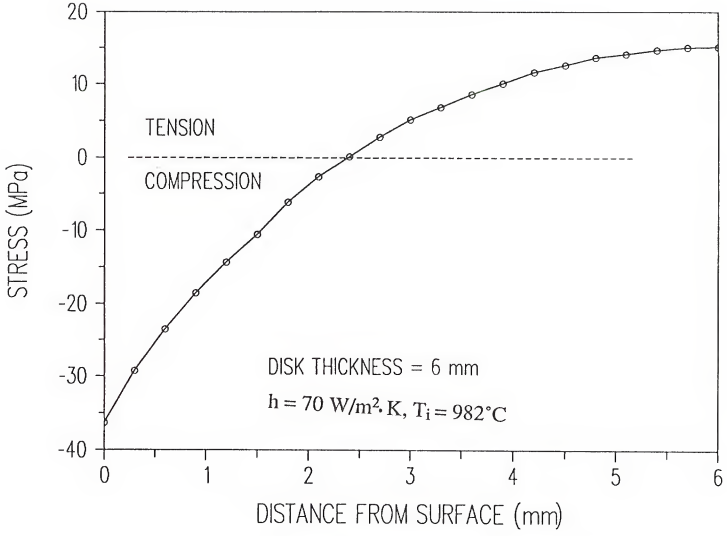

Fig. 4.24 Residual stress distribution in a 6-mm-thick body porcelain disk subjected to free convective cooling from an initial temperature of 982°C.

thickness, were tempered by a vertical air jet (TV) from initial temperatures of 982, 850, 750 and 650°C. Shown in Figs 4.25 to 4.37 are the results of thermal stress analyses for these tempered specimens. Six disks in each group were prepared and the effectiveness of the tempering treatment was analyzed experimentally by the biaxial flexure test. These results will be presented in a separate section. As stated earlier, the average heat transfer coefficient of 560 $W/m^2.K$, was determined based on the slope of the cooling curve from a copper disk. Shown in Fig. 4.25 are the actual and fictive temperature versus time profiles at the surface and the insulated face of a 2-mm-thick body porcelain disk tempered from an initial temperature of 982°C. Compared with the profiles from the free convective cooling (Fig. 4.19), larger temperature gradients for actual and fictive curves were produced within the tempered specimens independent of the initial tempering temperature (Figs. 4.25, 4.28, 4.31 and 4.34). The asymptotic values obtained for fictive temperatures were not significantly influenced by the initial tempering temperature. In all cooling profiles, the tempered disks reached an ambient temperature of 30°C in about 60 seconds. This is consistent with the experimentally determined cooling profiles presented earlier.

Shown in Fig. 4.26 are the transient stresses versus time at the surface and insulated face of a 2-mm-thick body porcelain disk tempered from an initial temperature of 982°C. Approximately 10 sec after initiation of tempering, the transient compressive stresses produced at the surface increased in magnitude and in about 45 sec reached a constant value. This was also true for the disks tempered from lower initial temperatures (Figs. 4.29, 4.32 and 4.35). However, the magnitude of the transient stresses at any given time was influenced by the initial soak temperature. The transient stress profiles indicate that an increase in the surface compression corresponds to a greater amount of undesirable interior tensile

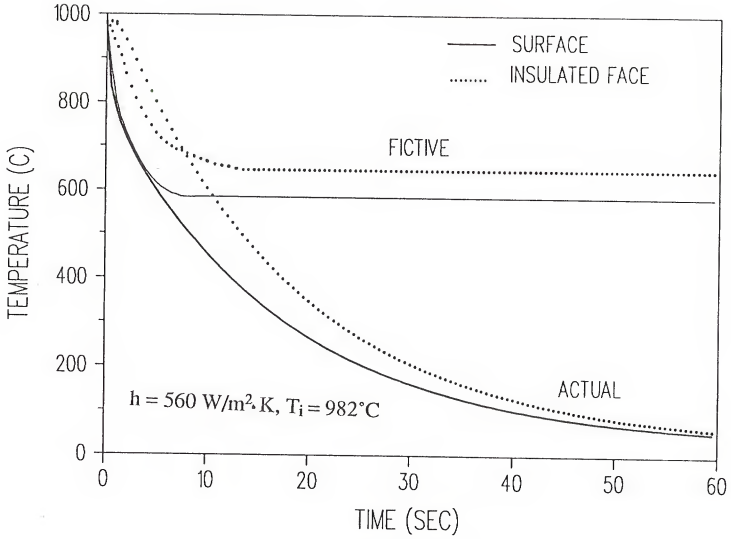

Fig. 4.25 Actual and fictive temperature versus time profiles at the surface and the insulated face of a 2-mm-thick body porcelain disk tempered from an initial temperature of 982°C.

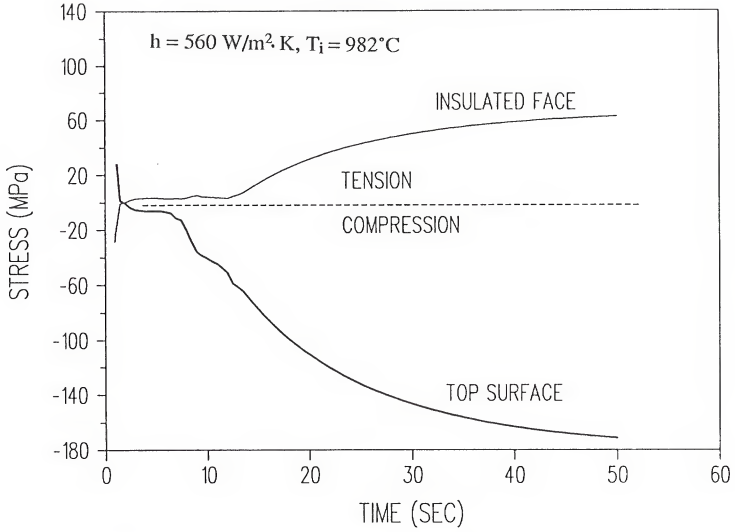

Fig. 4.26 Transient stresses versus time at the surface and the insulated face of a 2-mm-thick body porcelain disk tempered from an initial temperature of 982°C.

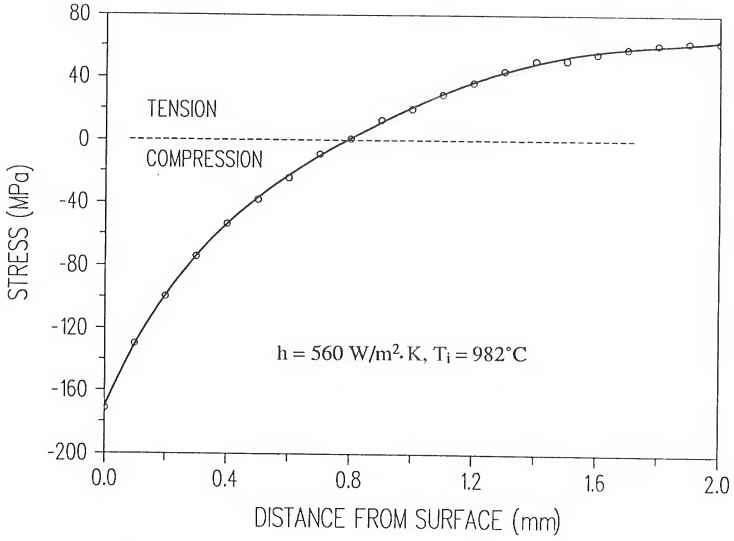

Fig. 4.27 Residual stress distribution in a 2-mm-thick body porcelain disk tempered from an initial temperature of 982°C.

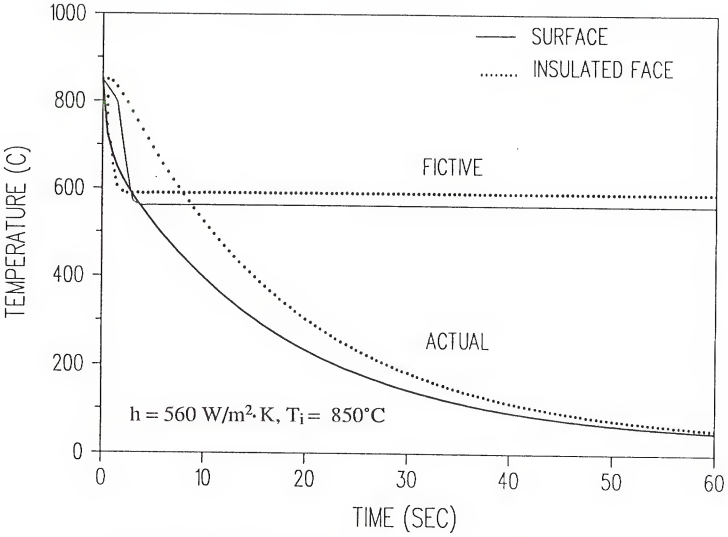

Fig. 4.28 Actual and fictive temperature versus time profiles at the surface and the insulated face of a 2-mm-thick body porcelain disk tempered from an initial temperature of 850°C.

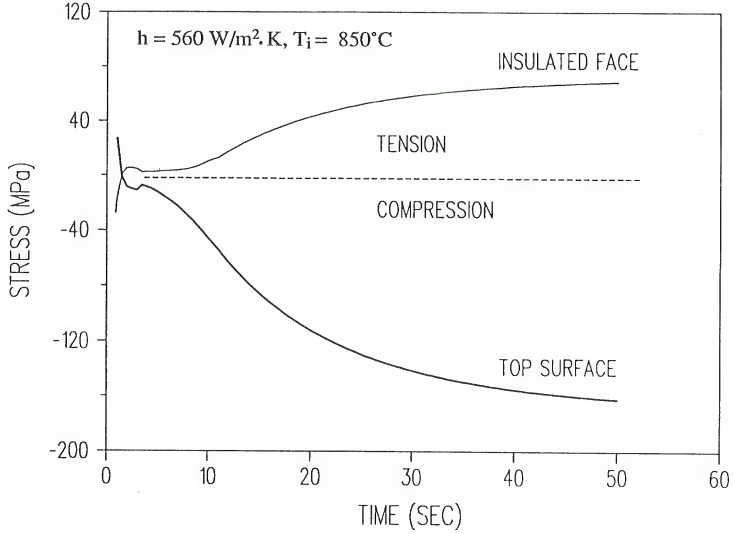

Fig. 4.29 Transient stresses versus time at the surface and the insulated face of a 2-mm-thick body porcelain disk tempered from an initial temperature of 850°C.

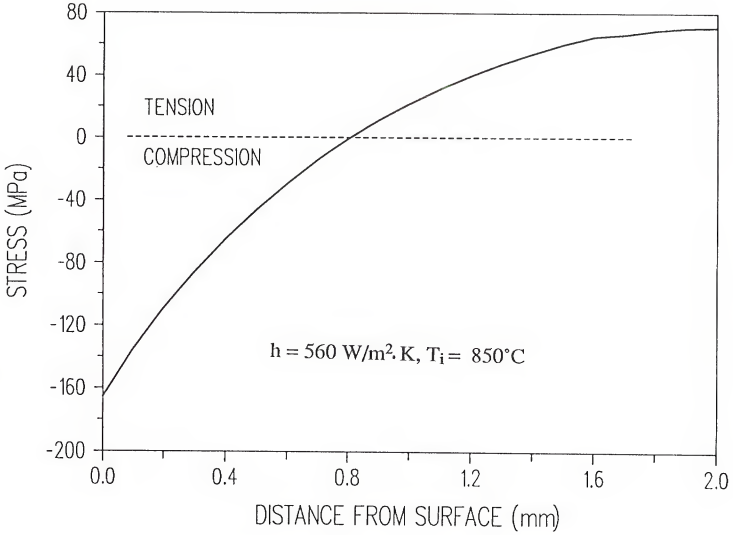

Fig. 4.30 Residual stress distribution in a 2-mm-thick body porcelain disk tempered from an initial temperature of 850°C.

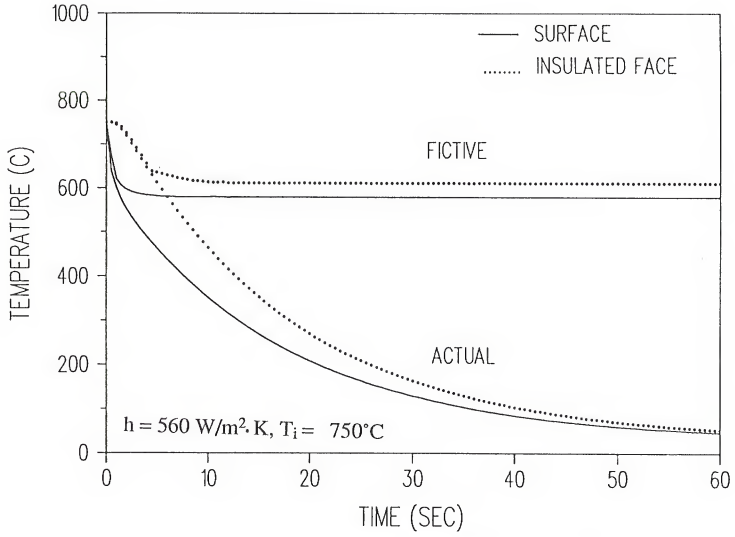

Fig. 4.31 Actual and fictive temperature versus time profiles at the surface and the insulated face of a 2-mm-thick body porcelain disk tempered from an initial temperature of 750°C.

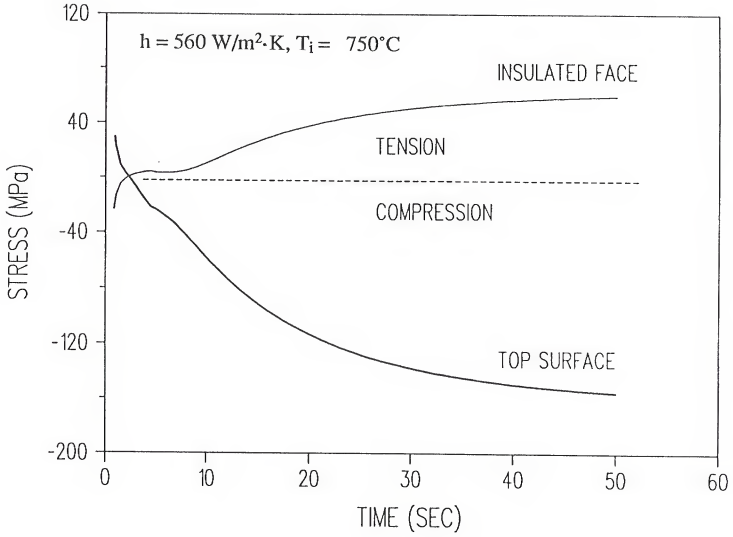

Fig. 4.32 Transient stresses versus time at the surface and the insulated face of a 2-mm-thick body porcelain disk tempered from an initial temperature of 750°C.

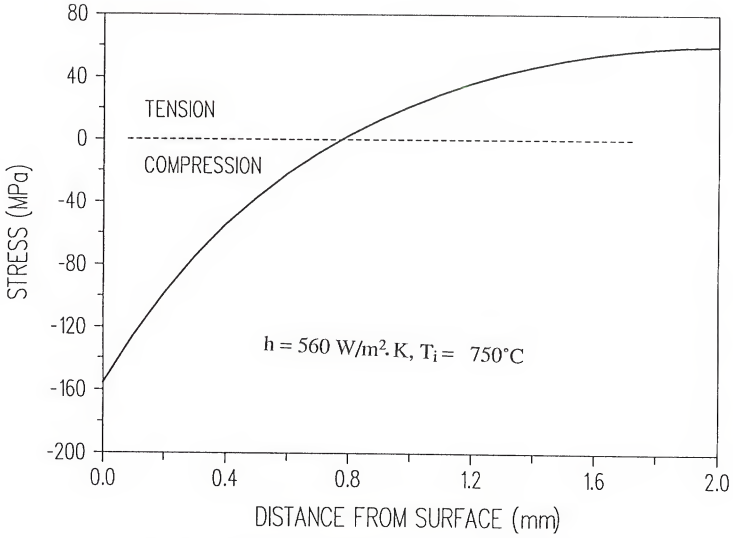

Fig. 4.33 Residual stress distribution in a 2-mm-thick body porcelain disk tempered from an initial temperature of 750°C.

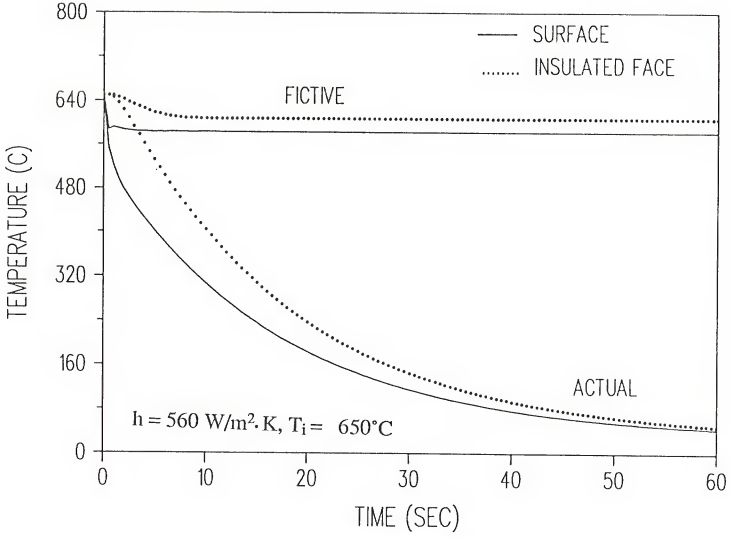

Fig. 4.34 Actual and fictive temperature versus time profiles at the surface and the insulated face of a 2-mm-thick body porcelain disk tempered from an initial temperature of 650°C.

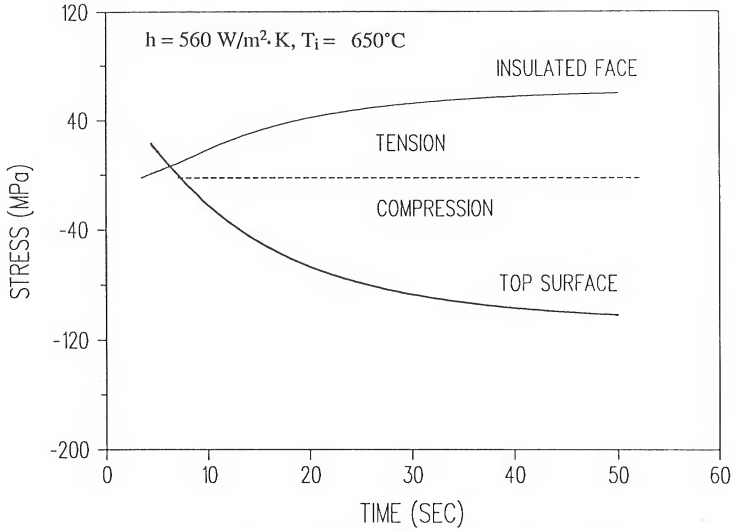

Fig. 4.35 Transient stresses versus time at the surface and the insulated face of a 2-mm-thick body porcelain disk tempered from an initial temperature of 650°C.

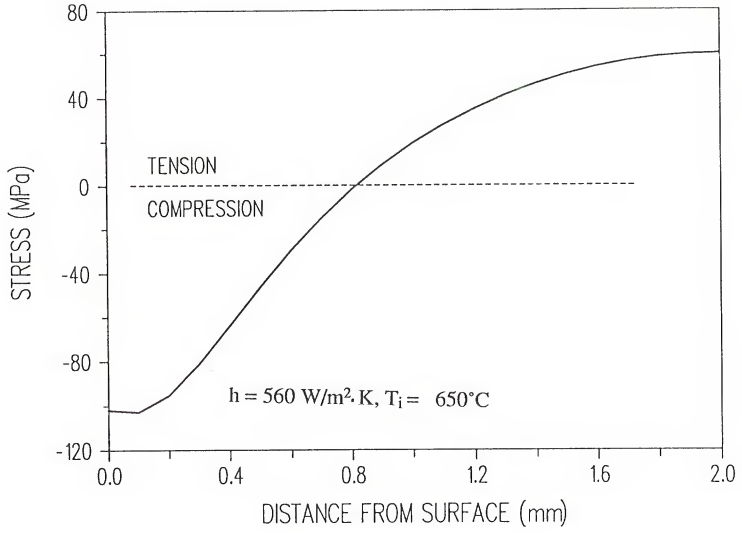

Fig. 4.36 Residual stress distribution in a 2-mm-thick body porcelain disk tempered from an initial temperature of 650°C.

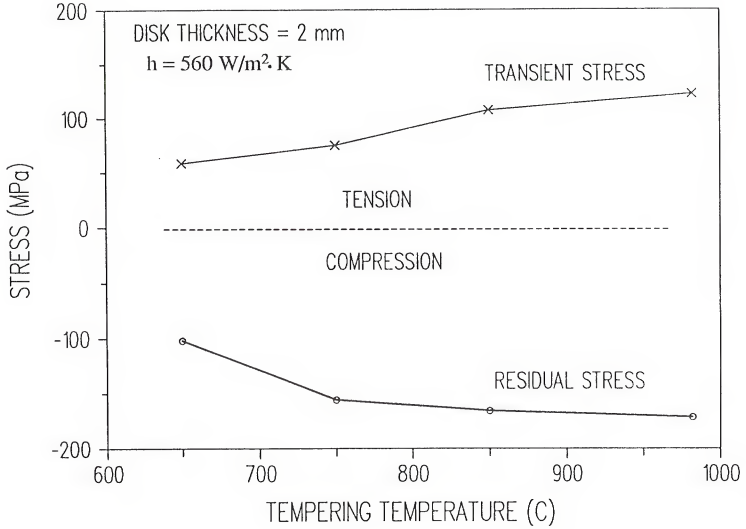

Fig. 4.37 Residual compressive and tensile stresses at the surface of a 2-mm-thick body porcelain disk as a function of initial tempering temperature.

stresses. However, in general the surface compressive stresses produced in a disk at any given time are greater in magnitude than the interior tension. The residual stress distribution in a 2-mm-thick body porcelain disk tempered from an initial temperature of 982°C is shown in Fig. 4.27. The maximum compressive and tensile stresses produced at the surface and the insulated face were 171.4 MPa and 62.6 MPa, respectively. Under this condition, the magnitude of the surface compression was 2.7 time greater than that of the maximum tension. The beneficial compressive stresses induced at the surface of the tempered disks from initial temperature of 850, 750 and 650°C, were 165.8 MPa (Fig. 4.30), 155.9 MPa (Fig. 4.33) and 102.0 MPa, respectively. These stresses were greater than their corresponding maximum tensile stresses by factors of 2.3, 2.6 and 1.7, for the initial tempering temperatures of 850, 750, and 650°C, respectively. As stated earlier, the corresponding factor for the free convective cooling was 2.1. This indicates that, the ratio of the surface compression to the maximum tension is not strongly influenced by the initial tempering temperature. However, a small change in this ratio can make a significant difference in the strength and fracture characteristics of porcelain. Gardon [24], introduced the idea of "modulated quenching" to control this ratio and to obtain the desired strength and fracture characteristics in a glass plate.

Shown in Fig. 4.37 is the residual compressive stresses produced at the surface of a 2-mm-thick porcelain disk as a function of initial tempering temperature. An increase of the soak temperature from 650 to 750°C will result in a relatively large increase in the compressive stress value. However, any further increase in the initial temperature does not significantly increase the surface compression. Also, a greater increase in the ratio of the surface compression to the maximum tension corresponds to an increase in the initial tempering temperature

from 650 to 750°C. Since the structural distortion of the specimens due to viscous flow may occur at high temperatures, for the same tempering effectiveness a smaller soak temperature is more desirable. In this study an optimum value for the soak temperature is determined from this result and the data obtained from the biaxial flexure test.

B. Liquid Cooling Media

Shown in Fig. 4.38 to 4.40 are the results for the 2-mm-thick porcelain disk quenched in silicone oil from an initial temperature of 850°C. The mean value of heat transfer coefficient for this condition was 720 $W/m^2 \cdot K$ which was applied both on the top and bottom surfaces. Because of the symmetric cooling condition, the midplane of the disk was treated like an insulated boundary and the transient temperature distributions were obtained from the results of the Laplace transformation approach (equations 46 and 57) using an "a" dimension of 1 mm. At the initial stage of quenching, a relatively large temperature gradient from the surface to the midplane was produced (Fig. 4.38) because of the large value of the heat transfer coefficient. The fictive and the actual temperatures approached their asymptotic values after 5 and 25 sec, respectively. Since the entire disk reached the oil temperature of 100°C in about 25 sec (Fig. 4.38), the transient stresses at the surface and midplane subsequently stayed constant (Fig. 4.39). Shown in Fig. 4.40 is the symmetric distribution of the residual stresses within the disk as a function of the distance from the center. A maximum compressive stress value of 107.8 MPa was produced at the surfaces. The largest residual tensile stress value which occurred at the midplane of the disk was 44.3 MPa. Under this condition, the ratio of the surface compression to the maximum interior tension was 2.4 and the thickness of the compressive layer at each side was approximately 0.4 mm.

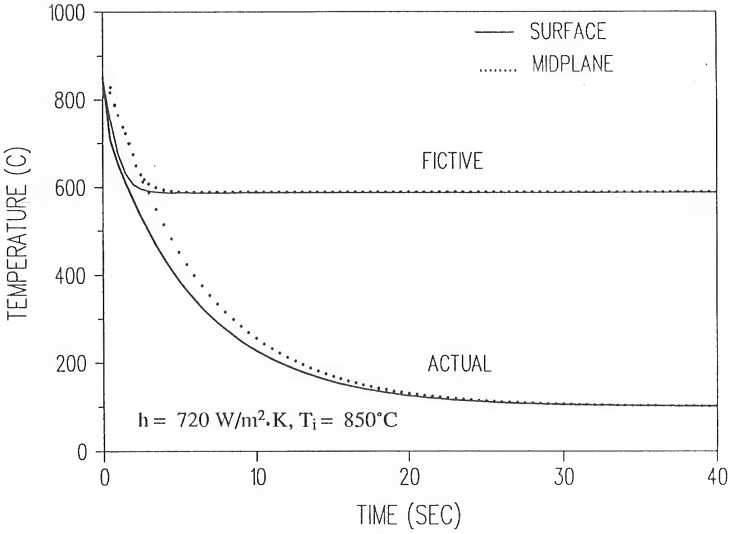

Fig. 4.38 Actual and fictive temperature versus time profiles at the surface and midplane of a 2-mm-thick body porcelain disk quenched in silicone oil from an initial temperature of 850°C.

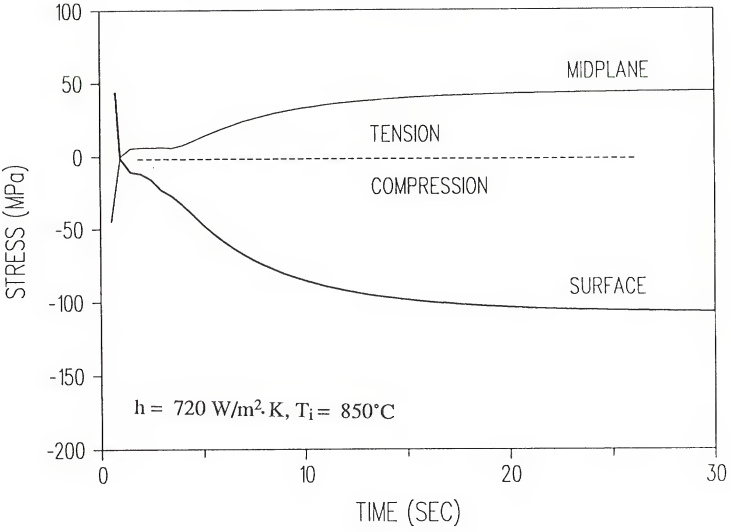

Fig. 4.39 Transient stresses versus time at the surface and midplane of a 2-mm-thick body porcelain disk quenched in silicone oil from an initial temperature of 850°C.

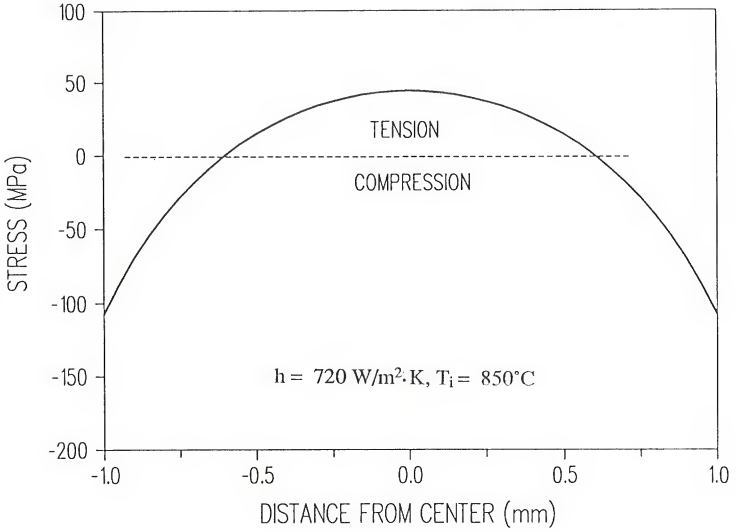

Fig. 4.40 Residual stress distribution in a 2-mm-thick body porcelain disk quenched in silicone oil from an initial temperature of 850°C.

For the same initial temperature of 850°C, the maximum stresses produced in the oil quenched specimens were smaller than those of the tempered specimen in air. However, the results of a 2-mm-thick disk tempered from one side and insulated from another side are the same as a 4-mm-thick disk symmetrically tempered from both sides. Therefore, because of a larger effective thickness, at a given time, the temperature gradient produced within the disks during non-symmetrical cooling in air was greater than the corresponding values during symmetrical cooling in silicone oil. It should be emphasized that the silicone oil temperature was kept at 100°C to prevent thermal shock failure. To analyze the effect of a cooling medium with a very large heat transfer coefficient on the temperature and stress characteristics of a single layer porcelain, the results of quenching a 2-mm-thick disk in water were determined and are shown in Figs. 4.41 and 4.42. The initial temperatures of the disk and water were 850°C and 100°C, respectively. The mean value of the heat transfer coefficient applied in this analysis was 1590 $W/m^2 \cdot K$ which was determined from the slope of the cooling curve for the copper disk (Fig. 4.12). Approximately, 15 sec after quenching, the entire disk reached the water temperature of 100°C (Fig. 4.41). Midplane tension and the surface compression reached constant values of 91.0 MPa and 243.0 MPa, respectively (Figs. 4.42 and 4.43). Comparison between Figs. 4.40 and 4.43 indicates that under this condition, the depth of the residual compressive stress layer is not influenced by the heat transfer coefficient and is approximately 0.4 mm for both cases. However, under this condition, thermal shock failure occurred because of the large tensile stresses which developed within the surface at the initial stage or at the interior during later stages of quenching.

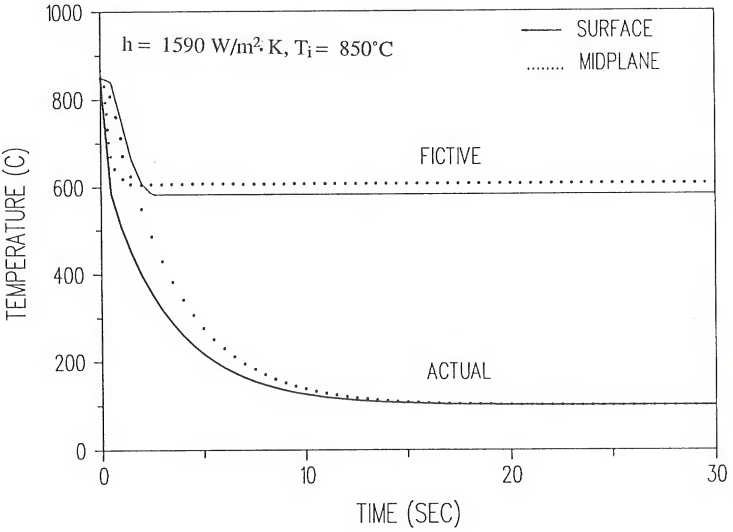

Fig. 4.41 Actual and fictive temperature versus time profiles at the surface and midplane of a 2-mm-thick body porcelain disk quenched in water from an initial temperature of 850°C.

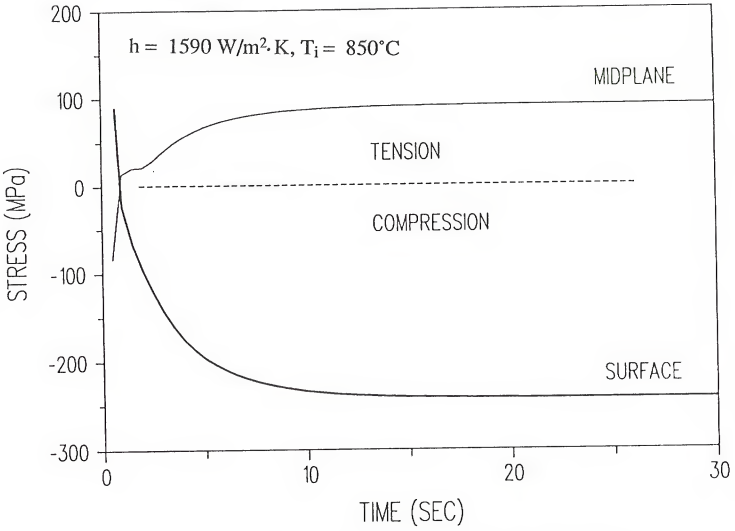

Fig. 4.42 Transient stresses versus time at the surface and midplane of a 2-mm-thick body porcelain disk quenched in water from an initial temperature of 850°C.

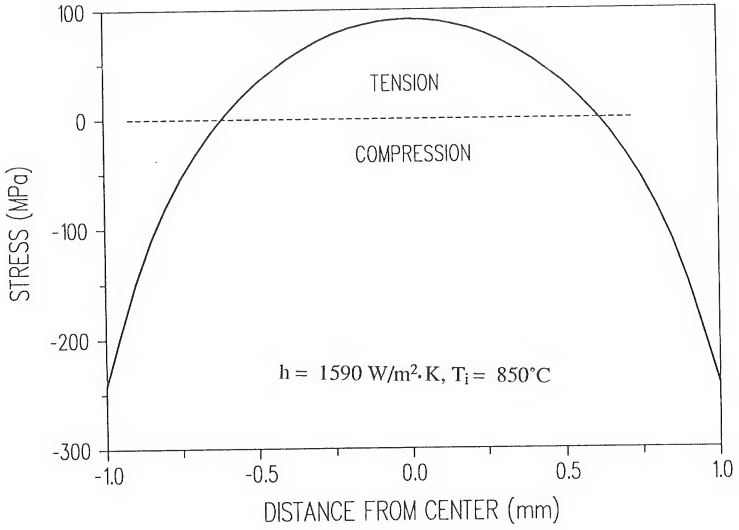

Fig. 4.43 Residual stress distribution in a 2-mm-thick body porcelain disk quenched in water from an initial temperature of 850°C.

Stress Analyses using Finite Element Method

A. Transient Stress Analysis of Bilayered Ceramic Disks

The stress analysis by viscoelastic and structural relaxation theory which was presented earlier only determined the stresses for a single–layered ceramic disk by using a specific stress condition of a two–dimensional model. This model assumed that the stress components along the horizontal and vertical directions were identical. In this section, the influence of a thermal contraction mismatch on the transient stresses within a bilayered disk was analyzed by using an axisymmetric model. However, this model assumed that the viscoelastic stresses were relaxed during cooling through the glass transition region.

Shown in Fig. 4.44 is a comparison between the experimental and the calculated cooling profiles for free convective cooling of a 2–mm-thick disk from an initial temperature of 982°C in helium. At the time that the temperature at the thermocouple location (node number 103 in Figs. 3.3 and 3.4) approached the glass transition temperature (T_g = 600°C), the difference between the experimental and the calculated temperatures was negligibly small. Shown in Fig. 4.45 are the temperature contours near this glass transition temperature which are perpendicular to the insulated surface (bottom) and the symmetrical (left side) boundaries. The largest temperature value (599.8°C) corresponds to node 1 and the regions adjacent to it (see Fig. 3.4 for the identification of node numbers) and the smallest value (496.9°C) corresponds to the upper right corner node (number 153). This temperature distribution was obtained for a time of 41 sec after the initiation of cooling. The vector plot of the thermal fluxes are shown in Fig. 4.46. These vectors, which are perpendicular to the thermal contours, determine the direction

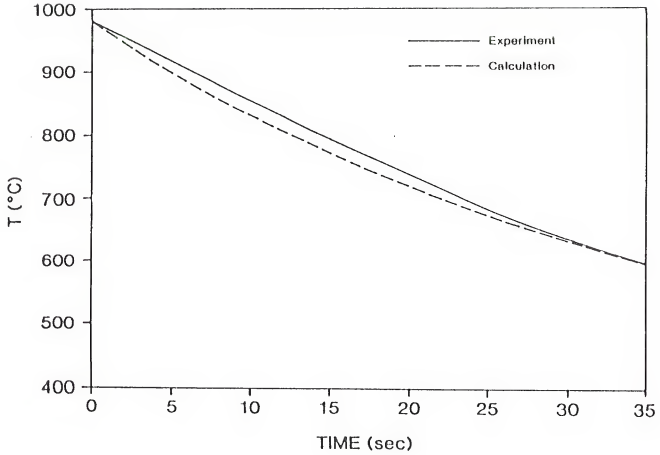

Fig. 4. 44 Experimental and calculated cooling profiles for a 2-mm-thick disk subjected to free convective cooling in helium.

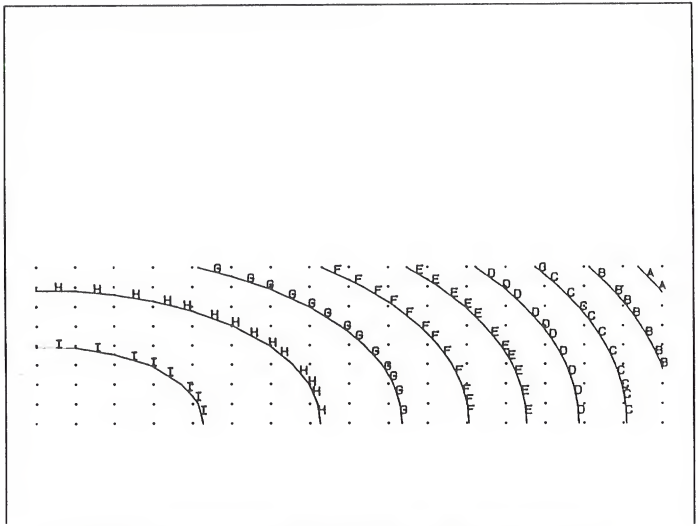

Fig. 4.45 Temperature distribution near glass transition temperature within a 2-mm-thick disk subjected to free convective cooling in helium.

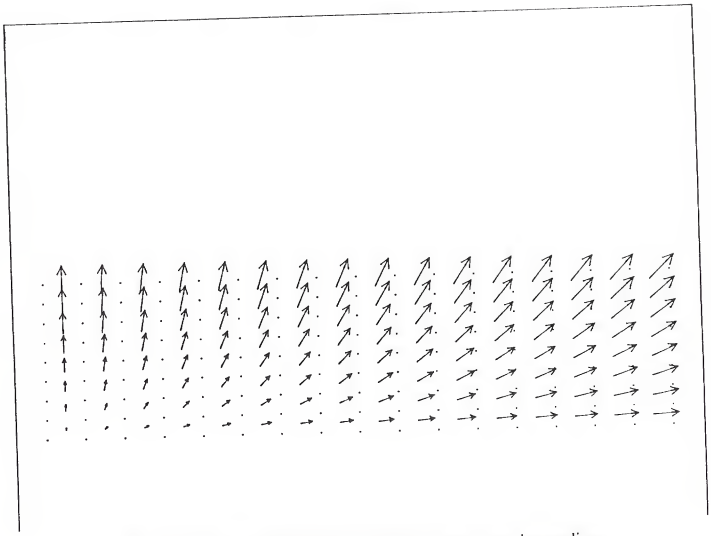

Fig. 4.46 Vector plot of thermal fluxes for free convective cooling of a 2-mm-thick disk in helium.

and magnitude of the heat loss at each location. The nodes which are located on the symmetrical axis and adjacent to it are not significantly affected by the heat loss from the side of the disk. The temperature gradients at these regions are parallel to the vertical axis.

Shown in Figs. 4.47 and 4.48 are principal stress contours, $\sigma 1$ and $\sigma 2$, within a bilayered porcelain disk with a mismatch level of +3.2 ppm/°C. The peak value of the transient tensile stress ($\sigma 1$) was 78.6 MPa (contour E) which occurred near the edge of the disk. The peak transient compressive stress value was 68.2 MPa which occurred at the top surface and near the insulated boundary. These stresses developed because of the combined effect of the temperature gradient within the disk and the thermal contraction difference between the porcelain layers.

Shown in Fig. 4.49 are the temperature contours near T_g for free convective cooling of a 2–mm–thick disk from an initial temperature of 850°C using air as cooling medium. In this study, similar values of thermal conductivity (K), specific heat (C_p) and density (ρ) were used for all porcelain types. Therefore, the temperature distributions for single–layered and bilayered disks are identical. However, because of the difference in thermal contraction mismatch, the transient stress distribution for each porcelain combination was different. shown in Figs. 4.50 and 4.51 are the principal stress contours, $\sigma 1$ and $\sigma 2$, for free convective cooling of a bilayered disk with a mismatch level of +3.2 ppm/°C. Comparison of these figures with Figs. 4.47 and 4.48 indicates that the difference among the stress distributions for disks subjected to cooling treatments in helium and in air is negligibly small.

Shown in Figs. 4.52 and 4.53 are the contours, $\sigma 1$ and $\sigma 2$, for a bilayered porcelain with a mismatch level of –1.5 ppm/°C subjected to free convective cooling in air. The peak values of principal tensile stress ($\sigma 1$) and compressive

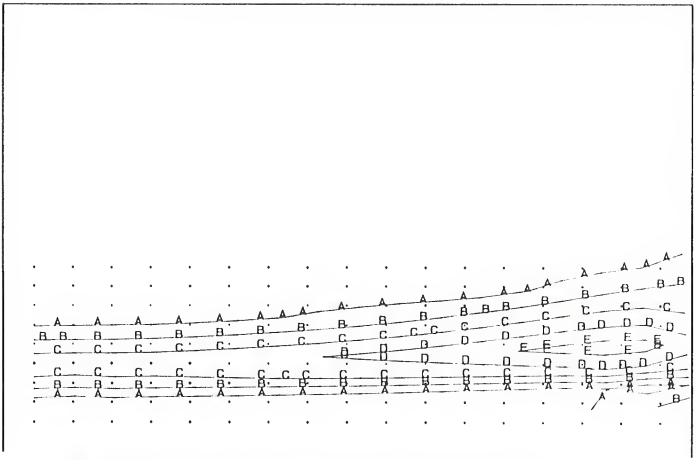

Fig. 4.47 Transient principal stress ($\sigma 1$ in MPa) produced within a 2-mm-thick disk ($\Delta\alpha$ = +3.2 ppm/°C) subjected to free convective cooling in helium (T_i = 982°C).

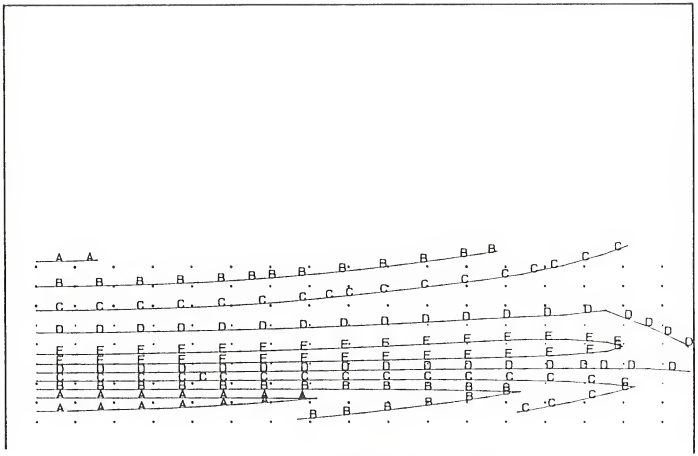

Fig. 4.48 Transient principal stress ($\sigma 2$ in MPa) produced within a 2-mm-thick disk ($\Delta\alpha = +3.2$ ppm/°C) subjected to free convective cooling in helium ($T_i = 982$°C).

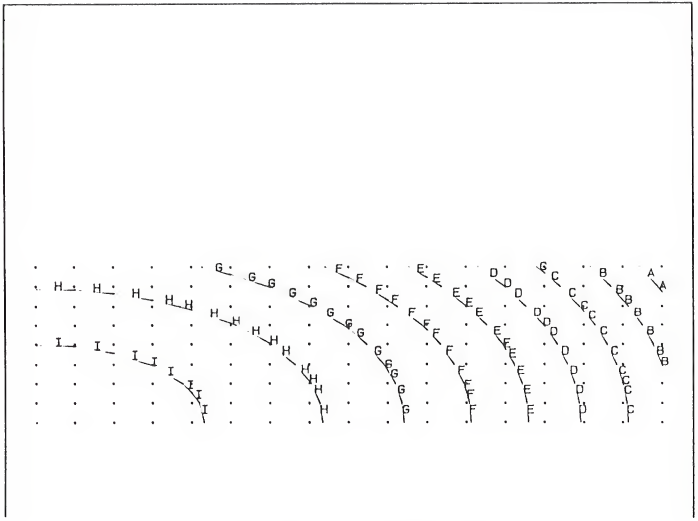

Fig. 4.49 Temperature distribution near T_g (600°C) for free convective cooling of a 2-mm-thick disk in air (T_i = 850°C).

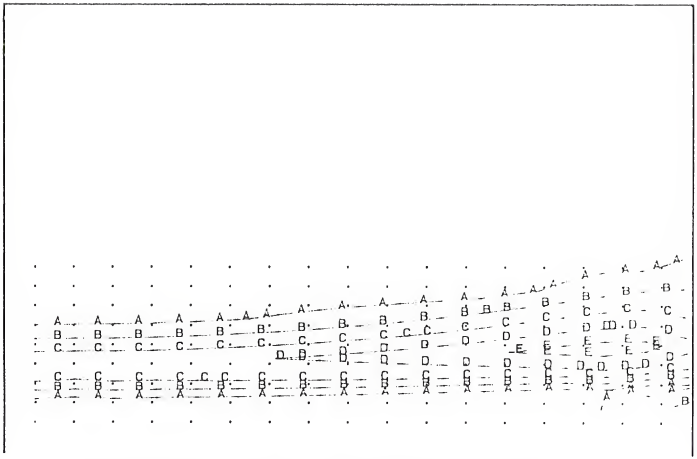

Fig. 4.50 Transient principal stress ($\sigma 1$ in MPa) produced within a 2-mm-thick disk ($\Delta\alpha = +3.2$ ppm/°C) subjected to free convective cooling in air ($T_i = 850$°C).

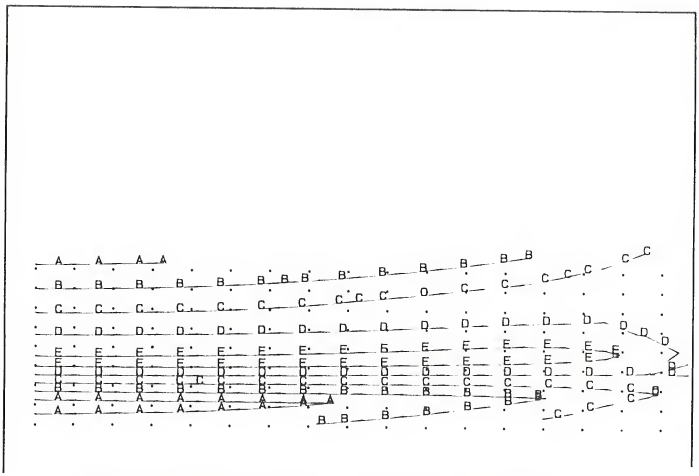

Fig. 4.51 Transient principal stress ($\sigma 2$ in MPa) produced within a 2-mm-thick disk ($\Delta\alpha = +3.2$ ppm/°C) subjected to free convective cooling in air ($T_i = 850$°C).

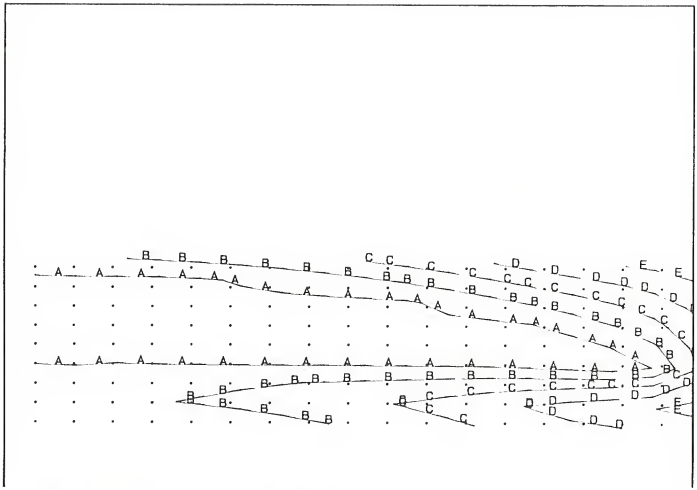

Fig. 4.52 Transient principal stress ($\sigma 1$ in MPa) produced within a 2-mm-thick disk ($\Delta\alpha = -1.5$ ppm/°C) subjected to free convective cooling in air ($T_i = 850$°C).

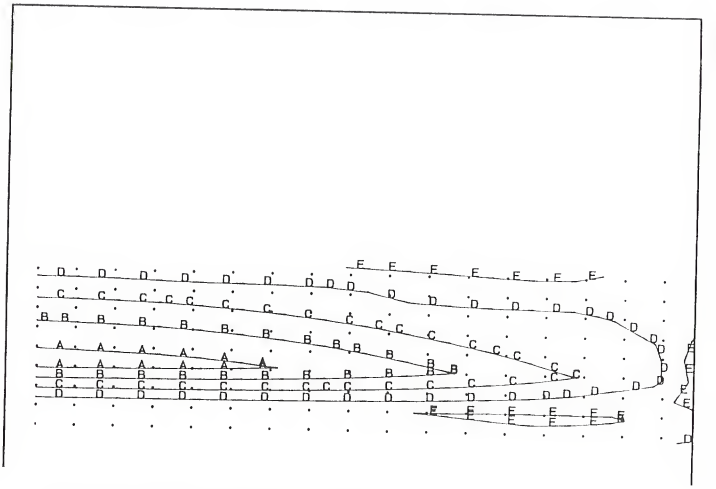

Fig. 4.53 Transient principal stress ($\sigma 2$ in MPa) produced within a 2-mm-thick disk ($\Delta\alpha = -1.5$ ppm/°C) subjected to free convective cooling in air ($T_i = 850$°C).

(σ_2) stress were 55.1 MPa and 49.3 MPa, respectively. Although these stresses were smaller than the corresponding values in a +3.2 ppm/°C mismatch case, comparison of Figs. 4.50 and 4.52 indicates that under this condition the tensile stresses produced at the top surface are relatively larger. Shown in Fig. 4.54 are the superimposed plots of the deformed and undeformed conditions for a disk with a mismatch level of $\Delta\alpha$ = +3.2 ppm/°C. The maximum displacement along the vertical direction was 0.02 mm which occurred at point B (node 153 in Fig. 3.4). Since the incompatibility stresses are not present in a single–layered specimen ($\Delta\alpha$ = 0.0), the disk is not subjected to bending. Under this condition, the maximum vertical displacement was 0.012 mm (Fig. 4.55). Shown in Figs. 4.56 and 4.57 are stress contours, σ_1 and σ_2 for the free convective cooling of a 2–mm thick body porcelain disk. Comparison of these figures with Fig. 4.49 indicates that in the absence of incompatibility stresses, the stress contours are in the same direction as the temperature contours and are perpendicular to the insulated and symmetrical boundaries. Comparison of Figs. 4.56 and 4.57 with Figs. 4.50 and 4.51 indicates that the peak σ_1 and σ_2 values for a mismatch level of +3.2 ppm/°C were at least two times larger than the corresponding values for the body porcelain disks. Therefore, under the free convective cooling condition, the influence of the thermal contraction mismatch on the transient stresses was significant. Shown in Figs. 4.58 and 4.59 are the σ_1 and σ_2 stress distributions at the surface of a body porcelain as a function of disk radius. The minimum and maximum transient tensile stresses (σ_1) occurred at the center and edge of the disk, respectively (Fig. 4.58). However, the maximum compressive stress (σ_2) at the surface occurred at a point with radius of 5.0 mm (Fig. 4.59). The principal stresses at the edge of the disk as a function of distance from the bottom surface are shown in Figs. 4.60 and 4.61. The transient tensile stress distribution (σ_1) along this direction (Fig. 4.60)

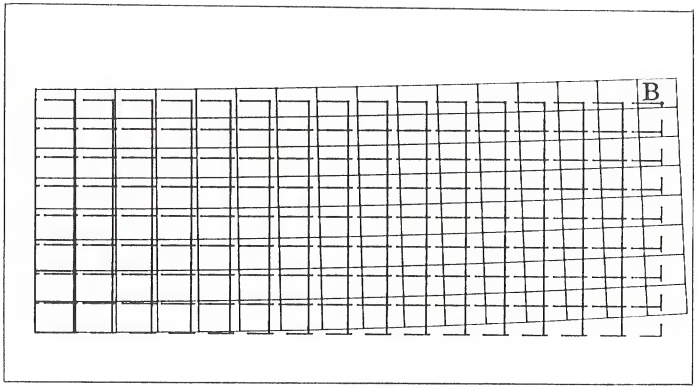

Fig. 4.54 Superimposed plots of the deformed and undeformed disk ($\Delta\alpha = +3.2$ ppm/°C) under the influence of transient thermal and incompatibility stresses.

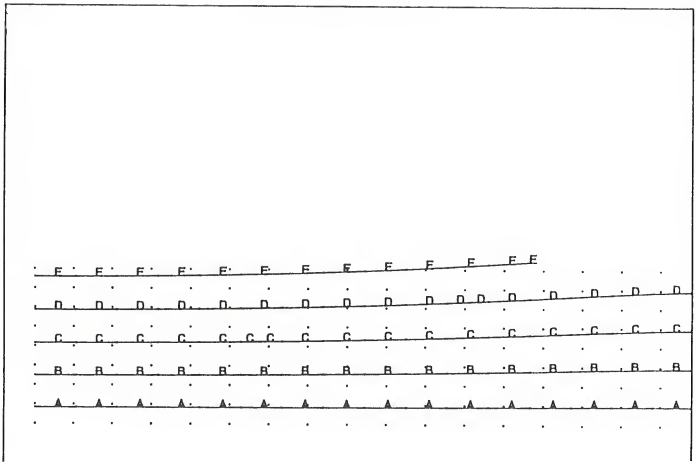

Fig. 4.55 Displacements along the vertical direction (mm) for a 2-mm -thick disk ($\Delta\alpha = 0$) subjected to free convection.

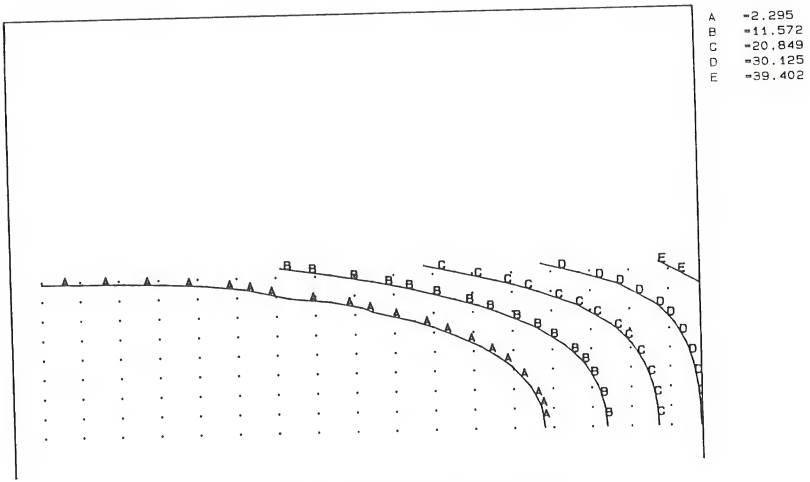

Fig. 4.56 Transient principal stress ($\sigma 1$ in MPa) produced within a 2-mm-thick disk ($\Delta\alpha = 0$) subjected to free convective cooling in air ($T_i = 850°C$).

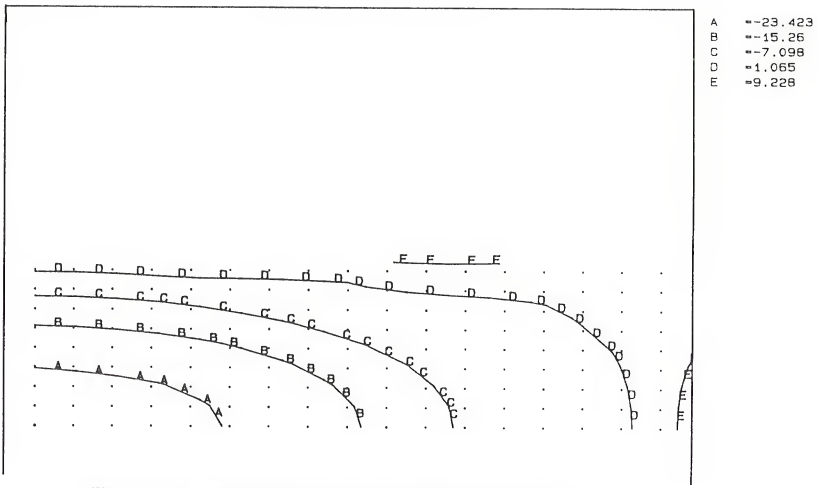

Fig. 4.57 Transient principal stress ($\sigma 2$ in MPa) produced within a 2-mm-thick disk ($\Delta\alpha = 0$) subjected to free convective cooling in air ($T_i = 850°C$).

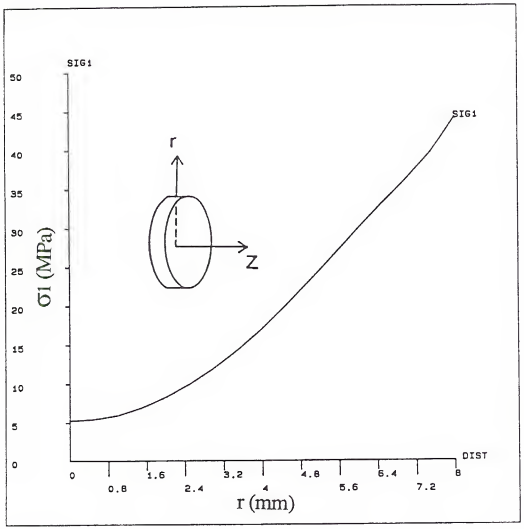

Fig. 4.58 Transient principal stress ($\sigma 1$ in MPa) produced at the surface of a 2-mm-thick disk ($\Delta\alpha = 0$) subjected to free convective cooling in air as a function of radius ($T_i = 850°C$).

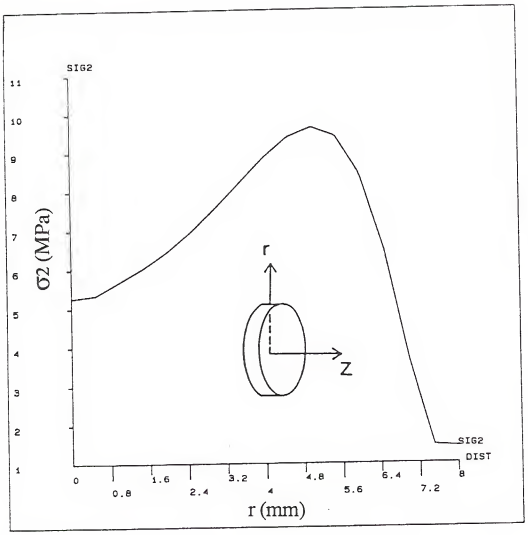

Fig. 4.59 Transient principal stress ($\sigma 2$ in MPa) produced at the surface of a 2-mm-thick disk ($\Delta\alpha = 0$) subjected to free convective cooling in air as a function of radius ($T_i = 850°C$).

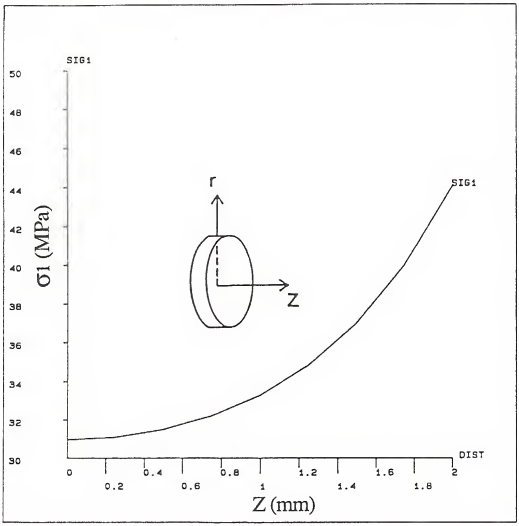

Fig. 4.60 Transient principal stress ($\sigma 1$ in MPa) produced at the edge of a 2-mm-thick disk ($\Delta\alpha = 0$) subjected to free convective cooling in air as a function of thickness ($T_i = 850°C$).

is parabolic in shape with a minimum value of 31 MPa at the bottom (node 17 in Fig. 3.5) and maximum value of 44 MPa at the top surface (node 153). The peak value of σ_2 stress was 13.0 MPa (Fig. 4.61) which occurred at the bottom edge.

Shown in Fig. 4.62 are the temperature contours near T_g (600°C) within a 6-mm-thick disk subjected to free convective cooling in air from an initial temperature of 982°C. These temperature occurred 146 sec after the initiation of cooling. Compared with the 2-mm-thick disk (Fig. 4.49), this disk was subjected to a larger temperature gradient along the thickness and along the radius. Shown in Figs. 4.63 and 4.64 are stress contours, the σ_1 and σ_2 for the bilayered disk with a mismatch level of 3.2 ppm/°C. The gradient of principal tensile stress (Fig. 4.63) increased with the radius and it was maximum at the edge of the disk. However, at this location the gradient of the principal compressive stress (σ_2) was minimum. Although the transient stresses at this stage of cooling are not significantly greater than the corresponding stresses in a 2-mm-thick disk, the interaction of these stresses with the microcracks and flaws, which are probably more likely to be present in a 6-mm-thick disk due to laboratory techniques, can cause thermal shock failure. As mentioned earlier, several experiments, which were conducted for free convective cooling of the 6-mm-thick disks, resulted in thermal shock failure at various stages of cooling. Therefore, tempering analysis was performed only for the 2-mm-thick disks.

Shown in Fig. 4.65 is the temperature versus time profiles for three selected nodes located on axis of symmetry in a 2-mm-thick disk subjected to tempering by air from an initial temperature of 850°C. At the initial stage of tempering, a significant temperature gradient occurred along the disk thickness (between nodes 1 and 137). This gradient reduced in magnitude at a later time. The temperatures at node 103 which correspond to the thermocouple location agreed well with the

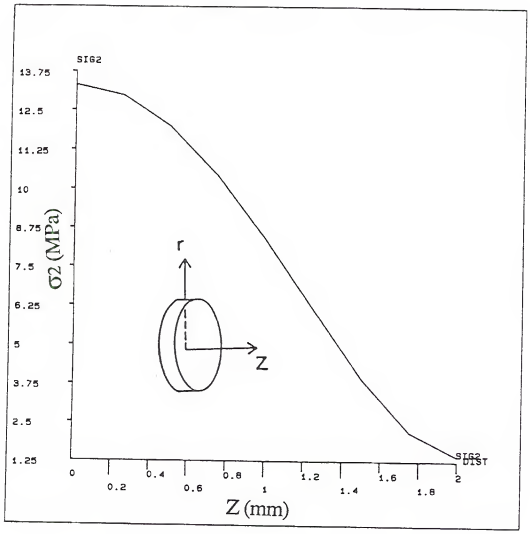

Fig. 4.61 Transient principal stress ($\sigma 2$ in MPa) produced at the edge of a 2-mm-thick disk ($\Delta\alpha = 0$) subjected to free convective cooling in air as a function of thickness ($T_i = 850°C$).

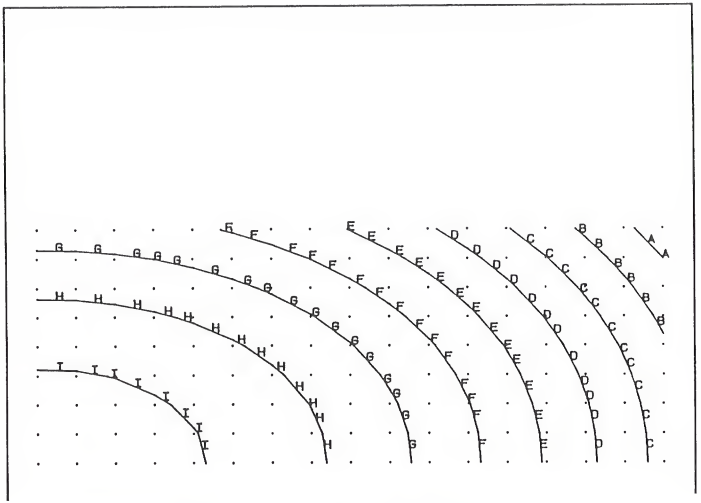

Fig. 4.62 Temperature distribution near T_g (600°C) for free convective cooling of a 6-mm-thick disk in air (T_i = 982°C).

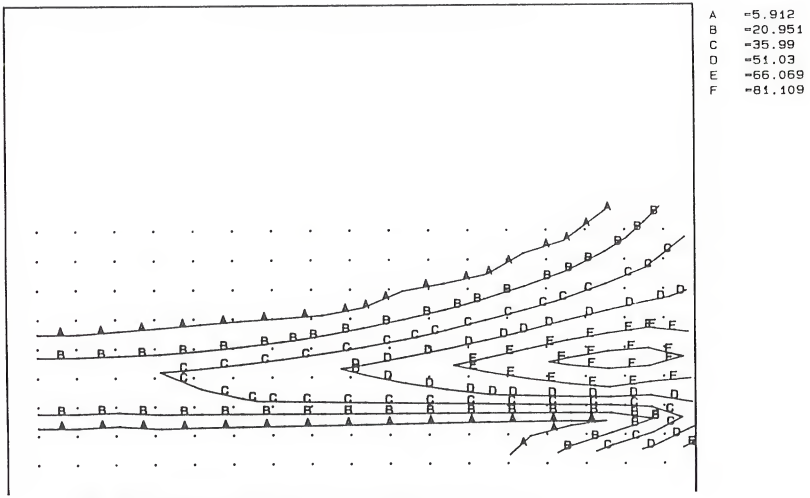

Fig. 4.63 Transient principal stress ($\sigma 1$ in MPa) produced within a 6-mm-thick disk ($\Delta\alpha = 3.2$ ppm/°C) subjected to free convective cooling in air ($T_i = 982$°C).

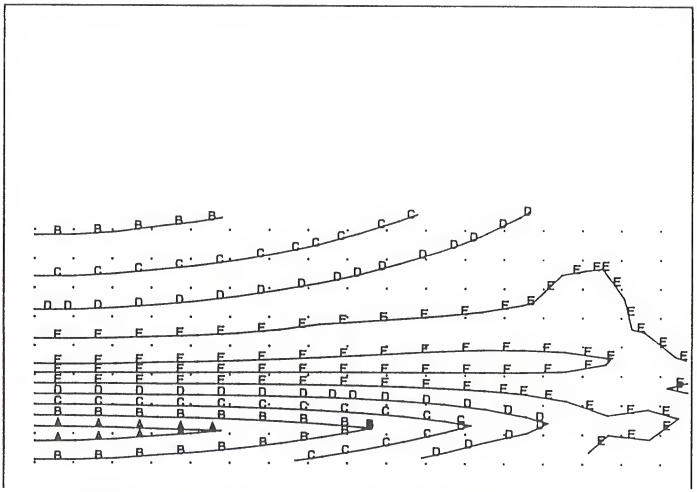

Fig. 4.64 Transient principal stress ($\sigma 2$ in MPa) produced within a 6-mm-thick disk ($\Delta\alpha = 3.2$ ppm/°C) subjected to free convective cooling in air ($T_i = 982$°C).

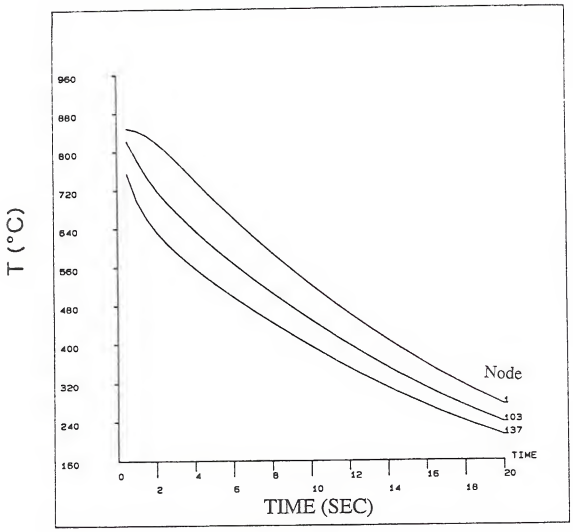

Fig. 4.65 Temperature versus time profiles for three selected nodes on the symmetrical axis in a 2-mm-thick disk subjected to tempering in air (T_i = 850°C).

experimental data and the analytical models (eqs. 57 and 35). The axisymmetric temperature distribution which occurred at 8 sec after the initiation of tempering, is shown in Fig. 4.66. A maximum temperature differential of 113°C, occurred near the center of the specimen. At this stage of tempering, a temperature differential of 302°C was produced between the hottest and the coldest point of the disk. Shown in Figs. 4.67-4.69 are the $\sigma 1$ and $\sigma 2$ values and the stress intensity contours (SI), respectively, for a tempered disk with a contraction mismatch level of 3.2 ppm/°C. Stress intensity is defined as twice the maximum shear stress (τ_{max}). The peak values of tensile stresses (Fig. 4.67) and stress intensity (Fig. 4.69) were 152.9 MPa and 163.8 MPa, respectively, which occurred at the edge of the disk (contour F). The peak value of compressive stress at the surface (Fig. 4.68) was 88.0 MPa. Comparison of these stresses with the corresponding values for the mismatch level of –1.5 ppm/°C (Fig. 4.70 through 4.72) indicates that the contours are different in shape and direction, however, their peak values are not significantly different. For instance, the largest $\sigma 1$ value for the +3.2 ppm/°C mismatch level was 153 MPa (Fig. 4.67) and the corresponding value for the –1.5 ppm/°C level was 152 MPa (Fig. 4.70). This indicates that in the tempered specimen the transient incompatibility stresses are dominated by the stresses developed because of the temperature gradient.

To determine the contribution of the temperature gradient to transient stresses, the principal stress contours were plotted (Figs. 4.73–4.76) for a tempered body porcelain disk with no contraction mismatch ($\Delta\alpha = 0.0$). Similar to the free convective cooling condition, the insulated boundary for the thermal analysis was treated as a symmetrical boundary for stress analysis. The peak value of the transient tensile stress ($\sigma 1$) was 142.4 MPa (Fig. 4.73) which occurred at the surface near the edge of the disk. This location was also associated with the largest

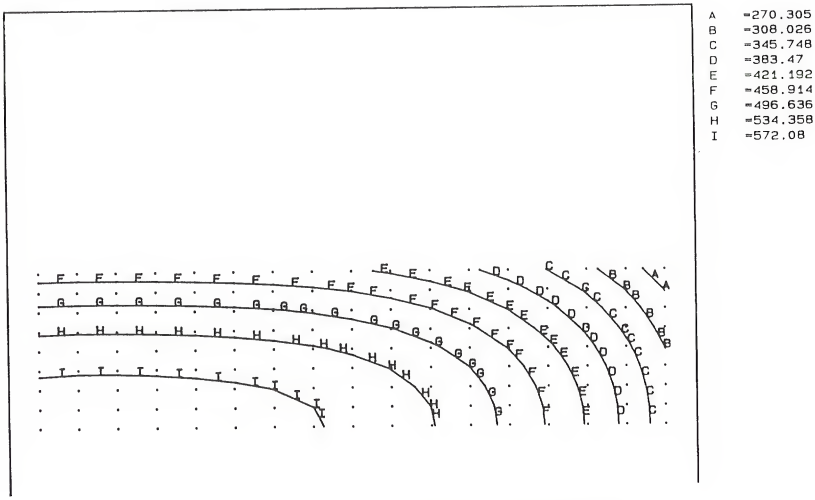

Fig. 4.66 Temperature distribution near T_g (600°C) in a 2-mm-thick disk subjected to tempering in air (T_i = 850°C).

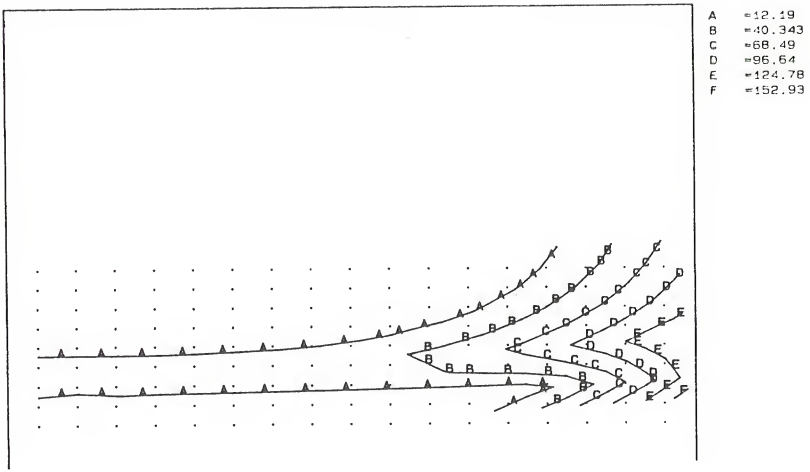

Fig. 4.67 Transient principal stress ($\sigma 1$ in MPa) produced within a 2-mm-thick disk ($\Delta\alpha$ = 3.2 ppm/°C) subjected to tempering in air (T_i = 850°C).

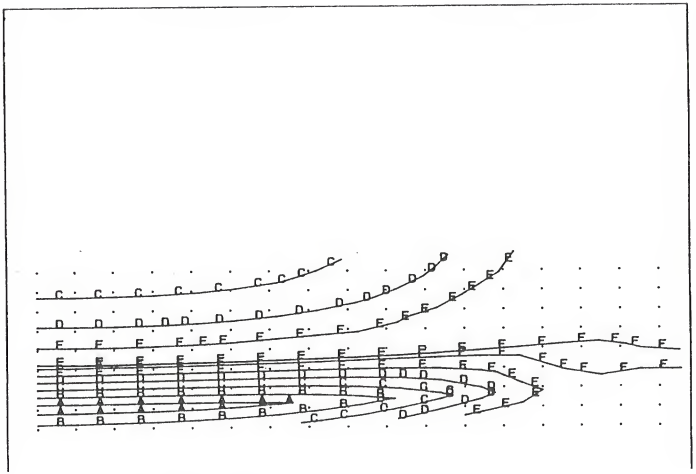

Fig. 4.68 Transient principal stress ($\sigma 2$ in MPa) produced within a 2-mm-thick disk ($\Delta\alpha$ = 3.2 ppm/°C) subjected to tempering in air (T_i = 850°C).

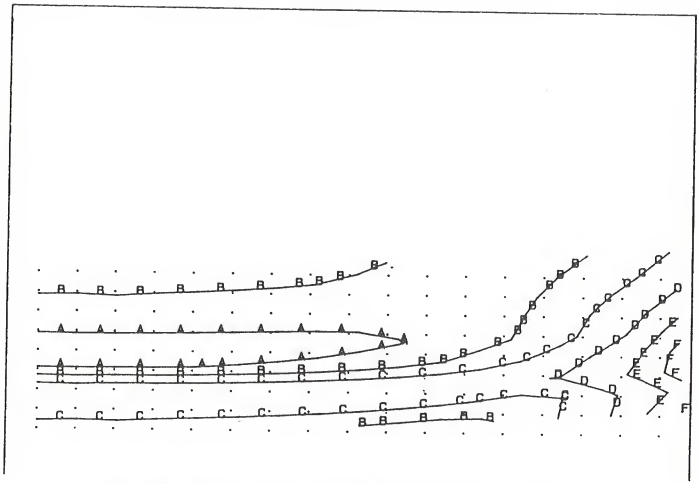

Fig. 4.69 Transient stress intensity (SI in MPa) produced within a 2-mm-thick disk ($\Delta\alpha = 3.2$ ppm/°C) subjected to tempering in air ($T_i = 850$°C).

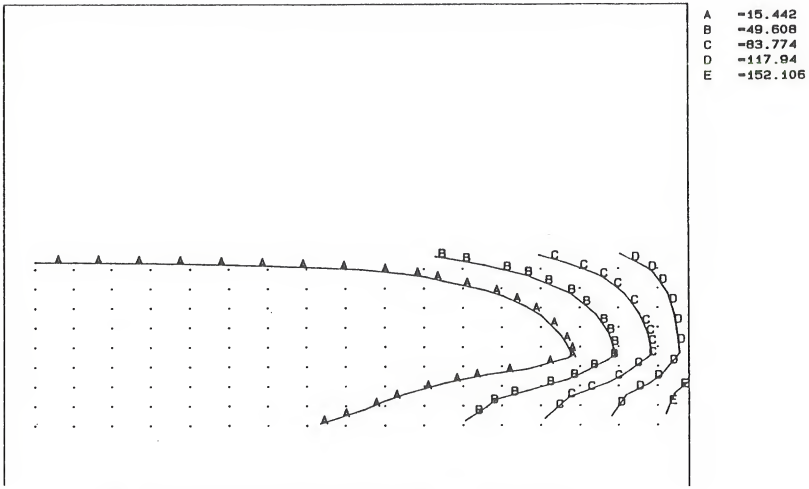

Fig. 4.70 Transient principal stress ($\sigma 1$ in MPa) produced within a 2-mm-thick disk ($\Delta\alpha = -1.5$ ppm/°C) subjected to tempering in air ($T_i = 850$°C).

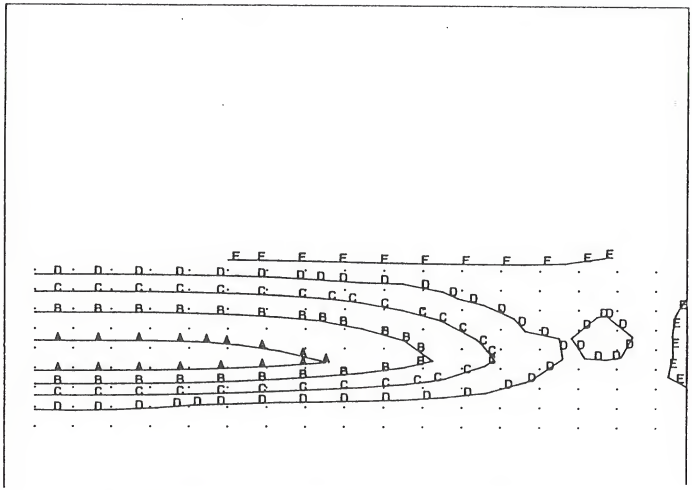

Fig. 4.71 Transient principal stress ($\sigma 2$ in MPa) produced within a 2-mm-thick disk ($\Delta\alpha = -1.5$ ppm/°C) subjected to tempering in air ($T_i = 850$°C).

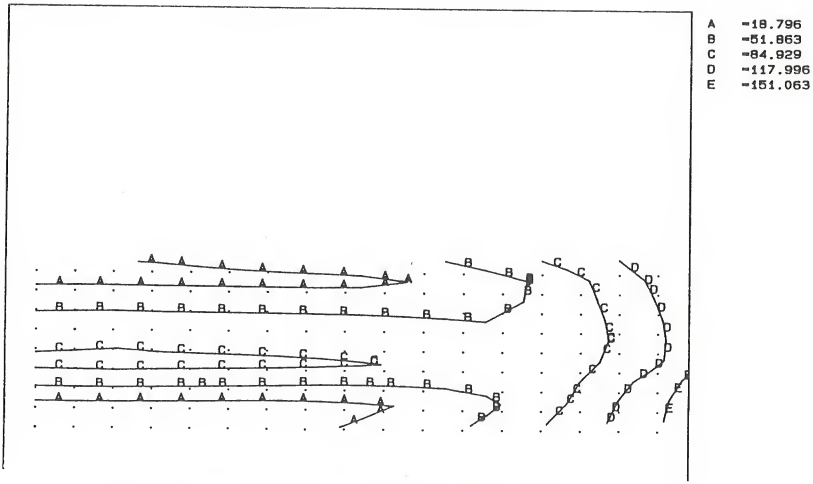

Fig. 4.72 Transient stress intensity (SI in MPa) produced within a 2-mm-thick disk ($\Delta\alpha = -1.5$ ppm/°C) subjected to tempering in air ($T_i = 850$°C).

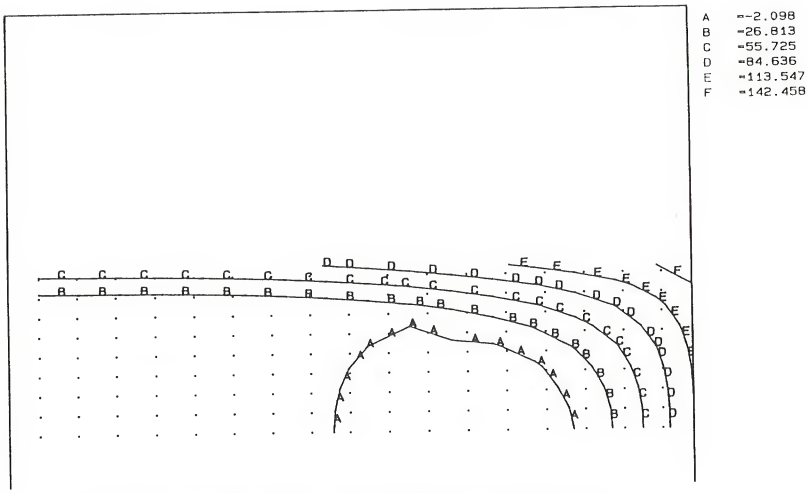

Fig. 4.73 Transient principal stress ($\sigma 1$ in MPa) produced within a 2-mm-thick disk ($\Delta\alpha = 0$) subjected to tempering in air ($T_i = 850°C$).

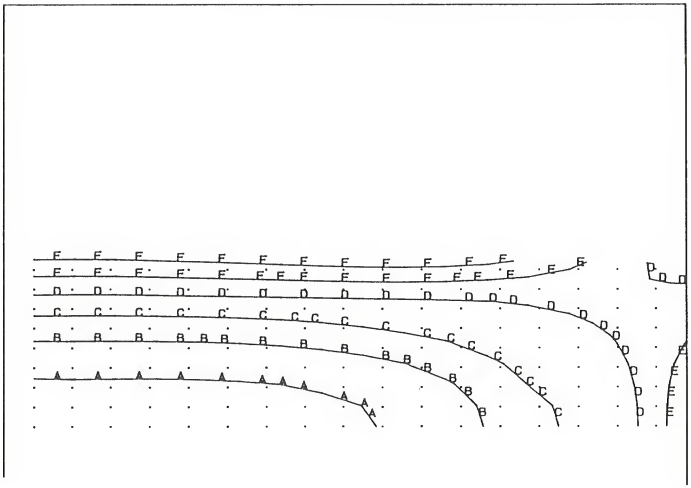

Fig. 4.74 Transient principal stress ($\sigma 2$ in MPa) produced within a 2-mm-thick disk ($\Delta\alpha = 0$) subjected to tempering in air ($T_i = 850°C$).

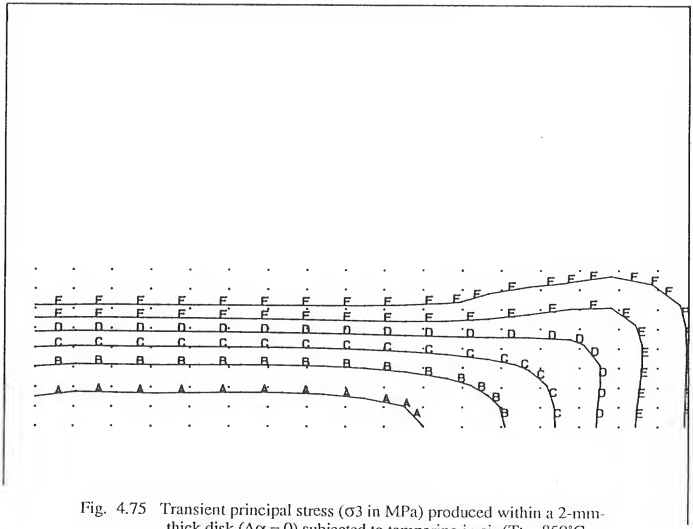

Fig. 4.75 Transient principal stress ($\sigma 3$ in MPa) produced within a 2-mm-thick disk ($\Delta\alpha = 0$) subjected to tempering in air ($T_i = 850°C$

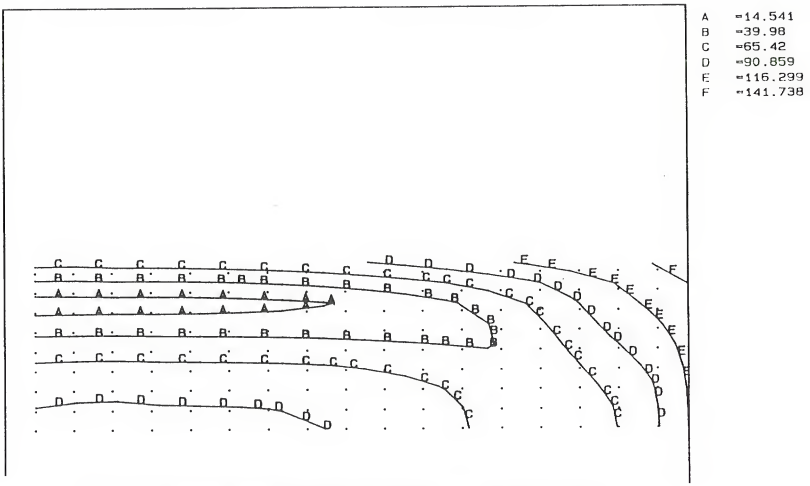

Fig. 4.76 Transient stress intensity (SI in MPa) produced within a 2-mm-thick disk ($\Delta\alpha = 0$) subjected to tempering in air ($T_i = 850°C$).

stress intensity value of 141.7 MPa (Fig. 4.76). The stress contours were along the same directions as the temperature contours (Fig. 4.66) The locations of maximum σ_2 and σ_3 gradients (Figs. 4.74, 4.75) were associated with the regions of the largest temperature gradient. Shown in Fig. 4.77 and 4.78 are the distribution of σ_1 and σ_2 at the surface as a function of the disk radius. Similar to the free convection case, the σ_1 stress has a parabolic shape with a minimum value of 72 MPa at the center and maximum value of 155 MPa at the edge of the disk (Fig. 4.77). The largest σ_2 value was 84 MPa which occurred at a radius of 4.4 mm. The regions with a larger radius are influenced by the heat loss from the side and are associated with a smaller temperature gradient. Therefore, the principal compressive stresses (σ_2) at the surface for free convective cooling (Fig. 4.59) and tempering (Fig. 4.78), which is more influenced by temperature gradient, decreases toward the edge of the disk. Shown in Figs. 4.79 and 4.80 are the principal stresses (σ_1 and σ_2) at the edge of the disk as a function of distance from the insulated (bottom) surface. These stresses are also parabolic in shape. However, at the surface where σ_1 has a maximum of 156 MPa (Fig. 4.79), σ_2 has a minimum of 8 MPa (Fig. 4.80). The minimum and maximum values of σ_1 and σ_2 which occurred at the bottom surface were 116 MPa and 71 MPa, respectively.

Shown in Fig. 4.81 are the temperature contours near the T_g value of 600°C for a 2-mm-thick body porcelain disk ($\Delta\alpha = 0$) quenched from an initial temperature of 850°C in silicone oil at a temperature of 100°C. Since the disk was subjected to uniform cooling, the temperature distribution is symmetrical along a horizontal plane which passes through the half-thickness of the disk. This plane is referred to as midplane of the disk. Shown in Fig. 4.82 is a vector plot of the thermal fluxes which represent the magnitude and direction of the heat loss at each location. Shown in Figs. 4.83–4.85 are the principal stresses (σ_1 and σ_2) and

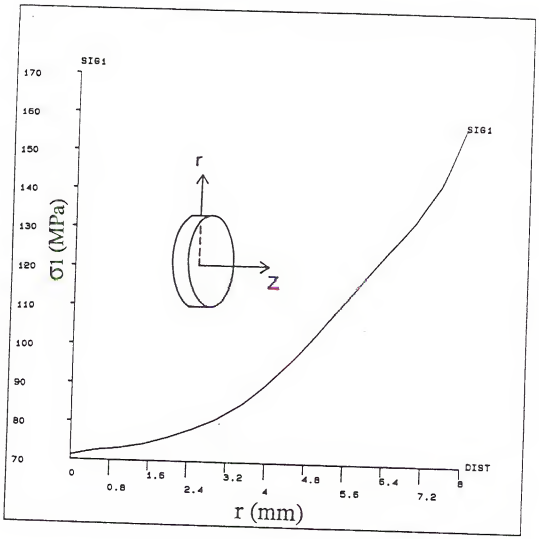

Fig. 4.77 Transient principal stress ($\sigma 1$ in MPa) at the surface of a 2-mm-thick disk ($\Delta\alpha = 0$) subjected to tempering in air ($T_i = 850°C$) as a function of radius.

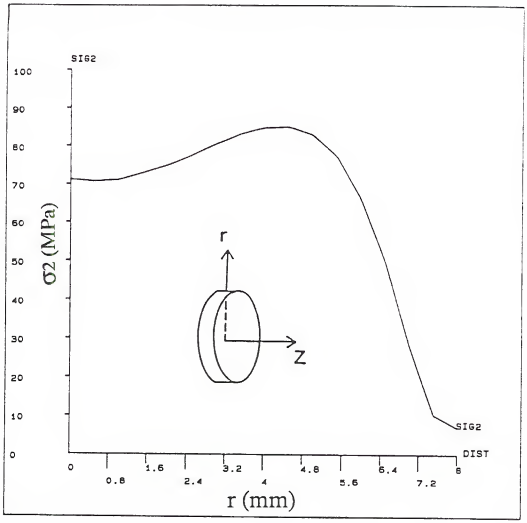

g. 4.78 Transient principal stress (σ2 in MPa) at the surface of a 2-mm-thick disk ($\Delta\alpha = 0$) subjected to tempering in air ($T_i = 850°C$) as a function of radius.

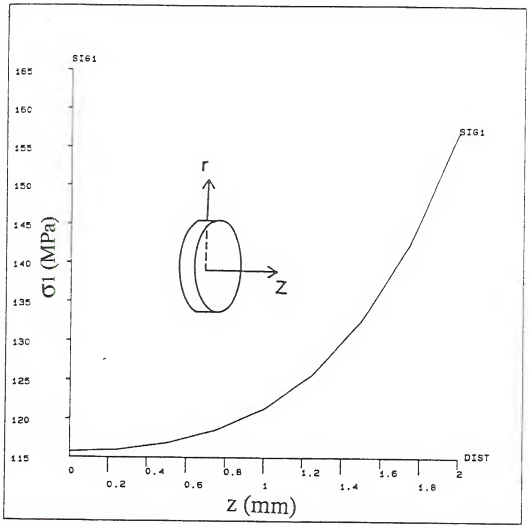

Fig. 4.79 Transient principal stress ($\sigma 1$ in MPa) at the edge of a 2-mm-thick disk ($\Delta\alpha = 0$) subjected to tempering in air ($T_i = 850°C$) as a function of thickness.

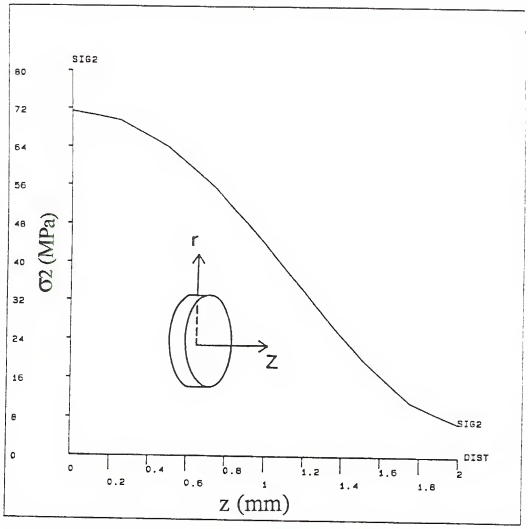

Fig. 4.80 Transient principal stress ($\sigma 2$ in MPa) at the edge of a 2-mm-thick disk ($\Delta\alpha = 0$) subjected to tempering in air ($T_i = 850°C$) as a function of thickness.

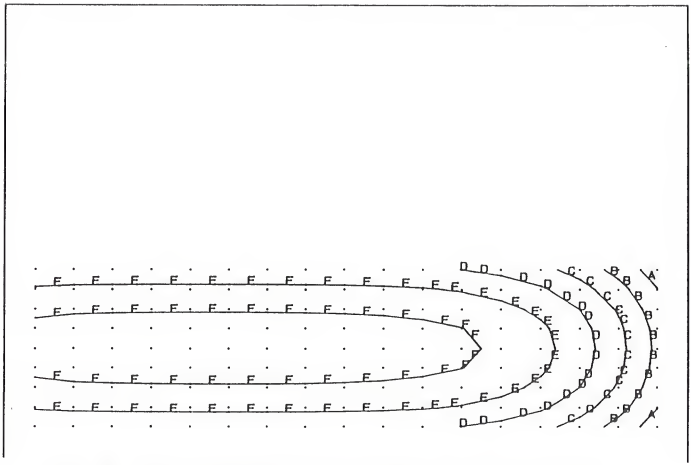

Fig. 4.81 Temperature distribution near T_g (600°C) for a 2-mm-thick body porcelain disk ($\Delta\alpha = 0$) quenched from an initial temperature of 850°C in silicone oil at a temperature of 100°C.

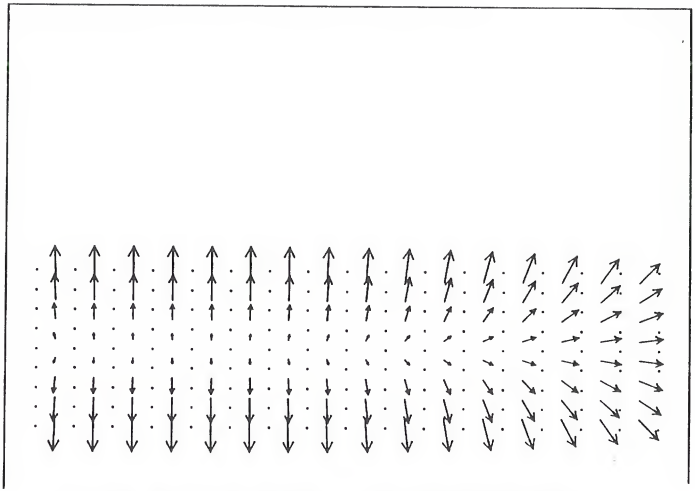

Fig. 4.82 Vector plot of thermal fluxes for a 2-mm-thick body porcelain disk ($\Delta\alpha = 0$) quenched from an initial temperature of 850°C in silicone oil at a temperature of 100°C.

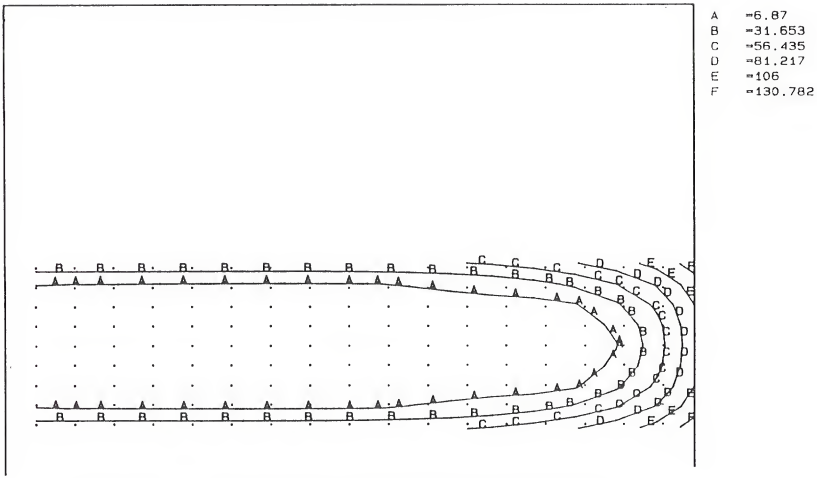

Fig. 4.83 Transient principal stress ($\sigma 1$ in MPa) within a 2-mm-thick disk ($\Delta\alpha = 0$) quenched from an initial temperature of 850°C in silicone oil at a temperature of 100°C.

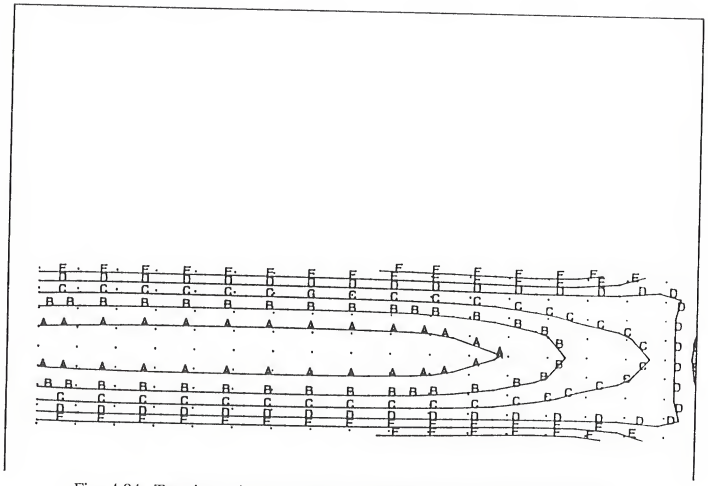

Fig. 4.84 Transient principal stress ($\sigma 2$ in MPa) within a 2-mm-thick disk ($\Delta\alpha = 0$) quenched from an initial temperature of 850°C in silicone oil at a temperature of 100°C.

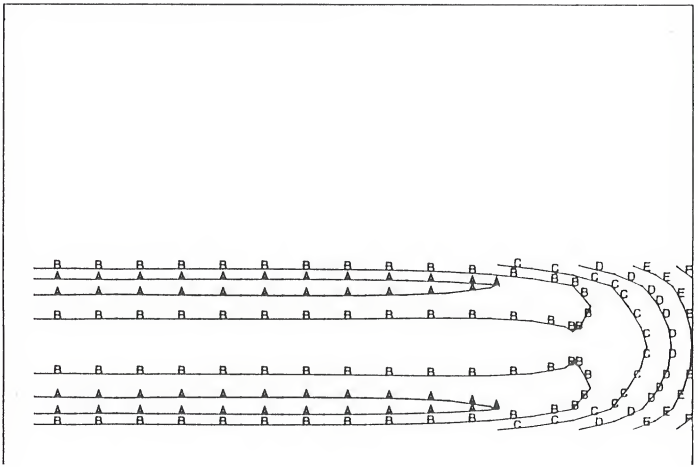

Fig. 4.85 Transient stress intensity (SI in MPa) within a 2-mm-thick disk ($\Delta\alpha = 0$) quenched from an initial temperature of 850°C in silicone oil at a temperature of 100°C.

stress intensity (SI) contours for this cooling condition. These stresses are parabolic in shape and similar to the the temperature contours, are symmetrical along the midplane of the disk. The peak values of $\sigma 1$ and SI stresses were 130.8 MPa (Fig. 4.83) and 127.7 MPa (Fig. 4.85), respectively, which occurred at the edge of the disk. The maximum $\sigma 2$ value was 49.8 MPa (Fig. 4.84) which was tensile in nature and occurred at the surface. Shown in Figs. 4.86 through 4.88 are the transient stresses produced at the surface as a function of radius. The magnitude of stresses, $\sigma 1$ (Fig. 4.86) and SI (Fig. 4.88) increased with an increase in radius and the largest values occurred at the edge of the disk. However, the largest value of $\sigma 2$ occurred at a radius of 6.2 mm. Shown in Figs. 4.89 through 4.91 are the transient stresses developed at the edge of the disk as a function of distance from the bottom surface. These stresses which are produced because of the temperature gradients in the absence of incompatibility stresses, are parabolic in shape and are symmetrical with respect to the midplane of the disk.

The minimum values of stresses, $\sigma 1$ and SI were 103.0 MPa (Fig. 4.89) and 110.0 MPa (Fig. 4.91), respectively. The maximum value of $\sigma 2$ stress was 39.0 MPa which occurred at the midplane of the disk.

B. Static Analysis of Dental Ceramic Crowns

The maximum tensile stress contours for a ceramic thickness of 0.5 mm (case I design) due to vertically and horizontally applied loads are shown in Figs. 4.92 and 4.93, respectively. The largest principal tensile stresses induced in ceramic due to a distributed load of 600 N applied in a cuspal region were 11.4 MPa and 171.9 MPa for vertical and horizontal loading orientations, respectively. Stresses which developed in the facial and lingual margins were primarily

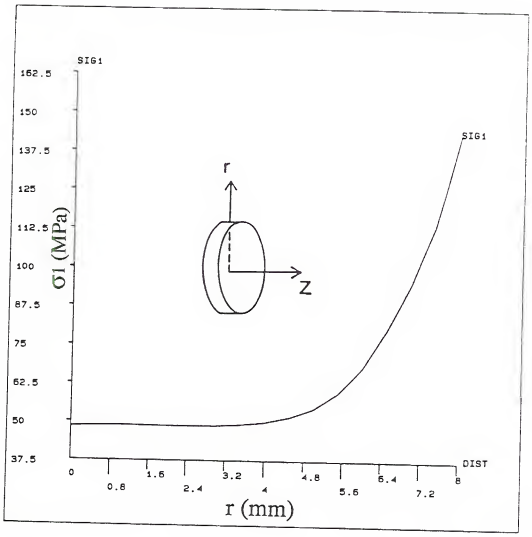

Fig. 4.86 Transient principal stress ($\sigma 1$ in MPa) at the surface a 2-mm-thick disk ($\Delta\alpha = 0$) quenched in silicone oil as a function of radius.

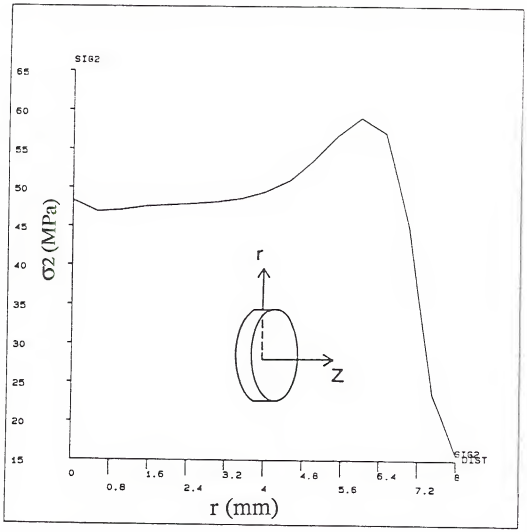

Fig. 4.87 Transient principal stress ($\sigma 2$ in MPa) at the surface a 2-mm-thick disk ($\Delta\alpha = 0$) quenched in silicone oil as a function of radius.

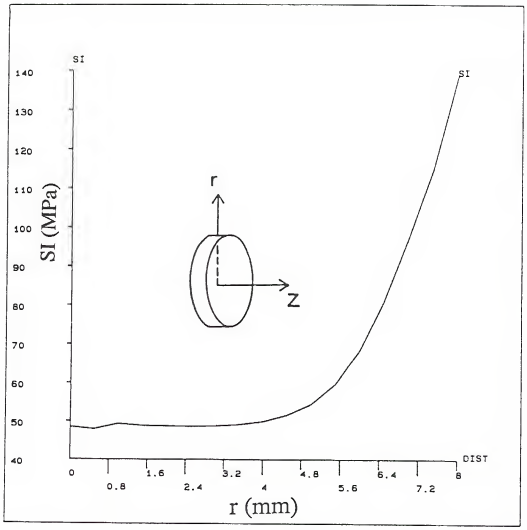

Fig. 4.88 Transient stress intensity (SI in MPa) at the surface a 2-mm-thick disk ($\Delta\alpha = 0$) quenched in silicone oil as a function of radius.

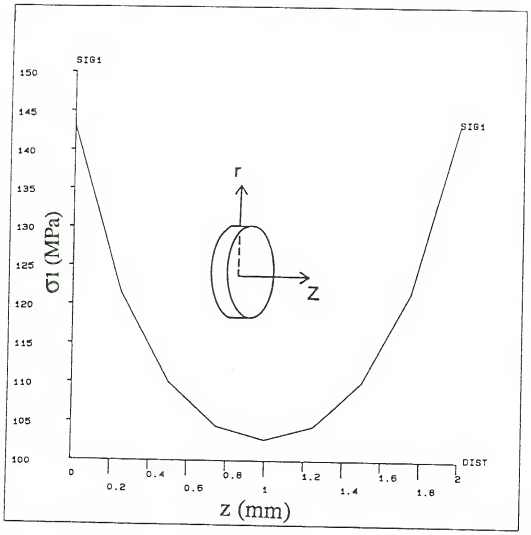

Fig. 4.89 Transient principal stress ($\sigma 1$ in MPa) at the edge of a 2-mm-thick disk ($\Delta\alpha = 0$) quenched in silicone oil as a function of thickness.

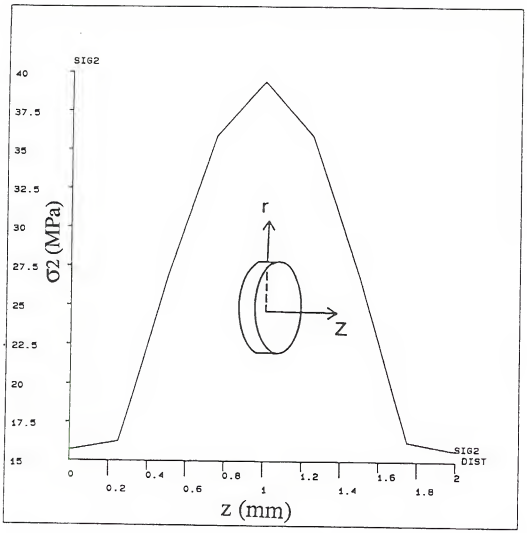

Fig. 4.90 Transient principal stress ($\sigma 2$ in MPa) at the edge of a 2-mm-thick disk ($\Delta\alpha = 0$) quenched in silicone oil as a function of thickness.

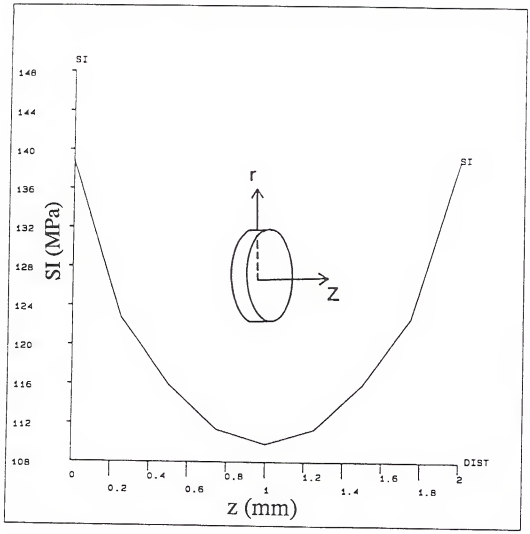

Fig. 4.91 Transient stress intensity (SI in MPa) at the edge of a 2-mm-thick disk ($\Delta\alpha = 0$) quenched in silicone oil as a function of thickness.

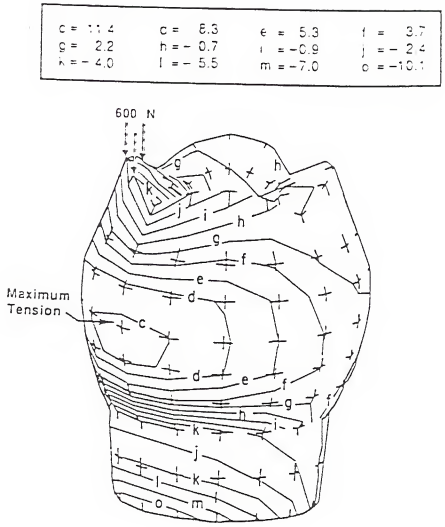

Fig. 4.92 Principal stress contours ($\sigma 1$ in MPa) in a ceramic dental crown due to vertically applied loads.

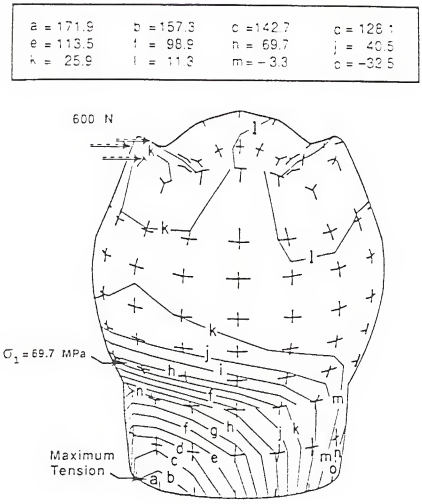

Fig. 4.93 Principal stress contours (σ1 in MPa) in a ceramic dental crown due to horizontally oriented loads.

compressive under vertical loads. However, tensile stresses developed when the load was applied horizontally. The stress distributions within the crowns three occlusal thicknesses were different only near the site of loading. Shown in Figs. 4.94 and 4.95 are the principal compressive and maximum shear stress contours due to a horizontally oriented load of 600 N. The result of this study showed that the variation of occlusal thickness of ceramic between 0.5 mm and 3.0 mm has only a minimal effect on the induced tensile stress state. The three-dimensional model also showed that the dominant factor in development of tensile stress at the surface of dental ceramic is the orientation of applied forces. The influence of these stresses in crack development and growth can be reduced by thermal tempering.

C. Transient Stress Analysis of Dental Ceramic Crowns

Shown in Fig. 4.96 is the vector plot of thermal fluxes for free convective cooling (h=70 $W/m^2 \cdot K$) of the ceramic crown from an initial temperature of 850°C. The crown was assumed to be completely insulated from the inner surface. The temperature versus time profiles for the inner and outer surfaces near the cuspal regions are shown in Fig. 4.97. The thermal contours near an assumed glass transition temperature of 600°C are shown in Fig. 4.98. This temperature distribution occurred 12.5 sec after initiation of the free convective cooling. Although the crown is initially subjected to uniform cooling, because of the variation in thickness and surface area there is a temperature gradient from cuspal to marginal regions. When the temperature at the cuspal region was approximately 600°C (contour I), the temperature at the margin was 543.3°C (contour A). Shown in Figs. 4.99 and 4.100 are the corresponding principal

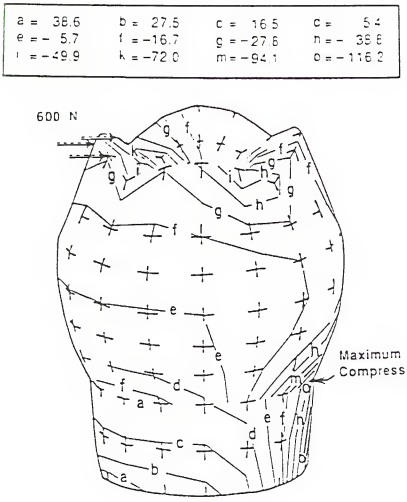

Fig. 4.94 Principal stress contours ($\sigma 2$ in MPa) in a ceramic dental crown due to horizontally oriented loads.

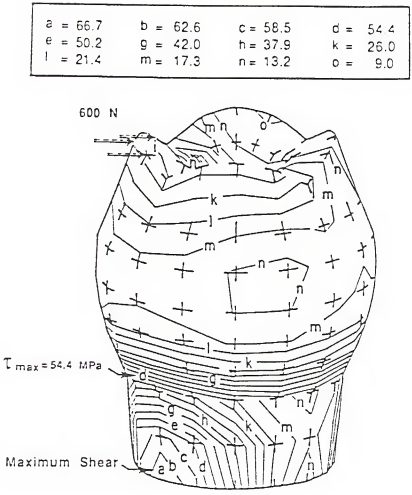

Fig. 4.95 Maximum shear stress contours (τmax in MPa) in a ceramic dental crown due to horizontally oriented loads.

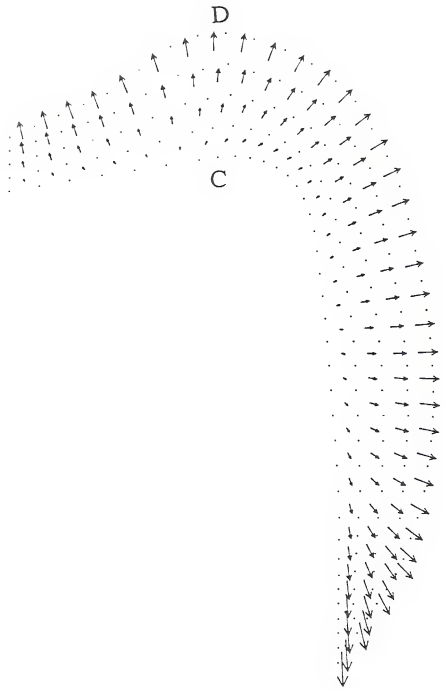

Fig. 4.96 Vector plot of thermal fluxes for a bilayered dental ceramic crown subjected to free convective cooling.

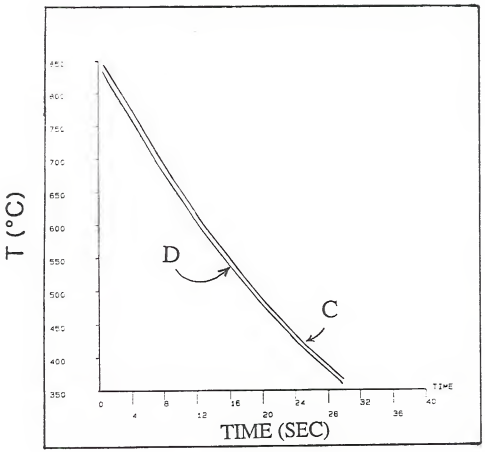

Fig. 4.97 Temperature versus time profiles at the inner and outer surfaces of the bilayered ceramic molar crown ($\Delta\alpha = +3.2$ ppm/°C) subjected to free cooling from an initial temperature of 850°C.

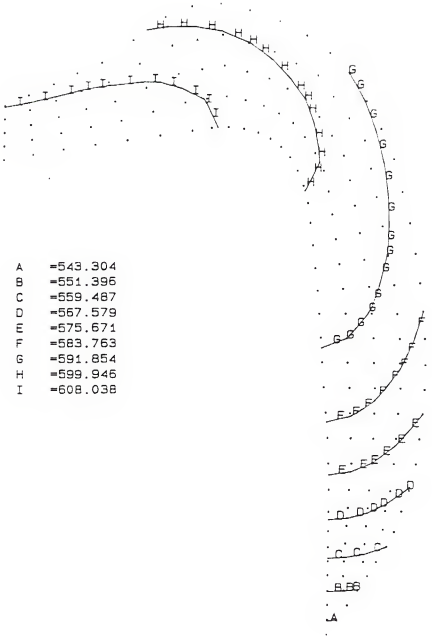

Fig. 4.98 Temperature contours (°C) near the glass transition temperature of 600°C in a bilayered ceramic molar crown ($\Delta\alpha$ = + 3.2 ppm/°C) subjected to free convective cooling.

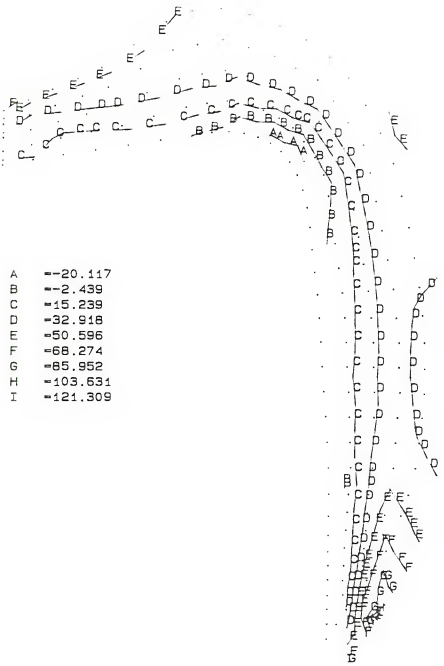

Fig. 4.99 Transient stress contours ($\sigma 1$ in MPa) in a bilayered ceramic molar crown ($\Delta\alpha = +3.2$ ppm/°C) subjected to free convective cooling from an initial temperature of 850°C.

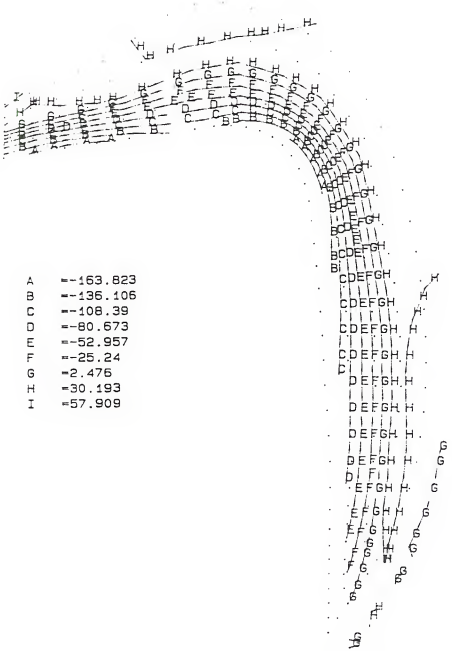

Fig. 4.100 Transient stress contours ($\sigma 2$ in MPa) in a bilayered ceramic molar crown ($\Delta\alpha = +3.2$ ppm/°C) subjected to free convective cooling from an initial temperature of 850°C.

tensile ($\sigma 1$) and compressive ($\sigma 2$) transient stresses induced within a ceramic crown with a thermal contraction mismatch of 3.2 ppm/°C. The maximum tensile and compressive were 121.3 MPa and 163.8 MPa, respectively, at the margins and near the occlusal region respectively. Fig. 4.101 shows the contours corresponding to a horizontal displacement. The maximum displacement (0.023 mm) occurred at the margin which had the largest distance from the fixed node located at the symmetric axis (node A in Fig. 3.9).

The temperature versus time profiles at the inner and outer surfaces of a ceramic crown near the cuspal regions are shown in Fig. 4.102. The crown was subjected to thermal tempering ($h = 560\ W/m^2{\cdot}K$) from an initial temperature of 850°C. The temperature of entire crown reached the ambient temperature of 30°C, approximately after 20 sec. Shown in Fig. 4.103 is the temperature contours near the glass transition temperature of 600°C. At 5 sec after initiation of cooling, the difference between the temperature at the cuspal and marginal regions was approximately 238°C. The transient principal stresses induced in the crown because of the thermal contraction mismatch of +3.2 ppm/°C and due to the temperature gradients produced by tempering treatment are shown in Figs. 4.104, 4.105 and 4.106. The maximum principal tensile stress ($\sigma 1$) value was 178.1 MPa (Fig. 4.104) which occurred at the marginal region. The maximum values of $\sigma 2$ and $\sigma 3$ were 183.2 MPa and 218.8 MPa, respectively, which were compressive in nature and occurred near the occlusal regions. Shown in Fig. 4.107 are the contours corresponding to the displacements along the horizontal direction.

To determine the influence of the initial tempering temperature on the magnitude of principal stresses, the transient stresses were also calculated for an initial tempering temperature of 750°C. Shown in Fig. 4.108 is the temperature

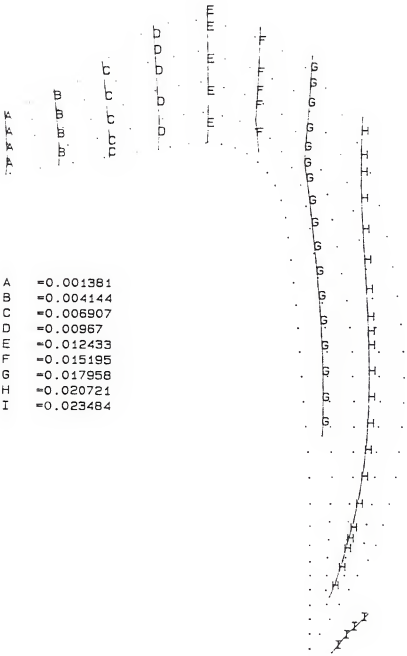

Fig. 4.101 Displacement contours (mm) along horizontal direction in a bilayered ceramic molar crown ($\Delta\alpha = +3.2$ ppm/°C) subjected to free convective cooling from an initial temperature of 850°C.

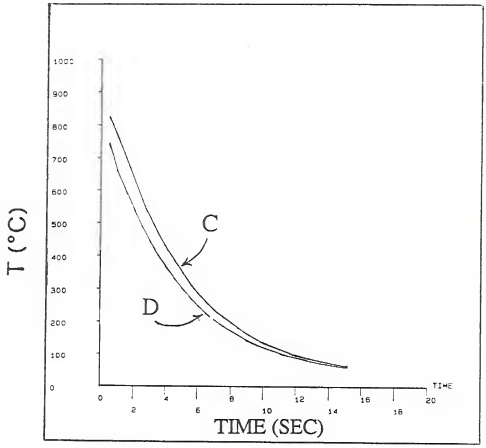

Fig. 4.102 Temperature versus time profiles for the inner and outer surfaces of the bilayered ceramic molar crown ($\Delta\alpha = +3.2$ ppm/°C) subjected to tempering from an initial temperature of 850°C.

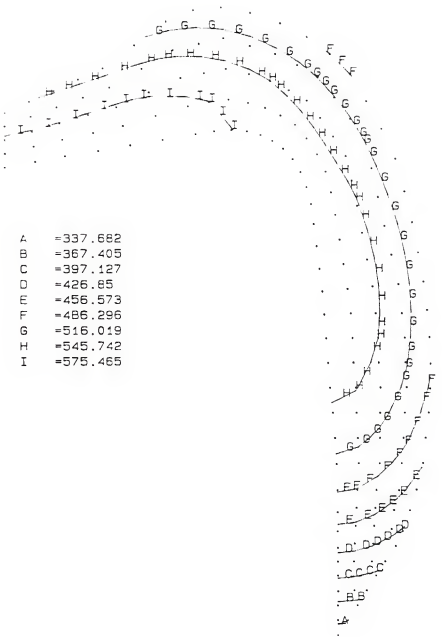

Fig. 4.103 Temperature contours (°C) near the glass transition temperature of 600°C for a bilayered ceramic crown tempered from an initial temperature of 850°C.

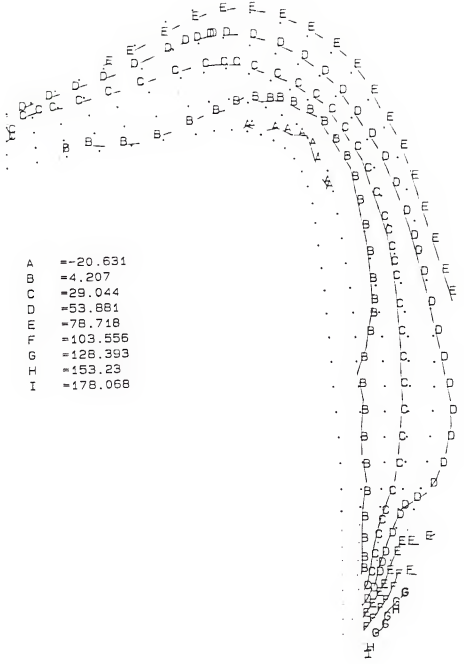

Fig. 4.104 Transient stress contours (σ_1 in MPa) in a bilayered ceramic molar crown ($\Delta\alpha$ = + 3.2 ppm/°C) tempered from an initial temperature of 850°C.

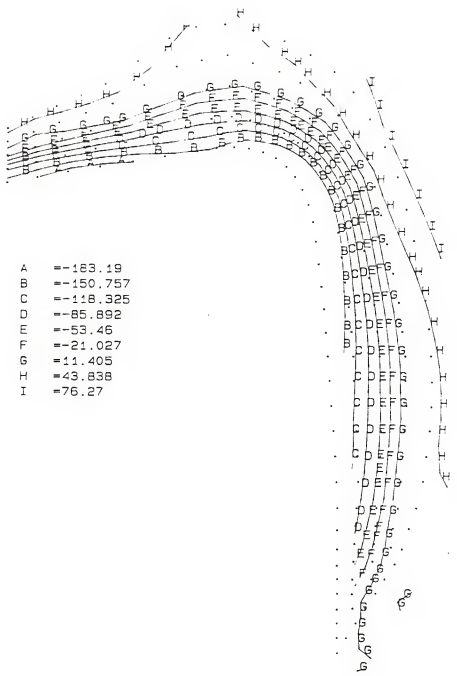

Fig. 4.105 Transient stress contours (σ_2 in MPa) in a bilayered ceramic molar crown ($\Delta\alpha$ = + 3.2 ppm/°C) tempered from an initial temperature of 850°C.

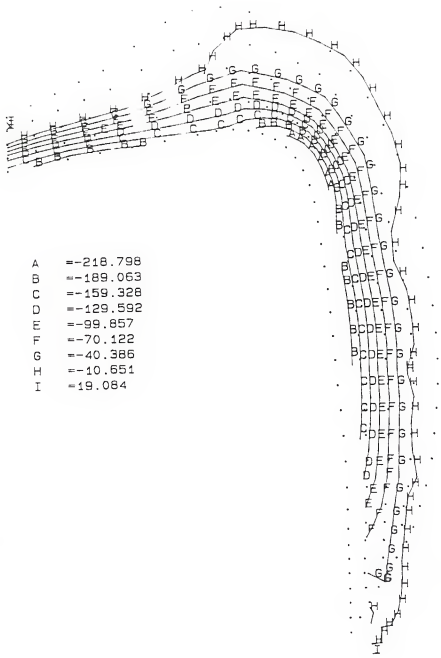

Fig. 4.106 Transient stress contours (σ_3 in MPa) in a bilayered ceramic molar crown ($\Delta\alpha$ = + 3.2 ppm/°C) tempered from an initial temperature of 850°C.

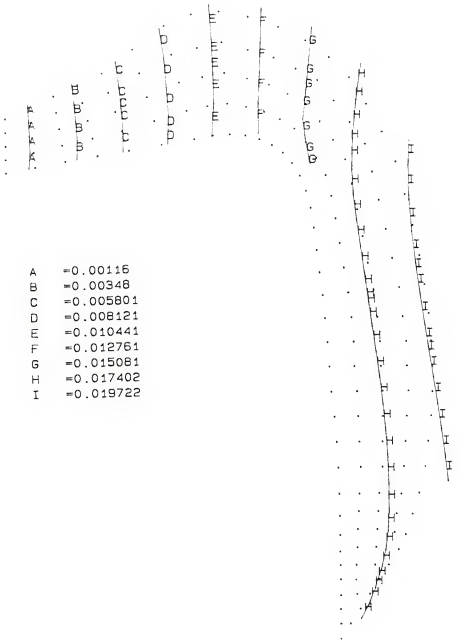

Fig. 4.107 Displacement contours (mm) along horizontal direction for a bilayered ceramic crown ($\Delta\alpha = +3.2$ ppm/°C) tempered from an initial temperature of 850°C.

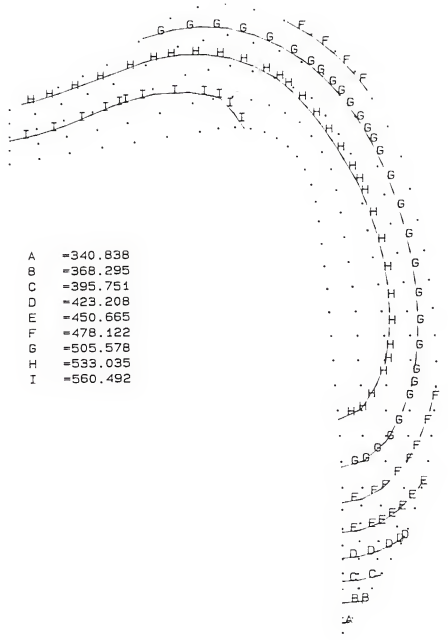

Fig. 4.108 Temperature contours (°C) near the glass transition temperature of 600°C for a ceramic crown tempered from an initial temperature of 750°C.

gradient near the glass transition temperature which occurred 2 sec after initiation of tempering. Since the temperatures were nearly similar to the values corresponding to an initial temperature of 850°C (Fig. 4.104), the stress distributions for these two cases were also similar. Shown in Figs. 4.109 through 4.112 are the stress and displacement contours for an initial tempering temperature of 750°C. Comparison of these figures with the corresponding figures for an initial temperature of 850°C indicates that the reduction of initial tempering temperature from 850°C to 750°C does not cause a significant difference in the magnitude of stresses.

These results show that, for a ceramic crown with a relatively large thermal contraction differential of 3.2 ppm/°C, the thermal tempering treatment produces relatively large transient tensile stresses. However, transient tensile stresses above the strength of dental ceramic were also developed under free convective cooling (Figs. 4.99 and 4.100). Therefore, for the conditions assumed in this analysis, failure due to incompatibility stresses will probably occur even for the conventional cooling of a crown with this level of thermal contraction mismatch. It is important to emphasize that the transient stresses were calculated for an assumed glass transition temperature of 600°C. However, the transition of dental porcelain from a liquid to a solid state occurs over a temperature range and not at a fixed temperature. So, to determine the influence of glass transition temperature on the magnitude of stresses, the transient stresses were also calculated for an assumed glass transition temperature (T_g) of 400°C. This is the same T_g value which was used in the study by DeHoff and Anusavice [66]. Shown in Fig. 4.113 are the temperature distributions near the glass transition temperature of 400°C within a crown tempered from an initial temperature of 850°C. This temperature distribution corresponds to a time of 4.5 sec after the

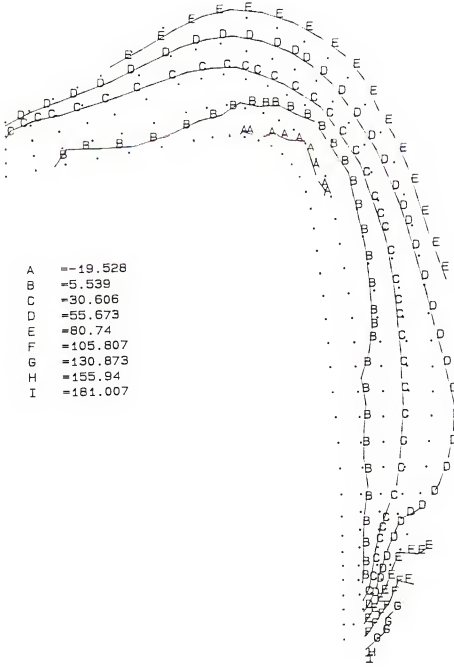

Fig. 4.109 Transient stress contours (σ_1 in MPa) in a bilayered ceramic molar crown ($\Delta\alpha$ = + 3.2 ppm/°C) tempered from an initial temperature of 750°C.

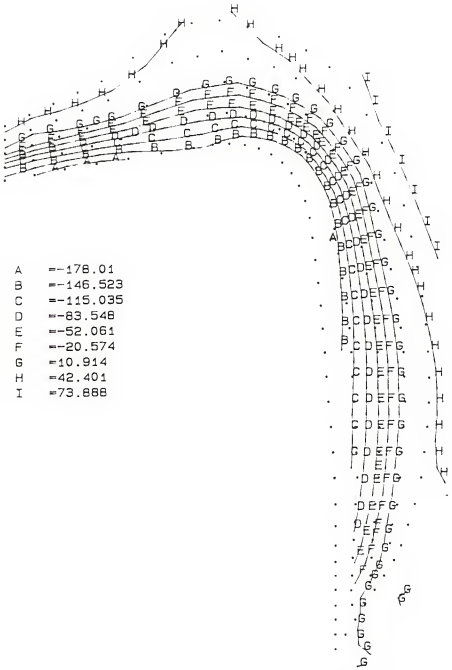

Fig. 4.110 Transient stress contours (σ_2 in MPa) in a bilayered ceramic molar crown ($\Delta\alpha = +3.2$ ppm/°C) tempered from an initial temperature of 750°C.

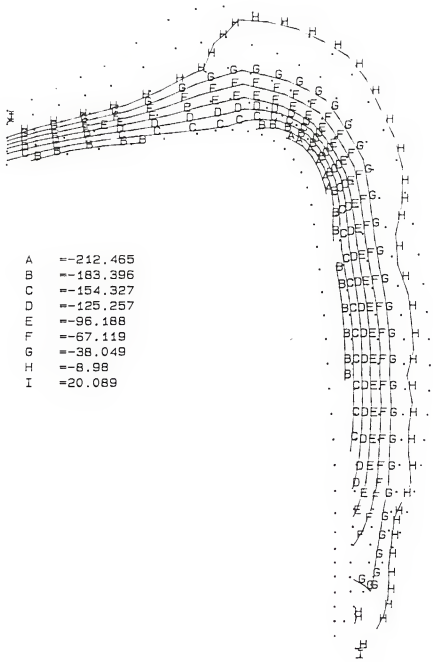

Fig. 4.111 Transient stress contours (σ_3 in MPa) in a bilayered ceramic molar crown ($\Delta\alpha$ = + 3.2 ppm/°C) tempered from an initial temperature of 750°C.

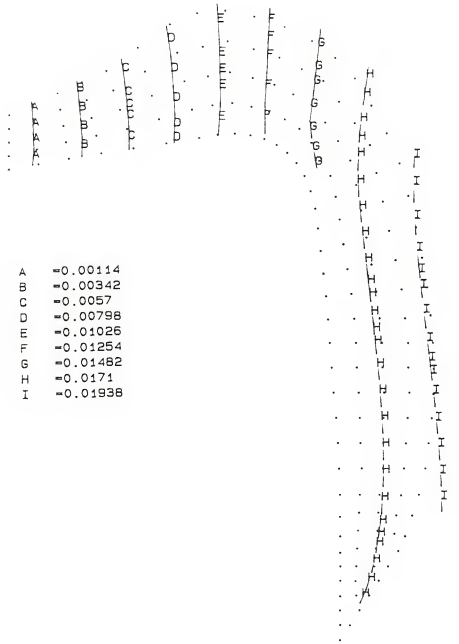

Fig. 4.112 Displacement contours (mm) along horizontal direction in a bilayered ceramic crown molar crown ($\Delta\alpha = +3.2$ ppm/°C) tempered from an initial temperature of 750°C.

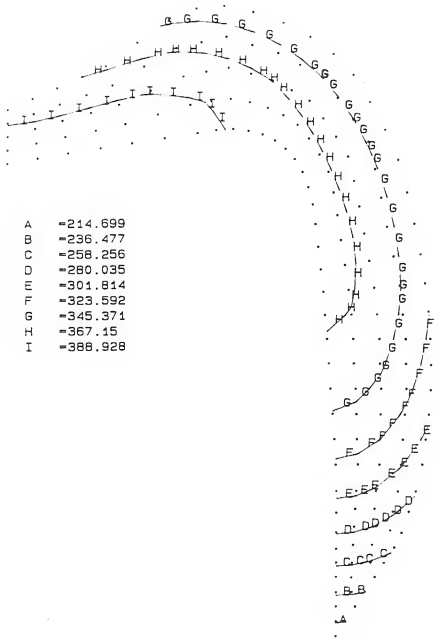

Fig. 4.113 Temperature contours (°C) near the glass transition temperature of 400°C for a ceramic molar crown tempered from an initial temperature of 850°C.

initial tempering. Under this assumption, a smaller temperature gradient is produced within the ceramic which results in smaller transient stresses. Shown in Figs. 4.114 through 4.116 are the principal stresses induced within ceramic with the thermal contraction mismatch level of +3.2 ppm/°C. The maximum tensile stress at the margin was reduced to 105.2 MPa (Fig.4.114). The maximum values of $\sigma 2$ and $\sigma 3$ stresses were 125.4 MPa (Fig. 4.115) and 149.5 MPa (Fig. 4.116), respectively.

To determine the contribution of the temperature gradient produced because of tempering treatment to transient stresses, the principal stress (Fig. 4.117 through 4.119) and stress intensity (Fig. 4.120) contours were plotted for a tempered crown with no contraction mismatch. For an assumed glass transition temperature of 600°C, the peak values of $\sigma 1$ and $\sigma 2$ and $\sigma 3$ were 86.6 MPa (Fig. 4.117), 43.5 MPa (Fig. 4.118) and 47.2 MPa (Fig. 4.119), respectively. The peak value of the stress intensity (SI) was 71.2 MPa (Fig. 4.120). When the temperature distributions near an assumed glass transition temperature of 400°C was used (Fig. 4.113), because of smaller temperature gradient the transient stresses were reduced significantly. Shown in Figs. 4.121 through 4.124 are the stress distributions within a single-layered ceramic crown for this condition. The peak value of $\sigma 1$, $\sigma 2$, $\sigma 3$ and SI stresses were 48.5 MPa (Fig. 4.121), 29.6 MPa (Fig. 4.122), 34.6 MPa (Fig.4.123) and 40.1 MPa (Fig. 4.124), respectively. These results show the glass transition temperature has a significant influence on the magnitude of transient stresses produced within a ceramic crown during tempering treatment.

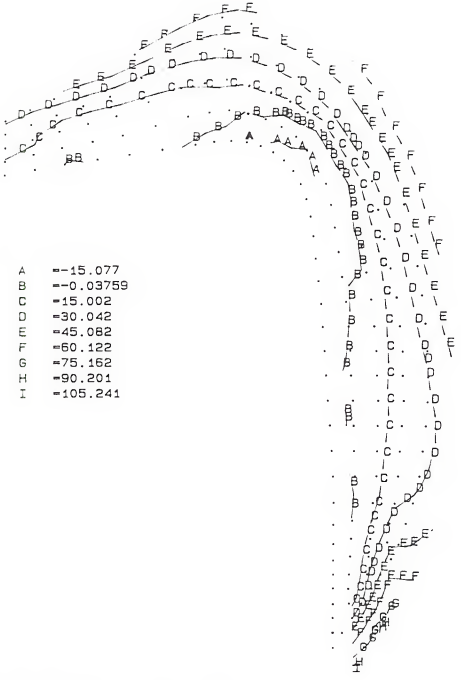

Fig. 4.114 Transient stress contours (σ_1 in MPa) in a bilayered ceramic molar crown ($\Delta\alpha$ = + 3.2 ppm/°C) tempered from an initial temperature of 850°C assuming a glass transition temperature of 400°C.

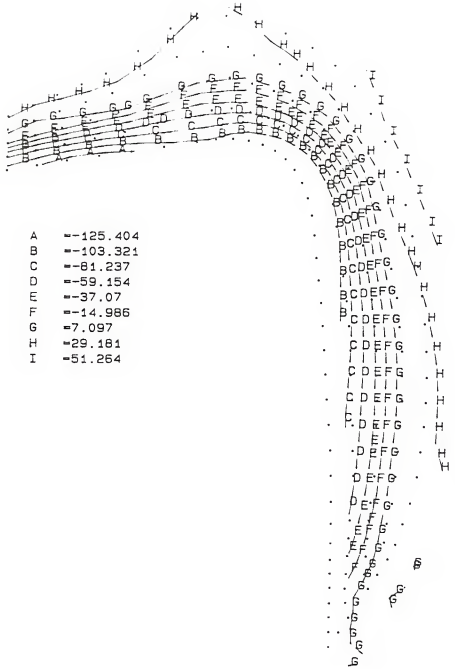

Fig. 4.115 Transient stress contours (σ_2 in MPa) in a bilayered ceramic molar crown ($\Delta\alpha = +3.2$ ppm/°C) tempered from an initial temperature of 850°C assuming a glass transition temperature of 400°C.

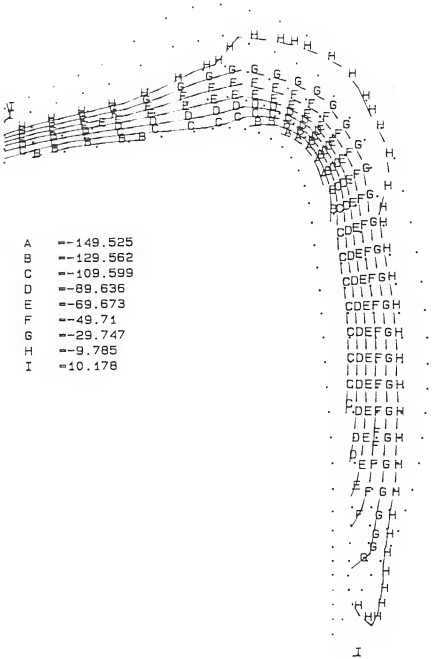

Fig. 4.116 Transient stress contours (σ_3 in MPa) in a bilayered ceramic molar crown ($\Delta\alpha = +3.2$ ppm/°C) tempered from an initial temperature of 850°C assuming a glass transition temperature of 400°C.

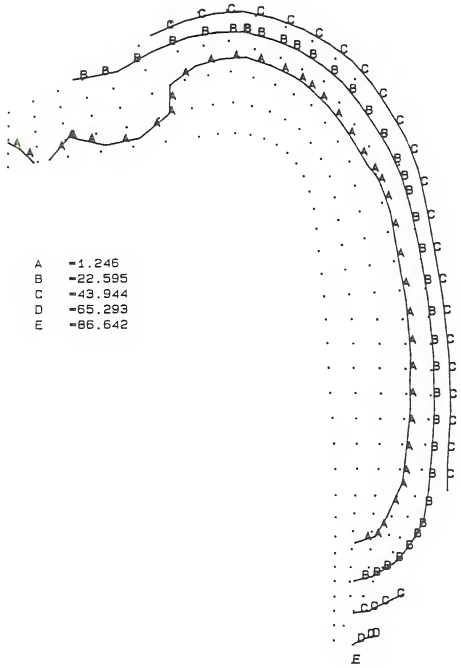

Fig. 4.117 Transient stress contours (σ_1 in MPa) for a tempered ceramic crown ($\Delta\alpha = 0$) from an initial temperature of 850°C using a glass transition temperature of 600°C.

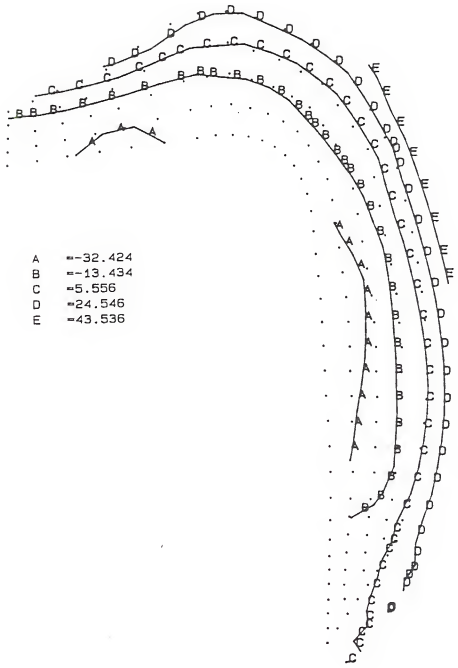

Fig. 4.118 Transient stress contours (σ_2 in MPa) for a tempered ceramic crown ($\Delta\alpha = 0$) from an initial temperature of 850°C, using a glass transition temperature of 600°C.

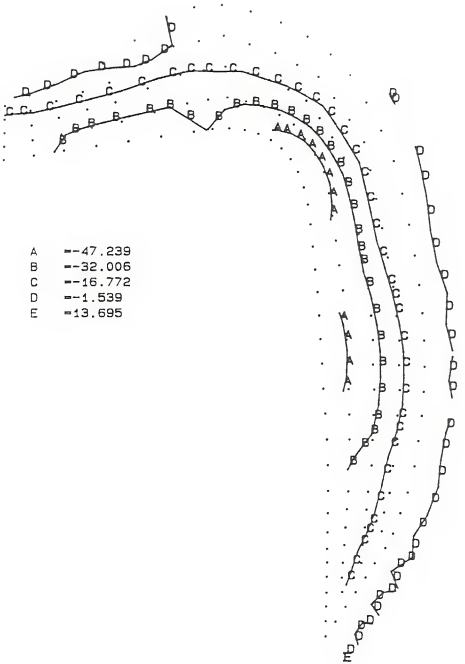

Fig. 4.119 Transient stress contours (σ_3 in MPa) for a tempered ceramic crown ($\Delta\alpha = 0$) from an initial temperature of 850°C using a glass transition temperature of 600°C.

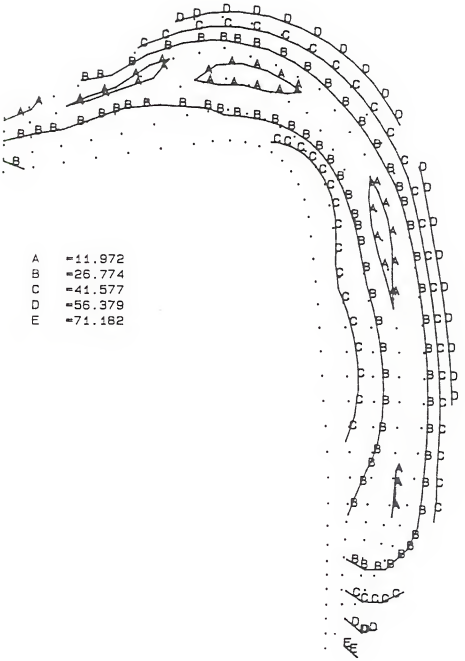

Fig. 4.120 Transient stress intensity (SI in MPa) for a tempered ceramic crown ($\Delta\alpha = 0$) from an initial temperature of 850°C using a glass transition temperature of 600°C.

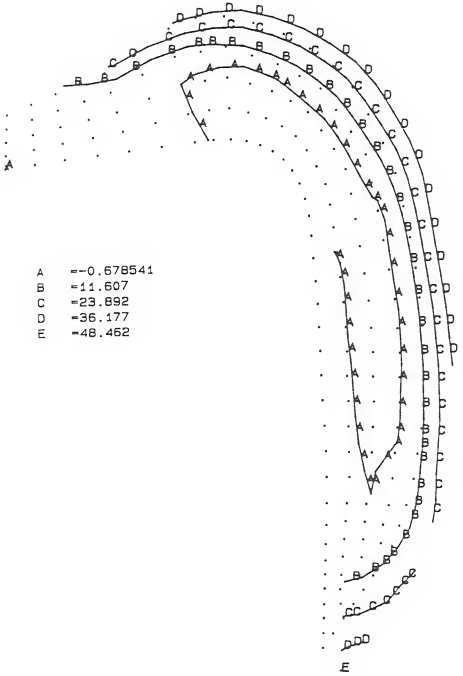

Fig. 4.121 Transient stress contours (σ_1 in MPa) for a tempered ceramic crown ($\Delta\alpha = 0$) from an initial temperature of 850°C using a glass transition temperature of 400°C.

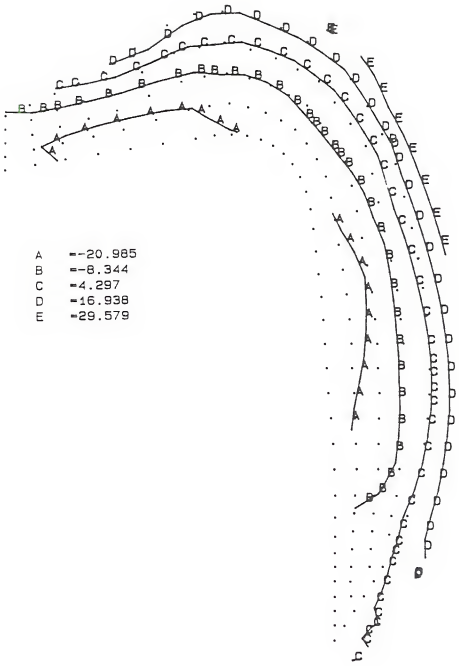

Fig. 4.122 Transient stress contours (σ_2 in MPa) for a tempered ceramic crown ($\Delta\alpha = 0$) from an initial temperature of 850°C using a glass transition temperature of 400°C.

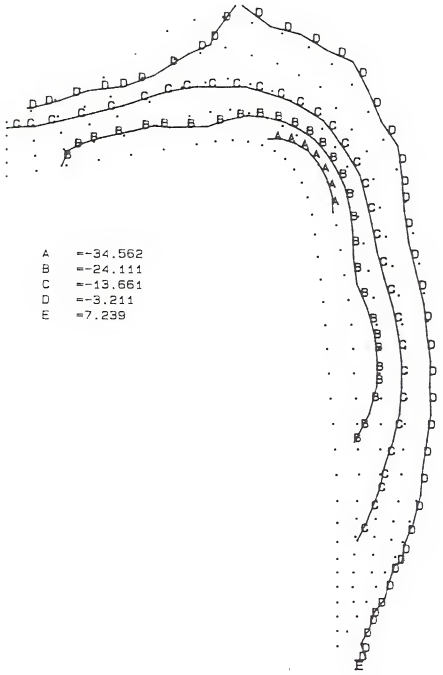

Fig. 4.123 Transient stress contours (σ_3 in MPa) for a tempered ceramic crown ($\Delta\alpha = 0$) from an initial temperature of 850°C using a glass transition temperature of 400°C.

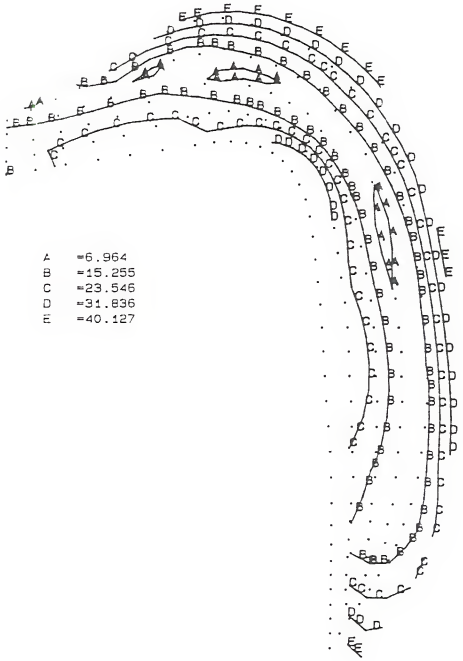

Fig. 4.124 Transient stress intensity (SI in MPa) for a tempered ceramic crown ($\Delta\alpha = 0$) from an initial temperature of 850°C using a glass transition temperature of 400°C.

Analysis of Crack Size Induced by a Microhardness Indenter

A. Statistical Analysis

Three-factor ANOVA revealed that the influence of cooling rate, thermal contraction mismatch, and initial quenching temperature and their interaction effects on induced crack size (c) was highly significant ($p = 0.001$). Throughout this paper, the dimension 'c' (Fig. 3.8), refers to one half of the measured crack length, or the 'crack size'. Shown in Table 4.1 are the results of the Tukey's multiple range test analysis for the comparison of the mean values of measured crack size in specimens quenched in silicone oil at various kinematic viscosities. As stated earlier, these oils had the same values of thermal conductivities, specific heat and density. To avoid thermal shock failure, the oil quenched experiments were performed in silicone fluids at 100°C. When the single-layered specimens ($\Delta\alpha = 0.0$ ppm/°C) with an initial temperature of 850°C were quenched in silicone oil, the differences among the crack sizes at different fluid viscosities were not significant ($p > 0.05$). There was no significant difference in crack sizes at viscosities of 50 and 5,000 centistokes for mismatch levels of 0.0 and –1.5 ppm/°C mismatch levels (Table 4.1). Shown in Table 4.2 are the mean crack sizes for disks quenched from an initial temperature of 750°C. These values for disks with mismatch levels of +3.2 ppm/°C and –1.5 ppm/°C quenched in silicone oils at viscosities of 50, 1000, and 5,000 centistokes were not significantly different.

In Table 4.3, the mean crack size for specimens quenched in silicone oil with a viscosity of 50 centistokes at each initial cooling temperature, was compared for the three contraction mismatch cases. At the initial temperature of 750°C, there were no significant difference among the induced crack sizes of the porcelain

Table 4.1 Mean crack size (μm) for bilayered disks tempered in silicone oil from an initial temperature of 850°C.

MISMATCH	SILICONE OIL VISCOSITY (CS)		
(ppm/°C)	5000	1000	50
+3.2	33.8	33.4	27.2
0.0	32.7	28.2	26.4
−1.5	42.2	34.9	38.2

NS = Not Significant

Table 4.2 Mean crack size (μm) for bilayered disks tempered in silicone oil from an initial temperature of 750°C.

MISMATCH	SILICONE OIL VISCOSITY (CS)		
(ppm/°C)	5000	1000	50
+3.2	33.2	37.8	31.8
0.0	29.3	31.5	37.3
−1.5	36.6	38.8	33.7

Table 4.3 Mean crack size (μm) for bilayered disks tempered in silicone oil at kinematic viscosity of 50 centistokes.

INITIAL TEMPERATURE	MISMATCH (ppm/°C)		
(°C)	+3.2	0.0	−1.5
850	27.2	28.2	38.2
750	31.8	37.3	33.7
650	37.4	29.2	32.5
	NS		

NS = Not Significant

Table 4.4 Mean crack size (μm) and 95% confidence intervals for bilayered disks tempered in silicone oil and in air.

MISMATCH (ppm/°C)	INITIAL TEMPERING TEMPERATURE (°C)			
	650	750	850	982
	SILICONE OIL (50 CS)			AIR
+3.2	37.4 ± 2.4	31.8 ± 2.1	27.2 ± 2.3	44.9 ± 2.7
0.0	29.2 ± 2.0	37.3 ± 2.9	28.2 ± 1.4	38.3 ± 1.4
−1.5	32.5 ± 2.0	33.7 ± 2.4	38.2 ± 4.8	38.7 ± 2.6

combinations. For the contraction mismatch level of +3.2 ppm/°C, the crack size decreased from 37.4 μm to 27.2 μm when the initial tempering temperature was increased from 650°C to 850°C. Shown in Table 4.4 are the mean crack size and 95% confidence intervals for specimens quenched in silicone oil from initial temperatures of 650, 750, and 850°C. These values are compared with the corresponding values of tempered specimens by air blasting from an initial temperature of 982°C. For the contraction mismatch levels of –1.5 ppm/°C, the mean crack size of specimens quenched in oil from 850°C were not significantly different than those of specimens which were tempered in air. It should be emphasized that the 2-mm-thick specimens quenched in silicone oil were cooled symmetrically from both sides, while under the air cooling condition, one surface was insulated. As previously stated, under the same cooling rate, the temperature distribution in a 2-mm-thick disk cooled on one side and perfectly insulated from another side is the same as that in a 4-mm-thick disk symmetrically cooled on both sides. However, quenching experiments in silicone oil were conducted using 2-mm-thick disks rather than 4-mm-thick disk to make the experiments more clinically relevant and to reduce the risk of thermal shock failure. Small values of 95% confidence intervals (Table 4.4) indicate that the surface of body porcelain in each disk is relatively homogeneous and that 20 indentations per specimen are sufficient for statistical analysis of tempering treatment.

Shown in Table 4.5 are the mean values of crack sizes for slow-cooled, fast-cooled (cooled by free convection) and tempered specimens in air from an initial temperature of 982°C. For all contraction mismatch levels, the crack sizes corresponding to tempered specimens were significantly smaller than the values of the slow-cooled (SC) and fast-cooled (FC) specimens. The mean values of crack

Table 4.5 Mean crack size (μm) for bilayered disks cooled in air from an initial temperature of 982°C.

MISMATCH (ppm/°C)	COOLING CONDITION		
	SC	FC	T
+3.2	51.6	51.8	44.9
0.0	57.5	51.0	38.3
−1.5	46.0	45.8	38.7

Table 4.6 Surface stresses in body porcelain disks cooled by free convection (FC) and tempering (T) in air, and quenched in silicone oil (OQ).

MISMATCH (ppm/°C)	SURFACE STRESS (MPa)		
	FC	T	OQ
+3.2	−4.2	−34.7	−231.9
0.0	−11.9	−84.1	−218.7
−1.5	−29.6	−81.0	−84.6

size for the SC and FC conditions were not significantly different for all three mismatch conditions.

B. Calculation of Surface Compressive Stresses

The calculated surface stresses in body porcelain for fast-cooled, tempered and oil-quenched specimens are summarized in Table 4.6. Relatively small differences in crack size for specimens cooled in air and silicone oil (Table 4.4) resulted in large differences in calculated surface stresses for the corresponding mismatch levels. For a mismatch level of +3.2 ppm/°C, the ratio of the mean crack size for the specimens tempered in air (44.9 μm) to the corresponding value of those tempered in silicone oil (27.2 μm) is 1.6, while the compressive surface stress in oil (231.9 MPa) is 6.7 times greater than the corresponding value in air (34.7 MPa). This is due to the high sensitivity of equations (9) and (11) to the input values of mean crack size. Although the surface compressive stresses in disks which were quenched in oil were greater than that specimens tempered in air, quenching in silicone oil from high temperatures were associated with a higher risk of thermal shock failure compared with air blasting.

Evaluation of the Biaxial Flexure Test Data

Tables 4.7 and 4.8 compare the biaxial flexure strength for specimens cooled in air from various initial temperatures. The increase of initial cooling temperatures (T_i) from 650 to 850°C did not have a major effect on the flexural strength of SC and FC specimens. However, for specimens tempered in air, the increase of T_i from 650 to 850°C resulted in a 25% increase in flexural strength

Table 4.7 Mean flexural strength (MPa) of body porcelain cooled in air and quenched in silicone oil (OQ) from various initial temperatures.

COOLING TREATMENT	INITIAL TEMPERATURE (°C)		
	650	750	850
SC	66.3	65.2	63.5
FC	62.8	58.0	53.2
T	80.2	100.0	107.6
OQ*	42.1	59.3	83.1

* Oil quenched specimens with 20 indentations on the surface of body porcelain.

Table 4.8 Mean flexural strength (MPa) and 95% confidence intervals of body porcelain disks cooled in air by various cooling methods.

INITIAL TEMPERATURE (°C)	COOLING CONDITION		
	SC	FC	T
982	46.4 ± 5.4	38.9 ± 5.0	116.3 ± 14.8
850	63.5 ± 4.9	53.2 ± 8.6	107.6 ± 11.5
750	65.2 ± 4.2	58.0 ± 4.6	100.0 ± 2.1
650	66.3 ± 7.0	62.8 ± 7.2	80.2 ± 6.2

(Table 4.7). There was no significant difference ($p > 0.05$) between the flexural strength of specimens tempered in air at 750 and 850°C. The flexural strength of the oil quenched specimens are also given in Table 4.7. It should be emphasized that these specimens were used for the microhardness indentation analyses prior to the flexure test. The indentations at the surface of the body porcelain may have reduced these strength values. Relatively small values of 95% confidence intervals were obtained for the flexural strength of the air cooled specimens (Table 4.8). For the comparison of the three cooling treatments and the initial temperatures, these values are plotted in Fig. 4.125. The results of Tukey's multiple range test (Table 4.8) indicate that the flexural strength of disks tempered in air were significantly greater than the corresponding values for slow-cooled and fast-cooled specimens. Shown in Table 4.9 is the comparison between the tempering stresses at the surface of body porcelain calculated from the viscoelasticity theory [66], and the biaxial flexure test data as a function of initial tempering temperature. The compressive surface stresses from the biaxial flexure test were obtained by subtracting the mean strength values of the slow-cooled specimens from the corresponding values of the tempered specimens at each temperature. These results indicate that the surface stresses predicted from the viscoelasticity and the structural relaxation analysis are much greater than those calculated from the flexure test data. For the body porcelain disks tempered from an initial temperature of 982°C, the surface compressive stress calculated from the flexure test data was 69.4 MPa, while the value obtained from the viscoelastic model was 171.4 MPa (Table 4.9). The corresponding value obtained from the microhardness indentation data (using eq. 11) was 84.1 MPa (Table 4.6). Therefore, under this condition, the data obtained from indentation measurements showed better agreement with the stress values obtained from the flexure test than the values determined from the

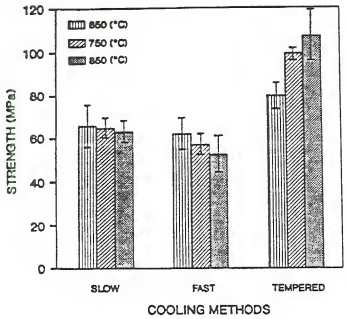

Fig. 4.125 Mean flexure strength for disk specimens cooled in air from various initial temperatures.

Table 4.9 Comparison of the tempering stresses in body porcelain calculated from viscoelastic model and biaxial flexure test.

INITIAL TEMPERING TEMPERATURE (°C)	CALCULATED STRESS (MPa)	
	Viscoelastic Model	Flexure Test
982	171.4	69.4
850	165.8	44.1
750	155.9	34.8
650	102.0	14.0

viscoelastic model. Shown in Fig. 4.126 are the mean values of biaxial flexure strength of tempered disks as a function of initial tempering temperature. The strength value increases with temperature between 650 and 982°C. However the influence of initial temperature decreases at higher values.

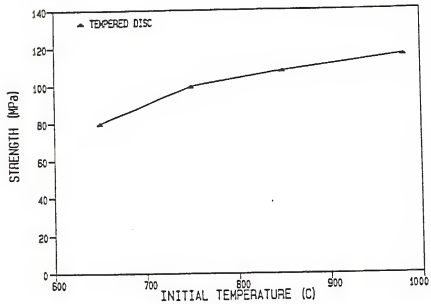

Fig. 4.126 Mean biaxial flexure strength for tempered disks as a function of initial tempering temperature.

CHAPTER V
DISCUSSIONS AND CONCLUSIONS

The strengthening effect of tempering results from the temperature gradient which is introduced over the thickness of ceramic specimens during cooling. To optimize the effectiveness of tempering in each specimen, it was necessary to obtain the temperature versus time profiles under each cooling condition. Experimental and analytical results showed that the most important variables which influenced the cooling profiles and the temperature gradient within the specimens were the initial cooling temperature, specimen thickness and the heat transfer coefficient associated with the cooling media. In general, at a constant initial tempering temperature, an increase in thickness or a higher value of heat transfer coefficient resulted in a greater temperature gradient within the specimen, thereby producing a larger magnitude of beneficial compressive stresses at the surface. However, the amount of undesirable tensile stress at the interior also increased.

Cooling Profiles

The major findings of the experimentally and analytically determined cooling profiles can be summarized as follows:

1. Tempering by a vertical flow of air resulted in a greater temperature gradient compared with tempering by a horizontal flow of air.

2. The advantage of tempering by a vertical air jet compared with a horizontal air jet was more pronounced in larger diameter specimens. Tempering by a horizontal flow may result in a nonuniform local heat transfer coefficient because of the change of boundary layer thickness. Although vertical tempering is also associated with a local heat transfer coefficient that may be nonuniform, this situation can be corrected by lateral movement of impinging jets relative to the ceramic.
3. Although helium had a greater cooling potential compared with nitrogen and air, the slopes of the temperature versus time profiles for a 2-mm-thick disk subjected to tempering by a vertical flow of either gas were similar. This similarity in cooling profiles corresponds to similar stress distributions for these cooling media. Therefore, the availability of compressed air in any dental laboratory and its low cost, support the suitability of air tempering treatment of dental porcelain compared with helium and nitrogen gases.
4. Experimental measurement of the temperature distribution within the dental furnace indicated that the specimen location inside the furnace could have a major influence on the effectiveness of cooling treatments employed for dental restorations.

In the thermal models it was assumed that each specimen was initially at a uniform temperature before cooling. However, as shown in Figs. 2.3 and 4.1, initially a temperature gradient may be associated for each specimen, depending on the size of the specimen and its location inside the furnace. Disks with a diameter of 16 mm and a thickness of 2 mm placed at the hot zone region corresponds to a more uniform initial temperature than disk with a diameter of 32 mm diameter and a thickness of 6 mm. However, in the thermal models it was assumed that each

disk was at a uniform initial temperature and had a perfect insulation layer at the bottom surface.

Each cooling treatment was associated with a convective and a radiative heat transfer coefficient. As shown in Fig. 4.9, the calculated heat transfer coefficients for free and forced convection (tempering) were approximately independent of surface temperature. However, in this study a radiative mode of heat transfer was present in each cooling condition. Based on the principle of superposition, the coefficient corresponding to radiation was added to the convective heat transfer coefficient (eq. 24). Thus, the total film coefficient (h) was influenced by the specimen surface temperature at the initial stage of cooling which becomes relatively constant at lower temperatures. For the calculation of transient tensile stresses by finite element and viscoelastic analyses, an average heat transfer coefficient over the entire temperature range was determined. This coefficient, which was independent of the thermal properties of the body, was calculated using a thin copper disk with the same diameter as the porcelain disk.

The findings based on 1-D and 2-D thermal models supported the proposed hypothesis that, under tempering conditions, the influence of heat loss from the edge of the disk model on the temperature distributions was negligible. The temperature versus time data calculated from the 1-D model for each disk were used in a viscoelastic model which was originally developed for calculation of thermal stresses within a porcelain plate symmetrically cooled from both sides [66]. In general, only small differences were obtained between the calculated and experimental data. These differences were probably due to the assumptions of perfect insulation at the bottom surface, constant initial temperatures for the specimen and cooling media, and constant values used for the thermal properties of porcelain and the heat transfer coefficients. Because of symmetry conditions, the

results of the viscoelastic model for a 2-mm-thick disk cooled from the top surface and perfectly insulated at the bottom surface are the same as the results of a 4-mm-thick disk symmetrically cooled from both sides.

Viscoelastic Analysis

Experimental techniques such as photoelasticity and analysis of strain changes after hole-drilling procedures are routinely used for residual stress measurement of glass and metal based structures. However, no direct and non-destructive experimental procedure is available to measure the transient and residual stresses in layered porcelains because of the inherent opacity of dental porcelain and the high temperature in which stresses begin to develop during cooling. The analytical methods available are based on either the viscoelastic or the elastic behavior of porcelain. In the viscoelastic models which are usually developed for simple and uniform geometric shapes, it is assumed that porcelain exhibits time-dependent viscoelastic behavior above a temperature (T_g). The elastic models are based on the assumption that a glass transition temperature (T_g) exists below which porcelain behaves like an elastic body. These models do not consider the stresses which are developed above T_g and because of that may be associated with some error. In the present study, the model developed by DeHoff and Anusavice [66] was used to determine the transient and residual stresses within porcelain because this model includes the viscoelastic effect of porcelain and accounts for stresses which are developed above T_g. Although, the viscoelastic model was originally developed for a ceramic plate which may have a different stress distribution compared with a porcelain disk because of edge effects, the results of the thermal models indicated that under tempering conditions, the edge effects were negligibly

small. Also under convective cooling, the edge effect was reduced by adjusting the heat transfer coefficient. The major findings of the viscoelastic analysis can be summarized as follows:

1. The viscoelastic model predicted relatively large transient and residual tensile stresses within 2-mm-thick and 6-mm-thick disks, respectively, cooled by tempering from high initial temperatures in liquid media and by free convection in air. These results were consistent with the experimental cooling of several disks which resulted in thermal shock failure under these cooling conditions.
2. The initial tempering temperature had a significant influence on the magnitude of stresses and on the ratio of maximum residual compressive to tensile stresses at temperatures below 750°C. However, tempering from initial temperatures above 750°C did not improve the residual stress distributions significantly.
3. In general, larger beneficial compressive stresses were associated with greater values of undesirable tensile stresses, independent of cooling rate, specimen thickness, and initial tempering temperature. At initial cooling temperatures above 850°C, the ratio of beneficial compression to undesirable tension was not strongly influenced by thermal parameters. However, it is possible that a small variation in this ratio significantly influences the strength and fracture characteristics of porcelain, and thereby controls the effectiveness of tempering.
4. The depth of compressive stress was relatively insensitive to the rate of cooling and initial tempering temperature.

It should be emphasized that the model proposed considers only a single layer viscoelastic material which behaves in a linear fashion. However, the behavior of

porcelain over the entire range of cooling temperatures considered in this study, may not be linear. Also, because of the lack of reliable thermal contraction properties of dental porcelain at high temperatures, a glass transition temperature of 400°C was assumed in the viscoelastic model.

Finite Element Analyses

To determine the influence of loading orientation, ceramic thickness, cooling rate, thermal contraction mismatch, initial tempering temperature and glass transition temperature on the stresses developed within a dental ceramic structure, these stresses were also obtained from finite element analysis which was based on elastic theory. The results of the finite element stress analyses for the bilayered ceramic disks and crowns are summarized as follows:

A. Transient Stress Analysis of Bilayered Ceramic Disks

1. Transient tensile stresses produced within the 6-mm-thick disk were higher than that of the 2-mm-thick disk and this difference increased with an increase in the heat transfer coefficient.
2. For a contraction mismatch level of +3.2 ppm/°C, oil quenching and tempering from high initial temperatures produced relatively large transient tensile stresses at the edge of the bilayered disks.
3. In general, the calculated transient tensile stresses at the edge of the disks were greater than the published tensile strength value for porcelain. This suggests that during tempering treatment, the 2-mm-thick disk is susceptible to thermal shock failure. However, the tempering experiments did not support this finding. The transient tensile stresses calculated from the finite

element method for a single layered specimens ($\Delta\alpha = 0.0$) were also greater than the corresponding values from the viscoelastic models. The large predicted stresses from the finite element analysis are probably due to the nature of the elastic analysis which does not account for stress relaxation.

B. Static Analysis of Dental Ceramic Crowns

1. Increase in ceramic thickness from 0.5 mm to 3.0 mm had a negligible influence on the stress distribution.
2. For a vertically oriented applied load of 600 N, the magnitudes of resulting tensile stresses were relatively small. However, when the load was applied along a horizontal direction, the tensile stresses which developed within ceramic rose above the failure level of ceramic. Therefore, the orientation of the applied load is an important factor in development of large tensile stresses.

C. Transient Stress Analysis of Dental Ceramic Crowns

1. Relatively large transient stresses were produced within the bilayered ceramic crowns with a thermal contraction mismatch of 3.2 ppm/°C when they were subjected to free convective cooling and tempering treatment. Under this condition, the influence of thermal contraction mismatch on the magnitude of tensile stresses was more pronounced than the influence of cooling rate.
2. Reduction of initial tempering temperature from 850°C to 750°C did not have a major influence on the transient stresses significantly.

3. The glass transition temperature had a significant influence on the magnitude of transient stresses.

Quenching In Silicone Oil

In our previous study [65], it was shown that tempering treatment significantly reduce the potential for crack growth in the surface of feldspathic porcelain. However, we indicated that development of surface tensile stresses during the initial stage of cooling may be of potential concern. The experimental results of the present study indicate that the transient tensile stresses which were produced during tempering of a 2-mm-thick disk specimen in air, were generally below the tensile strength of porcelain.

The experiments performed by Kirchner et al. [47] showed that the mean flexural strength of 96% alumina rods increased substantially when they were quenched in silicone oils with kinematic viscosities ranging from 5 to 12,500 centistokes. They reported that the highest strength was achieved by quenching the rods into low viscosity silicone oil at 30 °C (Table 1.1). In this medium, the flexural strength of two-inch-long bars determined from four-point bending test were increased by a factor of 2.5 compared with the untempered specimens, while tempering by forced-air resulted in a strengthening factor of 1.6. In the present study, the effectiveness of silicone oil as a quenching medium for dental ceramics was tested by the use of the indentation technique. Several quenching experiments were performed to determine the maximum and minimum initial quenching temperatures for feldspathic ceramic specimens (850°C) and for silicone oil (100°C), respectively, to prevent thermal shock.

In general, there was no statistically significant difference between the mean values of induced crack size for specimens quenched in silicone oil compared with

air-tempered specimens. The silicone oils used in this study had the same thermal conductivity, specific heat and density, however, they were different in viscosities. Data reported in Tables 4.1 and 4.3 indicated that the silicone oil viscosity in the range of 50 to 5,000 centistokes had no major effect on strengthening of ceramics, while in the Kirchner study [47] in which alumina specimens were quenched in silicone oil, a change in oil viscosity from 5 to 350 centistokes resulted in a decrease in flexural strength by a factor of 1.2.

The kinematic viscosity of oil (γ) has an influence on the heat transfer coefficient (h). As γ increases, h becomes smaller, however the temperature distribution and thus the stress distribution within the tempered ceramics depends also on the initial quenching temperature and specimen thickness. Perhaps, in the Kirchner study the initial specimen temperature (1600°C) and specimen thickness (3.2 mm) were large enough for the oil viscosity to change the residual stresses. However, in the present study with a initial specimen temperature of 850°C, an oil temperature of 100°C, and a specimen thickness of 2 mm, the change in heat transfer coefficient, because of the oil viscosity, was not large enough to have a major influence on residual stresses.

Microhardness Indentation Analysis

Tables 4.1 and 4.3 show only a small difference among the mean crack sizes for specimens with the three mismatch levels which were tempered in oil. Therefore, as reported in our previous studies [Anusavice et al. 65], the compatibility stresses at the surface of body porcelain are dominated by tempering stresses.

Although the mean values of crack size for disks quenched in oil were not significantly smaller than the corresponding values of specimens tempered in air

(Table 4.4), the surface compressive stresses calculated from equation (11) were much higher for specimen quenched in silicone oil. However, tempering in silicone oil from initial temperatures greater than 850°C was associated with a higher risk of thermal shock failure for the thermally incompatible specimens. Quenching of a 2-mm-thick bilayered disk ($\Delta\alpha$ = –1.5 or +3.2 ppm/°C) from 982°C in various silicone fluids at room temperature resulted in approximately 10% thermal shock failure. However, when the the initial specimen temperature was reduced to 850°C and the oil temperature was increased to 100°C, because of smaller temperature gradients, thereby smaller transient stresses during cooling, no failure occurred.

The major findings of the experimental analysis by using the microhardness indentation technique can be summarized as follows:

1. The mean crack sizes at the surface of body porcelain were significantly smaller for the tempered specimens compared with the conventionally air-cooled specimens.
2. The interaction effect of heat transfer coefficient associated with the cooling medium, initial cooling temperature and the thermal contraction mismatch on the surface crack size was statistically significant. However, the influence of thermal contraction mismatch stresses on the induced cracks were dominated by the thermal tempering stresses.
3. Silicone oil viscosity in the range of 50 to 5,000 centistokes had no major influence on the induced crack size and thus on the magnitude of surface compression.
4. Although, the measured surface crack sizes in disks which were quenched in silicone oil were smaller than the tempered specimen by air jet, quenching in

silicone oil from high initial temperatures was associated with a greater risk of thermal shock failure.

In general, under the same quenching conditions, the body porcelain disks ($\Delta\alpha = 0$) showed a better resistance to thermal shock than the bilayered disks. Quenching in silicone oil may result in a more favorable residual stress distribution because of more uniform cooling effects; however, the success of quenching in silicone oil is highly dependent on the proper selection of initial temperatures for each specimen thickness.

Biaxial Flexure Strength

The mean values of flexural strength of specimens tempered from initial temperatures of 650, 750, and 850°C were significantly greater than those for slow-cooled and fast-cooled specimens. For an initial cooling temperature of 982°C, tempering of the thermally compatible system ($\Delta\alpha = 0.0$), resulted in a mean strength value of 116.2 MPa, while the corresponding value for the specimens cooled by free convection was 39.7 MPa [65]. These results support the hypothesis that tempering improves the strength of porcelain structures. The flexural strength of the tempered disks increased with the initial cooling temperature. However, the influence of tempering temperature was much greater between 650 and 750°C (Fig. 4.51). This study showed that there was only a small and statistically insignificant difference between the mean biaxial strength values for tempered specimens for initial specimen temperatures between 982°C and 850°C. To improve the effectiveness of tempering and to minimize structural distortion because of viscous flow and air blasting, tempering should be achieved from an initial temperature of 850°C or lower. The mean flexural strength of thermally compatible tempered disks ($\Delta\alpha = 0.0$) was 1.8 times greater than the

corresponding values for the $\Delta\alpha$ = +3.2 ppm/°C group [Anusavice et al., 65]. Perhaps, the incompatibility stresses at the interior of the disk which were tensile in nature had reduced the strength of these specimens despite the tempering treatment. The major findings of the biaxial strength are summarized as follows:

1. The mean flexure strength of the tempered specimens was significantly greater than that of slow-cooled and fast-cooled specimens. Tempering treatment improved the strength of porcelain disks up to 3 times compared with conventionally cooled specimens.
2. Although the influence of the incompatibility stresses on the size of induced surface cracks was dominated by tempering, these stresses had a major influence on the flexural strength of tempered specimens. This was probably because the effect of the thermal incompatibility stresses were more pronounced at the interior than the surface region.
3. The increase of initial cooling temperature (T_i) from 650 to 850°C did not have a major effect on the flexural strength of the conventionally cooled specimens. However, for specimens tempered in air the flexural strength increased by 34%.
4. The flexural strength of the tempered disks increased with the initial cooling temperature. However, the influence of initial tempering temperature was much greater between 650 and 850°C.
5. To improve the effectiveness of tempering and to minimize structural distortion because of viscous flow and air blasting, tempering should be achieved from an initial temperature of 850°C or lower.

It should be emphasized that the condition required to justify the use of thermal tempering is that the interior tensile stresses which are produced because of applied forces do not cause any significant risk of failure. To strengthen dental

restorations or any other ceramic structure in which failure normally initiates at the surface, tempering is a promising technique.

Comparison of Predicted and Experimentally Determined Stresses

The compressive surface stresses predicted from the viscoelastic model were much greater than those calculated from the biaxial flexure test data (Table 4.9). For a 2-mm-thick disk tempered from an initial temperature of 982°C in air, the compressive stress determined from the biaxial test was 69.4 MPa, while the corresponding stress predicted from the viscoelastic model was 171.4 MPa. In explaining this difference one should consider the validity of the following points:

a) The data obtained from the biaxial flexure test were not significantly influenced by the flaws and microcracks within the body porcelain disks.

b) The tempered specimens used in flexure tests were not associated with significant warping.

c) The compressive stress calculated from the indentation test (eq. 11) showed better agreement with the values determined from flexure tests than with the viscoelastic model.

If these points are correct, one may conclude that one or more of the following factors which were not considered in the viscoelastic model were responsible for these differences:

1. The effect of the cooling rate and specimen temperature on thermal contraction coefficient, glass transition temperature, and the modulus of elasticity of porcelain were significant.
2. The relaxation function and some viscoelastic properties of glass

inappropriately assumed to be equivalent to the corresponding properties of dental porcelain.

3. The bottom surface of the porcelain disk was not perfectly insulated.
4. For the viscoelastic model, specific conditions of a two-dimensional stress state in which the horizontal and the vertical stress components were identical were assumed. The experimental tempering condition may be more accurately represented by a true two-dimensional viscoelastic model.

Recommendations for Future Studies

This study utilized various thermal stress analysis techniques to test the hypothesis that tempering by forced convective cooling in air is the most effective strengthening method for layered feldspathic porcelain structures. To simplify the theoretical and experimental analyses, porcelains were prepared in the form of bilayered disks. However, the major long-term goal is to apply the thermal tempering technique to improve the longevity of various ceramic based structures such as dental ceramic restorations.

From the foregoing study and our previous studies, it is evident that the strength of layered dental porcelains with simple geometric shapes such as disks or plates can be improved by thermal tempering treatment. The major requirement for development of compressive surface stresses by thermal tempering treatment is the viscoelastic behavior of the material at temperatures below the initial tempering temperature. Therefore, these beneficial stresses can also be developed at the surfaces of structures with more complex geometric shapes such as crowns and bridges. However, because heat transfer coefficient and ceramic thickness are important variables which determine the effectiveness of tempering, it is necessary to control the cooling rate at various locations for a complex geometric structures

with a non-uniform thickness. Perhaps a uniform cooling can be established by an adjustable array of multi-orifice nozzles which are positioned parallel to the surface of the structure.

Based on the present findings, the following recommendations are provided for the future studies:

1. Experiments should be conducted to analyze the effectiveness of thermal tempering treatment for more complex geometric shapes. To reduce the number of variables, it is recommended to start with shapes such as a semicircular hoop, with a uniform thickness.
2. Appropriate viscoelastic models should be developed to analyze thermal stresses developed in multilayered specimens. These models should also be capable of accounting for the effect of cooling rate and specimen temperature on the thermal contraction coefficient and glass transition temperature.
3. More reliable material properties such as glass transition temperature and viscosity at high temperatures are needed for porcelain.
4. For tempering of structures with curved boundaries, the effectiveness of a multi-orifice nozzle which is located in a surface parallel to the surface of structure should be investigated experimentally.

APPENDIX A

CALCULATION OF THERMAL STRESSES BY VISCOELASTICITY AND STRUCTURAL RELAXATION [66]

1- The actual temperature versus time profile in a porcelain plate cooled from an initial isothermal state is calculated from the solution for a semi-infinite plate subjected to convective cooling:

$$T(x,t) = Ta + (T_i - Ta) \sum_{n=1}^{N} \{ - \frac{2 \sin(\beta_n) \cos(\frac{\beta_n x}{a_h}) \exp(-\frac{\beta_n^2 \kappa t}{a_h^2})}{\beta_n + \sin \beta_n \cos \beta_n} \} \qquad (A-1)$$

where a_h is the plate half-thickness, x is the distance from the midplane, κ is the thermal diffusivity and t is the time. β_n are the positive roots of the transcendental equation :

$$\beta_n \tan(\beta_n) - \frac{h\, a_h}{K} = 0 \qquad (A-2)$$

where h is the convective heat transfer coefficient and K is the thermal conductivity of porcelain.

2- The fictive temperature distribution is calculated from the actual cooling profile by using numerical integration. The fictive temperature is defined as the temperature from which glass equilibrium must be quenched in order to produce a particular structural state:

$$T_f(x,t) = T(x,t) - \int_0^t \exp\{-[\frac{\xi(x,t) - \xi(x,u)}{\tau_v}]^b\} \frac{\partial T(x,u)}{\partial u} du \qquad (A-3)$$

$$\text{where } \xi(x,t) = \int_0^t \{\phi(T(x,u), T_f(x,u))\} du \qquad (A-4)$$

and $$\text{Ln}\,[\phi\,(T,T_f)] = -\frac{\Delta H^*}{2R^*}\left[\frac{1}{T}+\frac{1}{T_f}-\frac{2}{T_s}\right] \qquad \text{(A-5)}$$

ξ (x,t) is referred to as "reduced" time, based on the assumption that porcelain behaves as a thermorheologically simple viscoelastic material. This is a material in which the relaxation functions measured at two different states are related by a shift in time scale by a factor. In general, the reduced time, ξ (x,t), at a reference temperature T_r, is the time required for the material to relax the same amount as in time t at temperature T. T_s is the strain point temperature (temperature at which the viscosity is $10^{13.5}$ N cm /m^2). ΔH^* is the activation energy (kJ/mol), and R^* is the universal gas constant (8.317 J/mol. K). τ_v is the change of volume as a function of time due to step change in temperature. b is normally determined from measured relaxation data, but in this study the value of 0.68 which corresponds to glass [27] was used. ξ (x,t) also depends on the fictive temperature and viscosity of porcelain. Once the cooling profile and the viscosity as a function of temperature for porcelain are found, the fictive temperature can be determined. The integration variable u in equation (A-3) corresponds to any time between t = 0 and t for the indicated variable.

3- The transient and stress distribution is determined from the following equations:

$$\sigma(x,t) = \int_0^t R_n\,[\xi(x,t)-\xi(x,u)\,]\,\frac{\partial\,\sigma_g(x,u)}{\partial u}\,du \qquad \text{(A-6)}$$

where:

$$\sigma_g\,(x,t) = \left(\frac{E}{1-\nu}\right)\{\,\varepsilon\,(t)-\varepsilon_{th}\,(x,t)\} \qquad \text{(A-7)}$$

and

$$R_n(t) = \frac{R(t)}{R(o)} \qquad \text{(A-8)}$$

where E and ν are the Young's modulus and Poisson's ratio of porcelain at room temperature. R (t) is ,the axillary modulus R_n (t) is a normalized auxiliary function which is related to the uniaxial relaxation function of porcelain and is determined by numerical integration. ε(t) is the strain in the plate at the time t. ε_{th} (x,t) is referred to as free thermal contraction from the initial temperature state which is determined from the thermal contraction data and the actual and fictive cooling profiles.

$$\varepsilon_{th}(x,t) = a_o [\, T(x,t) - T_f(x,t) \,] + a_1 [\, T^2(x,t) - T_f^2(x,t)] + a_2 [\, T_f(x,t) - T_i \,] + a_3 [\, T_f^2(x,t) - T_i^2 \,] \qquad \text{(A-9)}$$

At the initial stage of cooling the stress and strain values within the entire specimen are zero:

$$\sigma(x,0) = 0 \quad , \quad \varepsilon(0) = 0 \qquad \text{(A-10)}$$

and the thermally induced stresses at each time must be in internal equilibrium such that :

$$\int_0^1 \sigma(x,t)\, dx = 0 \quad . \qquad \text{(A-11)}$$

This requires that :

$$\varepsilon(t_n) = \frac{\int_0^1 P(x,t_n)\,dx}{\int_0^1 [1 + R_n(x,t_{n-1})]\,dx} \qquad \text{(A-12)}$$

Using the calculated values of ε_{th} from the computer programs which had been developed in BASIC language for IBM microcomputers [66], a solution for $P(x,t_n)$ at each point in space (x) and time (t_n) is obtained by an iterative technique. Strain, $\varepsilon(t)$, at initial condition is zero and at a time t_n is calculated from (A-12) via numerical integration. Then the transient stresses within the plate are determined from the calculated strain values by using equation (A-7).

APPENDIX B

FINITE ELEMENT METHOD

In the finite element analysis, a structure is divided into discrete elements which are connected at a finite number of nodal points. The behavior of each element under internal and external forces or thermal loads applied to the structures is expressed by appropriate equations based on theory of elasticity and laws of thermodynamics. In the displacement formulation of finite element method, unknown nodal displacements are determined by solution of a system of linear equations through the application of the equilibrium conditions between internal and external forces at the nodes. The nodal forces in thermal analysis are due to temperature and in static analysis are due to applied loads. The following are basic formulations of finite element method for each problem:

I. Thermal Analysis [102]

The general equation for energy balance in the absence of any internal heat generation is :

$$\rho C_p \frac{\partial T}{\partial t} = \nabla \cdot K \nabla T \qquad \text{(B-1)}$$

For constant thermal conductivity and axisymmetric condition this equation becomes:

$$\frac{\partial T}{\partial t} = \kappa \left[\frac{\partial^2 T}{\partial r^2} + \frac{1}{r} \frac{\partial T}{\partial r} + \frac{\partial^2 T}{\partial z^2} \right] \qquad \text{(B-2)}$$

If a shape function {N} is defined such that the temperature in any arbitrary point within an element in terms of the element nodal temperature, T_e, can be obtained

from :

$$T = \{N\}^T [T_e] \quad . \tag{B-3}$$

Then the following matrix of temperature gradient can be written :

$$\{S\} = [B] \{T_e\} \tag{B-4}$$

were

$$\{S\} = \begin{pmatrix} \frac{\partial T}{\partial x} \\ \frac{\partial T}{\partial y} \\ \frac{\partial T}{\partial z} \end{pmatrix} \quad , \quad [B] = \begin{pmatrix} [\frac{\partial N}{\partial x}]^T \\ [\frac{\partial N}{\partial y}]^T \\ [\frac{\partial N}{\partial z}]^T \end{pmatrix} \tag{B-5}$$

The heat flow rates at a point can be written as :

$$\{Q\} = \begin{pmatrix} Q_x \\ Q_y \\ Q_z \end{pmatrix} = \begin{pmatrix} K_x & 0 & 0 \\ 0 & k_y & 0 \\ 0 & 0 & k_z \end{pmatrix} \begin{pmatrix} \frac{\partial T}{\partial x} \\ \frac{\partial T}{\partial y} \\ \frac{\partial T}{\partial z} \end{pmatrix} = [D] \{S\} \tag{B-6}$$

Then,

$$\{Q\} = [B]^T \{Q\} \tag{B-7}$$

The heat flow rate is related to conductivity matrix as follows :

$$[K_e] \{T_e\} = \{Q_e\} \tag{B-8}$$

So the conductivity matrix becomes :

$$\{K_e\} = \int_{vol} [B]^T [D] [B] \, d(vol) \tag{B-9}$$

Finally the matrix form of energy equation can be written in the following form :

$$[C]\ \{\frac{\partial T}{\partial t}\} + [K]\ \{T\} = \{Q_E\} \qquad \text{(B-10)}$$

where, $[C]$ = Specific hear matrix = $\rho\, C_P \int_{vol} \{N\}\ \{N\}^T\, d(vol)$ (B-11)

$[K]$ = Effective thermal conductivity matrix which can include conductive, convective and radiative surfaces.

$[Q_E]$ = Effective nodal heat flows which can include heat flow by convection surface and internal heat generation.

An implicit time integration scheme can be used to integrate the above equation with respect to time. Then a set of linear simultaneous equation is obtained which is solved by numerical techniques.

II. Static Analysis

The stress-strain relations for isotropic materials and under a plane stress condition are [103]:

$$\begin{pmatrix} \sigma_x \\ \sigma_y \\ \tau_{xy} \end{pmatrix} = [E/(1-\nu)^2] \begin{pmatrix} 1 & \nu & 0 \\ & 1 & 0 \\ \text{Symmetric} & & (1-\nu)/2 \end{pmatrix} \begin{pmatrix} \varepsilon_x - \alpha\,\Delta T \\ \varepsilon_y - \alpha\,\Delta T \\ \gamma_{xy} \end{pmatrix} \qquad \text{(B-12)}$$

General displacement expressions as a function of nodal displacements are used to describe the behavior of the element within the structure and are incorporated in the strain-displacement relations:

$$\{\varepsilon\} = \begin{pmatrix} \varepsilon_x \\ \varepsilon_y \\ \gamma_{xy} \end{pmatrix} = \begin{pmatrix} \dfrac{\partial u\,(x,y)}{\partial x} \\ \dfrac{\partial v\,(x,y)}{\partial y} \\ \dfrac{\partial u\,(x,y)}{\partial y} + \dfrac{\partial v\,(x,y)}{\partial x} \end{pmatrix} \qquad \text{(B-13)}$$

The corresponding stress-strain and strain-displacement relations for an axisymmetric problem are:

$$\begin{pmatrix} \sigma_r \\ \sigma_\theta \\ \sigma_z \\ \tau_{rz} \end{pmatrix} = [E/(1+\nu)(1-2\nu)] \begin{pmatrix} 1-\nu & \nu & \nu & 0 \\ & 1-\nu & \nu & 0 \\ & & 1-\nu & 0 \\ \text{Symmetric} & & & (1/2-\nu) \end{pmatrix} \begin{pmatrix} \varepsilon_r - \alpha\,\Delta T \\ \varepsilon_\theta - \alpha\,\Delta T \\ \varepsilon_z - \alpha\,\Delta T \\ \gamma_{rz} \end{pmatrix}$$

(B-14)

$$\{\varepsilon\} = \begin{pmatrix} \varepsilon_r \\ \varepsilon_\theta \\ \varepsilon_z \\ \gamma_{rz} \end{pmatrix} = \begin{pmatrix} \dfrac{\partial u\,(r,z)}{\partial r} \\ \dfrac{u\,(r,z)}{r} \\ \dfrac{\partial w\,(r,z)}{\partial z} \\ \dfrac{\partial w\,(r,z)}{\partial r} + \dfrac{\partial u\,(x,y)}{\partial z} \end{pmatrix} \qquad \text{(B-15)}$$

where u (x,y), v(x,y), u(r,z) and w(r,z) correspond to the displacement at any point within a finite element. For static analysis by the finite element method, a

set of simultaneous equations is solved. This has the form :

$$[K]\ \{u_N\} = \{F\} \tag{B-16}$$

or

$$\{u_N\} = [K]^{-1}\ \{F\} \tag{B-17}$$

where [K] is the total stiffness matrix and is obtained by superposition of the individual elements, $\{u_N\}$ is the vector of unknown nodal displacements and {F} is the equivalent vector of applied loads which is obtained by lumping the edge and element loads at the nodal points.

REFERENCES

1. PYE, L.D.; STEVENS, H.J.; and LACOURSE, W.C., Introduction to Glass Science, Plenum Press, New York (1972).

2. HOLLOWAY, D.G., A Look at the History of Glass Strength, In: Strength of Inorganic Glass, C.R., Kurkjian, Eds., Plenum Press, New York (1985).

3. INGLIS, C.E., Trans. Inst. Naval Arch., 55, pp. 219 (1913).

4. SNEDDON, J.N. and LOWENGRUB, M., Crack Problems in the Classical Theory of Elasticity, Wiley, New York (1969).

5. DOREMUS, R.H., Glass Science, Wiley-Interscience, New York (1973).

6. GRIFFITH, A.A., Phil. Trans. Roy. Soc., A221, pp. 163-198 (1920).

7. SAVIN, G.N., Stress Concentration around Holes, Pergamon, New York (1961).

8. MECHOLSKY, J.J., Fracture Analysis of Glass Surfaces, In: Strength of Inorganic Glass, C. R. Kurkjian, Ed., Plenum Press, New York (1985).

9. MECHOLSKY, J.J.; BECHER, P.F.; and FREIMAN, S.W., Relationship Between Surface Structure, Ceramic Processing and Mechanical Properties, Proceedings of Sagamore Army Materials Research Conf., V. 26, edg. J.J. Burke and V. Weiss, Plenum Press, New York, PP. 189-215 (1982).

10. MECHOLSKY, J.J.; FREIMAN, S.W. ; and RICE, R.W., Effect of Surface Finish On the Strength and Fracture of Glass, Proc. XIth International Congress on Glass, Prague, Czechoslovakia, pp. 489-497 (1977).

11. EVANS, A.G. and TAPPIN, G., Effect of Microstructure on Stress to Propagate Inherent Flaws, Proc. Brit. Ceram. Soc., 20, pp. 275-297 (1972).

12. GRUVER, R.M.; SOTTER, W.A.; and KIRCHNER, H.P., The Variation of Fracture Stress with Flaw Character in 96% Al_2O_3, Bull. Amer. Ceram. Soc., 55(2), pp. 198-202 (1976).

13. KELLY, A., Strong Solids, Clarendon Press, Oxford (1966).

14. BURGGRAAF, A.J., The Mechanical Strength of Alkali Silicate Glasses after Ion Exchang, Thesis, Eindoven (1965).

15. OLCOTT, J.S. and STOOKEY, S.D., In: Advances in Glass Technology, Plenum, New York, PP. 400 (1962).

16. KROHN, D. A. and COPPER, A. R., J. Am. Ceram. Soc., 52, Pg. 661 (1969).

17. RAWSON, H., Properties and Applications of Glass, Elsevier, New York, pp. 135 (1980).

18. KINGERY, W.D.; BOWEN, H.K.; and UHLM, Introduction to Ceramic, 2nd ed., pp. 830 (1987).

19. SCHAEFFER, H.A., Thermal and Chemical Strengthening of Glass Review and Outlook, In: Strength of Inorganic Glass, C. R. Kurkjian, Eds., Plenum Press, New York (1985).

20. GARDON, R., Thermal Tempering of Glass, In: Glass Science and Technology, vol. 5, Elasticity and Strength in Glasses, Edited by D. R. Uhlmann and N. J. Kreidl, Academic Press, New York, pp. 145-216 (1980).

21. GARDON, R., Calculation of Temperature Distributions in Glass Plates Under Going Heat-Treatment, J. Am. Ceram. Soc., 41 pp. 200-209 (1958).

22. GARDON, R., J. Am. Ceram. Soc., 61 pp. 143-146 (1978).

23. GARDON, R., Nonlinear Annealing of Glass, ibid., 64(2), pp. 114-119 (1981).

24. GARDON, R., Tempering Glass with Modulated Cooling Schedules, J. Am. Ceram. Soc., 71(10), pp. 876-878 (1988).

25. GARDON, R. and NARAYANASWAMY, O.S., Stress and Volume Relaxation in Annealing Flat Glass, J. Am. Ceram. Soc., 53(7), pp. 380-385 (1970).

26. NARAYANASWAMY, O.S. and GARDON, R., Calculation of Residual Stresses in Glass, J. Am. Ceram. Soc., 52 (10), pp. 554-558 (1969).

27. NARAYANASWAMY, .O.S., Stress and Structural Relaxation in Tempering Glass, J. Am. Ceram. Soc., 61(3-4), pp. 146-152 (1978).

28. NARAYANASWAMY, O.S., A Model of Structural Relaxation in Glass, J. Am. Ceram. Soc., 54, pp. 491-498 (1971).

29. MCMASTER, H.A., Practical problems in the Heat Treating of Flat Glass, Glass Ind., 31(11), pp. 569-594 (1950).

30. ACLOQUE, P., Comparison between Heat-Transfer Conditions and Setting Up of Strain in Glass During Heat-Treatment, J. Am. Ceram. Soc., 44, pp. 364-473 (1961).

31. KALMAN, P.G., The Calculation of Stresses Induced in Glass by Quenching, J. Soc. Glass Technol., 43(212) pp. 211-233 (1959).

32. KALMAN, P.G., Nonuniform Toughening of a Glass Disk, J. Am. Ceram. Soc., 43(6), pp. 313-325 (1960).

33. LEE, E.H.: ROGERS, T.G.; and WOO, T.C., Residual Stresses in a Glass Plate Cooled Symmetrically from Both Surfaces, J. Am. Ceram. Soc., 48, pp. 480-487 (1965).

34. MARSHALL, D.B. and LAWN, B.R., Strength Degradation of Thermally Tempered Glass Plates, J. Am. Ceram. Soc., 61(1-2), pp. 21-27 (1977).

35. SIEMENS, F., U.S. Patent 192,537 (1877).

36. BEAUCHAMP, E.K. and PURDY, B.A., Decrease in Fracture Toughness of Cherts by Heat Treatment, J. Mater. Sci. 21, pp. 1963-1966 (1986).

37. MECHOLSKY, J.J. and MACKIN, T.J., Fractal Analysis of Fracture in Ocala Cherts, J. Mater. Sci., pp. 1145-1147 (1988).

38. KIRCHNER, H.P., Strengthening of Ceramics, Treatments, Test, and Design Application: Marcel Dekker, Inc., New York (1979).

39. KATZ, R.N., Application of High Performance Ceramics in Heat Engine Design, Mater. Sci. and Eng., 71, pp. 227-249 (1985).

40. NICHOLLS, P.F. and PALUSZNY, A., Techniques for Design of Small Ceramic Turbine Rotors, Proc. 1st. Int. Conf. on Ceramics for High Performance Applications, Brook Hill Publishing, MA, pp. 63-78 (1974).

41. FISHER, E.A. and TRELA, W., The Evaluation of Ceramic Turbine Stators, Proc. 3rd Int. Conf. on Ceramic for High Performance Applications, Plenum, New York, pp. 623-643 (1983).

42. MASON, J. and MCLEAN, A.F., Ceramics for Gas Turbine Engines, Mater. Soc., 8(2), pp. 201-217 (1984).

43. RICHERSON, D.W., Evolution in the United States of Ceramic Technology for Turbine Engines, Am. Ceram. Soc. Bull., 64(2), pp. 282-286 (1985).

44. HUMMEL, F.A. and LOWERY, H.E., Quenching Vitrious Bodies Adds Strength, Ceram. Ind., 56(6), pp. 93-94 (1951).

45. SMOKE, E.J. and KOENING, J.H., Thermal Properties of Ceramics, Rutgers, The State Univ., Engineering Research Bull. No. 40 (1958).

46. PHILLIPS, C.J. and DIVITA, S., Thermal Conditioning of Ceramic Materials, Bull. Amer. Ceram. Soc., 43(1), pp. 6-8 (1964).

47. KIRCHNER, H.P.; WALKER, R.E.; and PLATTS, D.R., Strengthening Alumina by Quenching in Various Media, J. App. Phy., 42, pp. 3685-36692 (1971).

48. TRAVITZKY, N.A.; BRANKDON, D.G.; and GUTMANAS, E.Y., Effect of Rapid Cooling on the Microstructure and Mechanical Properties of Commercial 85 wt. % Al_2O_3, Mater. Sci. and Eng'g., 71, pp. 77-86 (1985).

49. SKINNER, E.W. and PHILLIPS, R.W., The Science of Dental Materials, Saunders, Philadelphia, (1967)

50. Clinical Instructions for DICOR™ Restorations and Use of The DICOR™ Light Activated Cementation Kit, Dentsply International, Dentsply/York Division, York, PA, pp. 1 (1988).

51. ANUSAVICE, K. J. and HOJJATIE, B., Influence of Incisal Length of Ceramic and Loading Orientation on Stress Distribution in Ceramic Crowns, J. Dent. Res., 67, pp. 1371-1375 (1988).

52. WEINSTEIN, M.; KATZ, S.; and WEINSTEIN, A.B., Fused Porcelain-to-Metal Teeth, U.S. Patent No. 3,052,982, Sept. 11, (1962).

53. WEINSTEIN, M. and WEINSTEIN, A.B., Porcelain Covered Metal-Reinforced Teeth, U.S. Patent No. 3,052,983, Sept. 11 (1962).

54. MOFFA, J. P., Clinical Evaluation of Dental Restorative Materials–Finial Report, Interagency Agreement No. 1Yo1–DE40001–05, Letterman Army Institute of Research, San Francisco (1988).

55. FARAH, J.W., and CRAIG, R.G., Distribution of Stresses in Porcelain-Fused-to-Metal and Porcelain Jacket Crowns, J. Dent Res., 54, pp. 255-261 (1975).

56. ANUSAVICE, K.J.; DEHOFF, P.H.; and FAIRHURST, C.W., Comparative Evaluation of Metal-Ceramic Bond Tests Using Finite Element Stress Analysis, J. Dent. Res., 59, pp. 608-613 (1980).

57. ANUSAVICE, K.J.; DEHOFF, P.H.; and LOCKWOOD, P.C., Thermal Shock Resistance of Porcelain Discs, J. Dent. Res., 62, pp. 1082-1085 (1983).

58. ANUSAVICE, K.J.; HOJJATIE, B.; and DEHOFF, P.H., Influence of Metal Thickness on Stress Distribution in Metal-Ceramic Crowns, J. Dent. Res., 65, pp. 1173-1178 (1986).

59. ANUSAVICE, K.J. and HOJJATIE, B., Stress Distribution Metal-Ceramic Crowns with a Facial Porcelain Margin, J. Dent. Res., 66, pp. 1493-1498 (1987).

60. DEHOFF, P.H.; ANUSAVICE, K.J.; and BOYCE, R.J., Analysis of Thermally Induced Stresses in Porcelain-Metal Systems, J. Dent. Res., 62, pp. 2593-2597 (1983).

61. DEHOFF, P.H. and ANUSAVICE, K.J., Effect of Residual Stress on Metal-Ceramic Bond Strength, J. Dent. Res., 63. pg. 233, Abst. No. 565 (1984).

62. DEHOFF, P.H. and ANUSAVICE, K.J., Effect of Viscoelastic Behavior on Stress Development in a Metal-Ceramic System, J. Dent. Res., 68, pp. 1223-1230 (1989).

63. COFFEY, J.R.; ANUSAVICE, K.J.; DEHOFF, P.H.; LEE, R.B.; and HOJJATIE, B.; Influence of Contraction Mismatch and Cooling Rate on Flexural Failure of PFM Systems, J. Dent. Res., 67, pp.61-65 (1988).

64. HOJJATIE, B.; and ANUSAVICE, K.J., Three-Dimensional Finite Element Analysis of Castable-Ceramic Dental Crown, J. Biomechanics, In press (1990).

65. ANUSAVICE, K.J.; DEHOFF, P.H.; HOJJATIE, B.; and GRAY, A., Influence of Tempering and Contraction Mismatch on Crack Development in Ceramic Surfaces, J. Dent. Res., 68, pp. 1182-1187 (1989).

66. DEHOFF, P.H. and ANUSAVICE, K.J., Tempering Stress in Feldspathic Porcelain, J. Dent. Res., 68, pp. 134-138 (1989).

67. ANUSAVICE, K.J.; HOJJATIE, B.; and GRAY, A., Inhibition of Crack Propagation in Tempered Porcelain Surfaces, J. Dent. Res. 68, Pg. 324, Abst. No. 1137 (1989).

68. HOJJATIE, B. and ANUSAVICE, K.J., Influence of Tempering Methods on Transient Incompatibility Stresses In Ceramics, J. Dent. Res. 68, Pg.324, Abst No. 1138 (1989).

69. HOJJATIE, B. and ANUSAVICE, K.J., Tempering of Bilayered Ceramics in Liquids from Various Initial Temperatures, J. Dent. Res. 68, Pg. 960, Abst No. 744, (1989).

70. SPARROW, E.M., Error Estimate in Temperature Measurement, In: Measurements in Heat Transfer, E.R.G. Eckert and R.J. Goldstein, Eds., McGraw-Hill, New York, (1976).

71. KREITH, F.,Principles of Heat Transfer, 3rd ed, Harper and Row, Publisher, New York (1973).

72. SCOTT, C.J., Transient Experimental Techniques for Surface Heat Flux Rates, In: Measurements in Heat Transfer, 2nd ed, Eckert, E.R.G. and Goldstein, R.J, Eds., McGraw-Hill, New York, (1976).

73. WELTY, J.R.; WICKS, C.E.; and WILSON, R.E., Fundamentals of Momentum, Heat, and Mass Transfer, John Wiley & Sons, New York, pg. 300 (1976).

74. EVANS, A.G. and CHARLES, E.A., Fracture Toughness Determination by Indentation, J. Am. Ceram. Soc., 59 (7-8), pp. 371-372 (1976).

75. LAWN., B.R. and FULLER, E.R., Equilibrium Penny-like Cracks in Indentation Fracture, J. Mater. Sci. (10), pp. 2016-2024 (1975).

76. LAWN, B.R.; EVANS, A.G. and MARSHALL, D.B., Elastic/Plastic Indentation Damage in Ceramics: The Median/Radial Crack System, J. Am. Ceram. Soc., (63) pp. 574-581 (1980).

77. ANSTIS, G.R.; CHANTIKUL, P.; LAWN, B.R.; and MARSHALL, D.B., A Critical Evaluation of the Indentation Technique for Measuring Fracture Toughness: I. Crack Measurement, J. Am. Ceram. Soc. (64) pp. 533-538 (1981).

78. ANUSAVICE, K.J. and LEE, R.B., Effect of Firing Temperature and Water Exposure on Crack Propagation in Unglazed Porcelain, J. Dent. Res. (60), pp. 1075-1081 (1989).

79. MARSHALL, D.B. and LAWN, B.R., An Indentation Technique for Measuring Stresses in Tempered Glass Surfaces, J. Am. Ceram. Soc. (60), pp. 86-87 (1977).

80. MARSHALL, D.B. and LAWN, B.R., Strength Degradation of Thermally Tempered Glass Plates, J. Am. Ceram. Soc. (61), pp. 21-27 (1978).

81. MARSHALL, D.B. and LAWN, B.R., Measurement of Nonuniform Distribution of Residual Stresses in Tempered Glass Discs, Glass Technology, (19), pp. 57-58 (1978).

82. MARSHALL, D.B. and LAWN, B.R., Residual Stress Effects in Sharp Contact Cracking, Part 1, Indentation Fracture Mechanics, J. Mater. Sci., (14), pp. 2001-2012 (1979).

83. WACHTMAN, J.B., Jr.; CAPPS, W.; and MANDEL, J.; Biaxial Flexure Test of Ceramic Substrates, J. Mater. JMLSA, 7(2), PP. 188-194 (1972).

84. MARSHALL, D.B., An Improved Biaxial Flexure Test for Ceramics, Ceram. Bull. 59 (5), pp. 551-552 (1980).

85. INCROPERA, F.P. and DEWITT, D.P., Fundamentals of Heat and Mass Transfer, 2nd Ed., Wiley, New York, pg. 433 (1985).

86. WRAGG, A.A., Free Convection Mass Transfer at Horizontal Electrodes, Electrochin, Acta, 13, pp. 2159-2165 (1968).

87. WRAGG, A.A. and LOOMBA, R.P., Free Convection Flow Patterns at Horizontal Surfaces with Ionic Mass Transfer, Int. J. Heat Transfer, 13, pp. 439-442 (1970).

88. SPARROW, E.M. and STRETTON, A.J., Natural Convection from Variously Oriented Cubes and from other Bodies of Unity Aspect Ratio, Int. J. Heat transfer, 28 [4],
pp. 741–752 (1985).

89. KING, W.J., The Basic Laws and Data of Heat Transmission - III. Free Convection, Mech. Eng., 54, pp. 347-353 (1932).

90. SPARROW, E.M. and ANSARI, M.A., A Refutation of King's Rule for Multi-dimensional External Natural Convection, Int. J. Heat Mass Transfer, 26(a), pp. 1357-1364 (1983).

91. KARLEKAR, B.V., and DESMOND, R.M., Heat Transfer, 2nd Ed., West, St. Paul, pp. 624-625 (1982).

92. HOLMAN, J.P., Heat Transfer, 5th Ed., McGraw Hill, New York, pg. 281 (1981).

93. KREITH, F. and BLACK, W.Z., Basic Heat Transfer, Harper and Row, New York, pg. 259 (1980).

94. THOMAS, L.C., Fundamentals of Heat Transfer, Prentice-Hall, NJ, pg. 444 (1980).

95. LEINHARD, J.H., A Heat Transfer Textbook, Prentice-Hall, NJ, pp. 261-362 (1981).

96. GOLDSTEIN, R.J.; SPARROW, E.M.; and JONES, D.C., Natural Convection Mass Transfer Adjacent to Horizontal Plates, Int. J. Heat and Mass Transfer, 16(5), pp. 1025-1034 (1973).

97. LLOYD, J.R. and MORAN, W.R., Natural Convection Adjacent to Horizontal Surfaces for Various Planforms, J. Heat. Trans., 96 pp. 443-447 (1974).

98. KAYS, W.M. and CRAWFORD, M.E., Convective Heat and Mass Transfer, 2nd ed., McGraw Hill, New York, pg. 141 (1980).

99. HOTEL, H.C. and SAROFIM, A.F., Radiative Transfer, McGraw-Hill, New York, pg. 301 (1967).

100. SPIEGEL, R., Mathematical Handbook of Formulas and Tables, McGraw-Hill, New York, pg. 143 (1968).

101. TWIGGS, S.W.; ANUSAVICE, K.J.; and FAIRHUST, C.W.; Effect of Cooling Rate on Porcelain-Alloy Compatibility, AADR Progr. & Abst. 59:No. 329 (1980).

102. ANSYS, Heat Transfer Seminar Notes, Swanson Analysis System, Inc., Rivision 4.2, Houston, Pennsylvania, (1986)

103. BURNETT, D.S., Finite Element Analysis from Concepts to Applications, Addison Wesley, Reading, Massachusetts (1987).

BIOGRAPHICAL SKETCH

Bahram Hojjatie was born in May 6, 1954, in Boroojerd, Iran. From early childhood, he was motivated by his parents who emphasized honesty, care and respect for other people, and education. In 1976, he received a Bachelor of Science degree in agricultural engineering from University of Ahwaz. To broaden his educational background and to expand his life experience, he travelled to the United States in 1977, and in 1980, he received his Master of Science degree in mechanical engineering from Mississippi State University. During his study at that university, he worked for two years on a magnetohydrodynamics research project as a graduate student assistant. From 1981 to 1983 he worked for Jacksonville Electric Authority in Jacksonville, Florida, as a power plant test engineer. In November, 1983, he began his employment as an Engineer in the Department of Dental Biomaterials at the University of Florida where he is still employed. He entered graduate school at the University of Florida in 1984, while maintaining his full-time engineering position. He is a Professional Engineer (P.E.) and author or coauthor of more than 10 research papers related to finite element analysis and other engineering applications in dental materials and biomechanics. As a part-time instructor, he has taught mathematics and statistics for four semesters at Florida Junior College and Santa Fe Community College. He presented part of his Ph.D dissertation at the International Association for Dental Research (IADR) meeting in Dublin, Ireland, in July, 1989. He was awarded a fellowship to present his paper at the Engineering Foundation Conference, in Santa Barbara, California, in August, 1989.

I certify that I have read this study and in my opinion it conforms to acceptable standards of scholarly presentation and is fully adequate, in scope and quality, as a dissertation for degree of Doctor of Philosophy.

Ulrich H. Kurzweg, Chairman
Professor of Aerospace Engineering, Mechanics, and Engineering Science

I certify that I have read this study and in my opinion it conforms to acceptable standards of scholarly presentation and is fully adequate, in scope and quality, as a dissertation for degree of Doctor of Philosophy.

Kenneth J. Anusavice, Cochairman
Professor of Materials Science and Engineering

I certify that I have read this study and in my opinion it conforms to acceptable standards of scholarly presentation and is fully adequate, in scope and quality, as a dissertation for degree of Doctor of Philosophy.

Paul H. DeHoff
Professor of Mechanical Engineering

I certify that I have read this study and in my opinion it conforms to acceptable standards of scholarly presentation and is fully adequate, in scope and quality, as a dissertation for degree of Doctor of Philosophy.

Calvin C. Oliver
Professor of Mechanical Engineering

I certify that I have read this study and in my opinion it conforms to acceptable standards of scholarly presentation and is fully adequate, in scope and quality, as a dissertation for degree of Doctor of Philosophy.

Martin A. Eisenberg
Professor of Aerospace Engineering, Mechanics, and Engineering Science

I certify that I have read this study and in my opinion it conforms to acceptable standards of scholarly presentation and is fully adequate, in scope and quality, as a dissertation for degree of Doctor of Philosophy.

Chas E Taylor

Charles E. Taylor
Professor of Aerospace Engineering,
Mechanics, and Engineering Science

This dissertation was submitted to the Graduate Faculty of the College of Engineering and to the Graduate School and was accepted as partial fulfillment of the requirements for the degree of Doctor of Philosophy.

May 1990

Winfred M. Phillips
Dean, College of Engineering

Madelyn M. Lockart
Dean, Graduate School